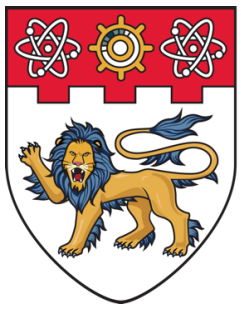

NANYANG TECHNOLOGICAL UNIVERSITY
SINGAPORE

ATOM/LIGHT INTERACTION AT THE INTERFACE OF METAMATERIALS

CHAN ENG AIK

SCHOOL OF PHYSICAL AND MATHEMATICAL SCIENCES

2018

ATOM/LIGHT INTERACTION AT THE INTERFACE OF METAMATERIALS

CHAN ENG AIK

SCHOOL OF PHYSICAL AND MATHEMATICAL SCIENCES

A thesis submitted to the Nanyang Technological University in partial fulfilment of the requirement for the degree of Doctor of Philosophy

2018

Statement of Originality

I hereby certified that the work embodied in the thesis is the result of original research done by me except otherwise stated in this thesis. The thesis work has not been submitted for a degree or professional qualification to any other university or institution. I declare that this thesis is written by myself and is free of plagiarism and of sufficient grammatical clarity to be examined. I confirm that the investigations were conducted in accord with the ethics policies and integrity standards of Nanyang Technological University and that the research data are presented honestly and without prejudice.

12 Dec 2018

Date

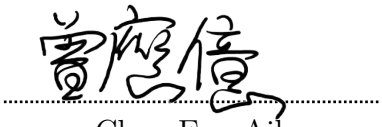

Chan Eng Aik

Supervisor Declaration Statement

I have reviewed the content and presentation style of this thesis and declare it is of sufficient grammatical clarity to be examined. To the best of my knowledge, the thesis is free of plagiarism and the research and writing are those of the candidate's except as acknowledged in the Author Attribution Statement. I confirm that the investigations were conducted in accord with the ethics policies and integrity standards of Nanyang Technological University and the research data are presented honestly and without prejudice.

14/12/2018

Date

Prof. David Wilkowski

Authorship Attribution Statement

This thesis contains material from 2 papers published in the following peer-reviewed journals where I was the first author.

Chapter 4 is published as Eng Aik Chan, Syed Abdullah Aljunid, Giorgio Adamo, Athanasios Laliotis, Martial Ducloy, and David Wilkowski. Tailoring optical metamaterials to tune the atom-surface casimir-polder interaction. Science Advances, 4(2), 2018.

The contributions of the co-authors are as follows:

- Prof. M. Ducloy, Prof. N. Zheludev and Assoc. Prof. D. Wilkowski suggested the ideas of the experiment.
- I co-designed the experimental setup with Dr. S. Aljunid and Assoc. Prof. D. Wilkowski.
- I conducted all the experimental works with Dr. S. Aljunid.
- I conducted the first stage of preparation of samples with Dr. S. Aljunid.
- Dr. G. Adamo fabricated the samples on Focused Ion Beam and I performed the samples measurements with Dr. S. Aljunid.
- I performed the data analysis with Dr. S. Aljunid, Asst. Prof. A. Laliotis, Prof. M. Ducloy and Assoc. Prof. D. Wilkowski.
- Asst. Prof. A. Laliotis, Prof. M. Ducloy and Assoc. Prof. D. Wilkowski established the theoretical models and the physical interpretations.
- Assoc. Prof. D. Wilkowski prepared the manuscript draft and I revised the manuscript together with Dr. S. Aljunid, Dr. G. Adamo, Asst.

Prof. A. Laliotis, Prof. M. Ducloy.

Chapter 6 is published as Eng Aik Chan, Syed Abdullah Aljunid, Nikolay I Zheludev, David Wilkowski, and Martial Ducloy. Doppler-free approach to optical pumping dynamics in the $6s_{1/2}$- $5d_{5/2}$ electric quadrupole transition of cesium vapor. Optics Letters, 41(9):2005–2008, 2016.

The contributions of the co-authors are as follows:

- Prof. M. Ducloy and Assoc. Prof. D. Wilkowski suggested the ideas of the experiment.
- I co-designed the experimental setup with Dr. S. Aljunid and Prof. M. Ducloy and Assoc. PRof. D. Wilkowski.
- Asst. Prof. A. Laliotis contributed to the initial setup of the experiment.
- I conducted all the experimental works with Dr. S. Aljunid.
- Dr. S. Aljunid performed the data analysis.
- Assoc. Prof. D. Wilkowski and Prof. M. Ducloy prepared the manuscript draft and I revised the manuscript with Dr. S. Aljunid.

12 Dec 2018

Date

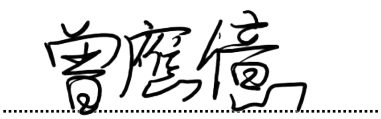

Chan Eng Aik

Abstract

An exciting frontier in the research field of atomic physics is the active engineering of the atomic environment, motivated by the prospect of applications in quantum information science, many-body physics simulation, atom-based metrology and sensor technology. To this end, one active direction in the atomic community is the manipulation of atoms at nanoscale distance from surface plasmons, utilizing the strong confinement of electric field of the surface plasmon to realize atom-trapping, single photon emitter source and strongly coupled system. Towards these goals, we experimentally investigated the coupling of hot atomic Cesium vapor with plasmonic metamaterials. First, we demonstrate tailoring of metamaterial for the tuning of atom-surface Casimir Polder interaction. Next, we realize atom-metamaterial interaction on a fiberized platform. In the atomic spectroscopy realm, we devise a method to study low-lying dipole-forbidden electric quadrupole transition with a non-linear pump-probe technique. Finally, we investigate the possible enhancement of an electric quadrupole transition in the vicinity of a plasmonic metamaterial. Overall, these advances are significant contributions towards achieving subwavelength trapping of atoms at close distance from surface, integrating of fiberized atomic systems for mainstream applications, enabling the studies of the transfer of orbital angular momentum of light to

dipole-forbidden transitions and setting forth the investigation direction for dipole-forbidden transitions in an atom-plasmonic system.

Acknowledgements

First and foremost, I would like to thank my advisor David Wilkowski for his advices during my candidature. He always set the bar high for his team and I am deeply privileged to be his student. His keen insight has played a key role in the preparation of materials in this thesis.

During the completion of this work, I have the privileged to work with Syed Aljunid. Syed Aljunid was my mentor in the lab. He has taught me many details patiently from day one, and I am impressed by his expanding wealth of knowledge in everything, from diode lasers, hot atoms spectroscopy, cold atom setup, mechanical machining, electronic circuit, theory to anything under the sun. I am also indebted to his insights when I hit a stone wall during experiments and simulations. Working with Syed proved to be tremendous learning experience, and I have nothing but praise and my gratitude to him.

I cannot thank Giorgio Adamo enough for all the guidance he has given me at many critical times in my years in CDPT. He was also our person for fabrication of metamaterials and person to go to for discussion on nanophotonics.

I am very grateful to have had the good fortune of working in the Center for Disruptive Photonic Technologies (CDPT). I would also like to thank Nikolay Zheludev who has been a wonderful example to follow as a physicist

and setting numerous discussions with us despite his busy schedule.

Martial Ducloy was also instrumental to the success of many of my works. Not only to mention his expertise in the selective reflection spectroscopy technique and atomic physics in general, he was always with us in the lab whenever he was in Singapore, offering us significant insights towards our results and he was always available to me to answer many of my questions.

I have relied heavily on the talents of Abdul Rahman of the machine workshop. Thank you or always eager to help with our challenging mechanical fabrications.

I am also grateful to Cesare Soci who has recommended me to CDPT. Without his dedication to the building of CDPT from day one, none of our works would be possible.

I have also been very fortunate to have interacted with an amazing team of colleagues in CDPT, Venkatram Nalla, Guanghui Yuan, Charles Altuzarra, Alexander Dubrovkin, Harish Krishnamoorthy, Ruixiang Guo, Jiaxing Liang, Sruthi Varier, Xinxing Sun, Mikhail Shestakov, Anton Vetlugin, Manukumara Manjappa, Hubert Basiege and many others who have come through CDPT which all I have enjoyed very much working with.

I must thank Athanasios Laliotis, for working together to get the red laser working and his efforts in the theoretical calculation of the Casimir-Polder interaction, which is essential in the theoretical interpretation in Chapter 4.

I would also like to thank Baile Zhang, Shau-Yu Lan, Dzmitry Matsukevich for reviewing my progress for the past four years.

To Chang Chi Kwong, Pramod Srinivas, Mehedi Hasan, Kanhaiya Pandey, Vincent Mancois and Frederic Leroux, thank you for being the best neighbors

possible. I cannot have imagined finishing my thesis in time without timely help in borrowing of numerous instruments from your lab.

Thank you to CDPT and Department of Physics for providing generous travel support to conferences so that I can present my work to peers and betters.

Finally, I deeply appreciate the support I have received from my family and specifically Linda , who always stuck by my side, I cannot thank her enough from the bottom of my heart for pushing me along.

Contents

Chapter 1

Introduction

Surface plasmon is known to confine light at extremely close distance of the surface by coupling of collective electron excitation with electromagnetic field. The strong confinement of light in small volumes increases the light field immensely near the surface and results in bigger interaction of light with quantum emitters like atoms [3, 4]. This is understood as the increase in the local density of states and enhancement of Pucell factor when the quantum emitters are positioned in the vicinity of plasmonic surfaces [3]. Our works fit into this juncture of localized surface plasmon in the presence of a thermal atom vapor. Several groups have successfully utilized the strong confinement of field by plasmons to enhance or alter atomic properties [5, 6, 7, 8, 9, 10, 11]. In particular, works on cold atoms have shown moderate Purcell enhancement and mainly limited due to low-quality factor of the plasmonic surface [12]. The low-quality factor of plasmon-quantum emitter coupling is due to the presence of Ohmic losses and resulted in a broadband plasmonic resonance. The broadband feature of plasmonic resonance has been taken advantaged to speed up photon emission from quantum emitters [13]. The presence of the broadband decay channels, either through coupling with surface propagating modes or to Ohmic losses can be also be taken advantage to alter the attractive Casimir - Polder interaction between the atoms and surface. Alteration of Casimir - Polder interaction was demonstrated in the studies of atoms resonant with surface polariton modes [14, 15]. These studies are still limited in wavelength and Casimir - Polder strength tunability due to limited selection from naturally occuring materials. While theoretical studies has been performed [16, 17], we successfully demonstrate experimentally that by carefully nano-structuring a metallic layer with plasmonic metamaterials,

we can achieve unprecented tunability of the Casimir - Polder strength. Our structured single layer metamaterials are subwavelength in thickness and is considered as metasurfaces in the metamaterials community. Dielectric metasurfaces, by the patterning of the subwavelength scatterers on the surface, demonstrates high flexibility in the modification of optical wavefronts and polarization, where functionalities such as ultrathin metalens, polarization rotator are realized [18, 19, 20]. Plasmonic metasurfaces, on the other hand, exhibit resonant localized surface plasmons that modify the far-field transmission and reflection spectra [21]. We are utilizing the plasmonic metasurface as sites for field enhancement and in order to differentiate that from the typical impression of metasurface for optics processes (polarization modification, ultrathin lens etc.), we call our metasurface as plasmonic metamaterials in this thesis. The tuning of Casimir - Polder interaction with plasmonic metamaterials is reported in Chapter 4 for a Cesium D2 transition at near infra-red wavelength. The same technique that we used could easily be employed to target other atomic transitions from visible region (See Chapter 7 where we target an Cesium electric quadrupole transition at visible red wavelength) to infra-red and further. Our studies have potential applications in high precision spectroscopy, that require atoms to be positioned very near to surface, where Casimir - Polder interaction is a dominant force [9, 22].

Spectroscopy of hot atomic vapor is typically done in bulky atomic vapor cells. Miniaturizing the atomic media would provide considerable opportunities for integrating atomic systems into mainstream applications. Miniaturization of atomic media have been done using hollow-core fiber [23, 24], optical waveguide [25], nanofiber [26]. We report on the first demonstration of spectroscopy of atomic vapor at an optical fiber tip and the modification of hyperfine Cesium spectrum in presence of plasmonic metamaterials in Chapter 5.

Higher-order optical forbidden atomic transitions are inherently weak - at least 6 order of magnitude or more than electric dipole transitions and thus they are not as well investigated as the electric dipole transitions. In Chapter 6, we report the first non-linear Doppler-free atomic spectroscopy on an electric quadrupole transition by optical pumping the transition and probing on a separate electric dipole transition with a mutually shared ground state. The improvement by our scheme compared to directly saturating the electric quadrupole transition is roughly given by the bare excited linewidth ratio between the electric dipole and electric quadrupole transition, which in our case it works out to be $\simeq 40$. Our Doppler-free scheme is a simple

and reliable way to resolve the hyperfine structures of higher-order atomic transitions which allows for frequency locking of laser on these weak transitions. In addition, it is possible to investigate magnetic levels optical pumping on the electric quadrupole transition using our scheme which will be discussed in Chapter 6.

Plasmonic nanostructure, with its highly localized electric fields are well suited for enhancing the higher-order atomic transitions. Associated with the highly localized electric fields are the high electric field gradients on the nanostructure surfaces, which enhance the higher-order transitions. Numerous theoretical works have been done on the enhancement effect on higher-order transition with plasmonic structures [27, 28, 29, 30] but experimental works are lacking. In Chapter 7, we report on our experimental work on pump - probe spectroscopy on an electric quadrupole transition at the vicinity of plasmonic metamaterials. We show in the chapter a modification of our spectra due to coupling of the electric quadrupole transition with the surface localized plasmons of themetamaterials. We report that the enhancement of electric quadrupole transition is dominated in the large plasmon wavevector region, in agreement with that recently reported [3], which manifests as a plasmon enhanced Doppler-broadened background in the spectroscopy spectrum.

The thesis is structured in following way. In Chapter 2, we establish the theoretical background of the general spectroscopy technique - frequency modulated selective reflection spectroscopy, which we use to probe our atomic vapor in the vicinity of an metamaterial surface. We use Cesium atoms as our atomic medium because of the presence of strong dipole transition and electric quadrupole transition in the near infra-red region and red part of the optical spectral region which eases our fabrication of metamaterials. This will be explained in Chapter 2. The general experiment setup, which we design to be adaptive to the requirements of our various atom vapor - plasmon experiments is explained in Chapter 3. In the same chapter, we also present our characterization methods on the optical properties of metamaterials. In Chapter 4, we investigate the coupling of an electric dipole transition with metamaterial. We observe Fano lineshapes like in the works reported by Stern and coauthors [7] and Stehle and coauthors for cold atoms [12]. We present the method for extracting the changes in the atom / surface Casimir-Polder interaction from the coupling of atomic vapor with the plasmonic resonances. Chapter 5 is a more technical chapter with interest potential applications where we integrate the atom - metamaterial setup on an optical fiber tip. In Chapter 6, we present a pump - probe scheme on a bulk atom vapor

setup where we optically pump on an electric quadrupole transition and simulateneously probe on an electric dipole transition with a shared ground state, which we would use as our frequency reference for the investigation of an electric quadrupole transition in vicinity of metamaterials in Chapter 7. In Chapter 7, we present our works on investigation of the enhancement of forbidden electric quadrupole transition due to the strongly localized field of plasmonic metamaterials. This is followed by the conclusion chapter - Chapter 8 where we highlight the important results and present our outlook on atomic - metamaterial system.

Chapter 2

Selective reflection spectroscopy

2.1 Introduction

In this chapter, we derive the key equations for frequency modulated selective reflection spectroscopy, the experimental technique that we use to investigate the interaction of atoms with surface plasmon of metamaterials. Selective reflection spectroscopy on an atomic vapor-surface layer produces a narrow line-shape that is selective in the atomic resonance frequency [31, 32]. The atomic resonance selective signal from the spectroscopy is a summation of coherent atomic responses from a $2\pi/\lambda$ layer above the probe surface due to the breaking of symmetry of the interface [33, 34, 35]. In this layer, there is no Doppler broadening along the surface normal and only Doppler effect along the surface has to be considered. This results in a Doppler-free spectroscopy method that is sensitive to the atom-surface interactions. In Section 2.2, we establish the expression of the reflection coefficient as a function of the atomic susceptibility and we deduce an analytical expression for the frequency modulated selective reflection spectroscopy . The Doppler free and surface sensitive behaviors of the spectroscopy technique is explained at the end of Section 2.2.5. Lastly, we illustrate the influences of van der Waals interaction and plasmonic surface on the lineshapes in Section 2.2.6).

2.2 Frequency modulated selective reflection spectroscopy

In this section, we explain the theoretical framework of our atom - metamaterial probing spectroscopy technique - frequency modulated selective reflection spectroscopy.

The reflection from an atomic vapor - window interface is modified when the frequency of the incident optical beam is tuned near a transition of the atomic vapor. This effect was first observed by Woods in 1909. He observed that a heated mercury vapor bulb displayed specular reflection when viewed at a specific angle when light from a mercury arc is shined on the bulb and he termed it as selective reflection [36]. Dispersion theory by Born and Wolf who considered dipolar displacement in atoms by the incident electric field and dissipation damping by reradiation and collisions between atoms predicts a dispersive lineshape on the selective reflection spectrum (See page 93 of [37]). This spectrum is broadened by the Doppler broadening due to the fast moving atomic vapor. In 1954, Cojan showed that light at normal incidence from a mercury cell on a glass-mercury vapor interface shows spectra narrowing features which deviates from the dispersion lineshape. He suggested the collisions of the atoms with the interface to be the source of the deviation [38]. With the advent of tunable laser sources, Woerdman and Schuurman observed clearly the sub-doppler selective reflection lineshape on the D2 line of sodium vapor in 1975 [31, 32] and Burgmans and Woerdman showed a qualitative agreement between theoretical lineshapes considering wall collisions and their experimental curves [39]. In 1982, Akulshin and coworkers frequency modulated their excitation laser at frequency smaller than the natural linewidth of the atomics line while detecting the reflected signal at the frequency of modulation. The amplitude of the atomic signals acquired on the narrow frequency sidebands recover the frequency derivative of the spectrum. This allows them to remove broad Doppler spectrum and resolve the sub-Doppler contribution as a Doppler-free dispersion lineshape. With this technique, they were able to measure the pressure broadening on Cesium D2 lines [40].

The van der Waals interaction or long range interaction between atomic dipole and induced dipole on the surface was not considered in the picture of selective reflection until first experimental evidence was obtained by Oria and coworkers in 1991 [41]. They observe a red-shift in the spectrum and

asymmetricities spectral lineshapes due to the van der Waals interaction. They calculate the van der Waals shift between the short-life excited state $6P_{3/2}$ and ground state $6S_{1/2}$ of Cesium with sapphire surface to be $4\,\mathrm{kHz}\,\mu m^3$. The theory on interpretating the van der Waals shift on frequency-modulated selective reflection spectroscopy was formulated by Ducloy and Fichet, for the regime where the atomic vapor is dilute and under linear optical excitation [42].

In the linear optical excitation regime, the arriving and departing atoms on the interface gives the same contribution to the selective reflection spectrum [33, 42]. In the non-linear regime, arriving and departing atoms contributes differently to the spectrum. The theoretical works of Vertanyan in 1985 [34] and Singh and Agarwal in 1986 [35] showed that for atoms leaving the surface, due to the relaxation of the atomic polarization after collision, the saturation intensity of the atoms leaving the surface is different from that of the atoms arriving to the surface, which are already in equilibrium with the optical field. In 1988, Neinhuis, Schuller and Ducloy generalized the theoretical works to include non-linear excitation to incidence field with arbitrary incident angle [43]. Vuletić and coauthors demonstrated experimentally the effect of optical pumping and investigated the saturation parameters of selective reflection [44]. Schuller, Gorceix and Ducloy further developed the theory for non-linear selective reflection in a cascade three-level atomic systems, in which they show that by using co-propagating pump - probe beams, they are able to selectively probe only atoms leaving the surface or otherwise in a counter-propagating configuration, the spectrum comes dominantly from atoms arriving towards the surface [45]. Neinhuis and Schuller performed the same theoretical treatment on a three-level Λ system [46]. Boiteux and coworkers performed the first pump - probe experiment on a cascade three-levels sodium system. They probed the lower level and pumped the intermediate level to the upper level. By scanning the pump laser, they observed the hyperfine levels on the upper level [47]. Hole - burning effect on a selective reflection probe with pumping a common ground state in a V type three-levels system was demonstrated by the experiment of Zhao and coauthors [48]. Guo and coauthors found that the hole-burning is extremely sensitive to velocity - changing type of collision [49]. Gross and coworkers did a comprehensive study on the conditions for incoherent and coherent effects on pump - probe selective reflection spectroscopy [50].

Previous studies focus on selective reflection with dilute atomic vapor. With dense atomic vapor, several effects become significant in influencing the

selective reflection spectrum. One of the effect is the attenuation of incident beam by the dense vapor. Electric dipole - dipole interaction also causes the atomic susceptibility to deviate from the linear polarizibility of atomic vapor [51]. In addition, collisional effects cause a broadening in the atomic spectra. Guo and co-authors showed that attenuation of field results in a blue shift on the selective reflection spectra. As a result of the transient effect of atoms leaving the surface, the amplitude of the indicent field attenuates in an oscillatory manner and causes extra blue shift. On another hand, they showed that at high atomic density, the Lorentz effect causes another red shift in the spectra [49]. Badalyan and coworkers performed theoretical and experimental studies of both dilute and dense atomic vapor in Cesium D2 line as well as rubidium D1 line. They demonstrated a general theory that agrees reasonably well with dilute and dense vapor [52].

Numerous works on selective reflection spectroscopy were also done in the presence of magnetic field of various field strength. The first few studies on magneto-optical effects done on selective reflection spectroscopy were conducted in the 1970s on the level - crossing effect using broadband light source. Zeeman sublevel from a higher hyperfine structure may cross with the Zeeman sublevel from a lower hyperfine structure. When the atoms are excited at these crossing points, we can have coherent superposition effects between the crossing Zeeman sublevels. This usually results in sub - Doppler narrowing of the atomic spectra. Stenzel and separately Siegmund and Scharmann conducted experiments on the level crossings of mercury isotopes and are able to the observe the line - crossing spectrum while scanning the magnetic field [53, 54]. The theory on level crossing effect on selective reflection was developed by Schuurmans [32]. Subsequently, Weis, Sautenkov and Hänsch performed non-linear seletive reflection with a single mode diode laser on resonance on one of the hyperfine transition of Cs D2 line. They observed the Faraday rotation of the reflected beam on applying a magnetic field in the direction of incident beam due to the ground-state coherence on the Zeeman levels [55]. Papageorgiou and coworkers investigated selective reflection spectra at intermediate magnetic field. They showed the results agree well with applying a typical dispersive lineshape on each resolved Zeeman levels [56].

Selective reflection experiments were also performed with dielectric interface coated with a thin metallic layer by Chevrollier and co-authors [57]. The absorptive component from metal attenuation mixes with the dispersive component due to dephasing of the incident laser inside the metallic film. The

authors show this effect significantly modify their selective reflection spectra, in which an unexpected nearly symmetrical spectral lineshape was reported.

When an excited atom has an de-excitation channel that is in resonant with a surface resonance mode, the coupling between the atomic decay and surface mode dephases the image dipole. This could result in switching of the van der Waals attraction to repulsion if the decay channel is to a neigbouring state [58]. The surface sensitive characteristic of selective reflection spectroscopy makes it a suitable technique to probe such a coupling. Failache and coworkers performed selective reflection spectroscopy on the cesium $6P_{1/2} - 6D_{3/2}$ and rubidium $5P_{3/2} - 6D$ which have decay channels resonant with a surface polariton mode of sapphire at 12µm . They demonstrated van der Waals repulsion potential shift on these excited states [14, 15]. Subsequently, they monitor the surface-induced decay channel of cesium $6D_{3/2} \rightarrow 7P_{1/2}$ by conducting selective reflection spectroscopy on cesium $7P_{1/2}$ to an empty high lying level on a sapphire interface. The surface - polariton enhanced decay is portrayed in the amplitude increase of the selective reflection signal [59].

Selective reflection spectroscopy is an useful technique to study atomic interaction up to the depth equal to $\lambda/2\pi$ from an interface but the technique does not discriminate the spatial variation within the probing depth. By performing the spectroscopy on an atomic vapor 'nanocell', with cell thickness varying in nanometer range, spatial selection within the probing depth could be realized. The investigation of van der Waals shift with selective reflection spectroscopy with a nanocell was done by Fichet and co-authors [60]. Spectra from region of the cell with varying thickness allowed them to quantify the spatial variation of the van der Waals shift. Selection of appropriate excited states allow them to minimize the effects of interacting surface on the spectra. Sargsyan and coworkers also demonstrated the feasiblity of using the spectroscopy method on a nanocell to monitor magnetic field in tens of nanometer resolution [61]. They determine the magnetic field applied on the nanocell by measuring the shift in the selective reflection peaks and frequency separation between the peaks.

In line with the needs of the experiments we conducted, we restrict our theoretical treatment to normal incidence beam on the interface, excitation on ground state - excited state atomic transitions of a dilute atomic vapor and under the absence of magnetic field. Figure 2.1 shows the geometry configuration of the selective reflection probe beam at normal incidence a) to the atom-dielectric interface, b) to the atom-metamaterial-dielectric interface that form the conceptual picture for our following theory. We start from

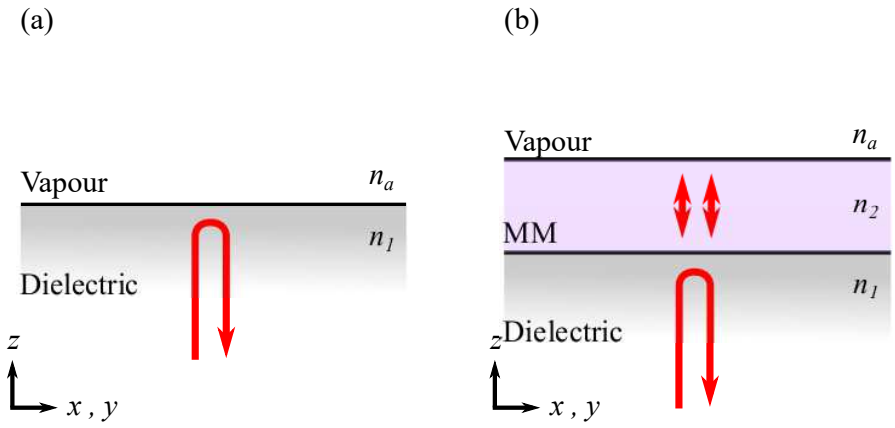

Figure 2.1: Geometry drawing of the frequency-modulated selective reflection laser beam. a) The interface layers consist of a) one interface; between dielectric window - atom b) two interfaces; between dielectric window-metamaterial, metamaterial-atomic vapor. The red arrow denotes the direction of the incident and reflected beams. The double-ended arrows denote multiple inteference in the metamaterial layer. On the bottom left, we label the convention of axes we use in this chapter.

the first principle of reflection and we will derive the expression of frequency modulated selective reflection spectra lineshape through a series of steps. At the end of the chapter, we would obtain the analytical expression of the lineshape and readers should understand the chracteristics of frequency modulated selective reflection spectroscopy; i.e., Doppler free lineshapes, the surface physical properties represented in the spectra formulae. For a general approach to the frequency modulated selective reflection spectroscopy method for excitation beam at non-normal incidence to the surface, we recommend the article by Ducloy and Fichet [42].

2.2.1 Reflection coefficient

Without loss of generality, the reflection from any atomic vapor interface is denoted by the reflection coefficient, r where the reflected electric field E_r is given by $E_r = rE_0$. The optical properties of the atomic vapor is characterized by the vapor refractive index:

$$n_a = \sqrt{1+\bar{\chi}} \approx 1 + \bar{\chi}/2 \tag{2.1}$$

where the last approximation is for for dilute vapor and $\bar{\chi}$ is the effective susceptibility of the vapor and the change in $\bar{\chi}$ is much smaller than 1. $\bar{\chi}$ is a complex number due to the presence of phase difference of the polarizibility of the vapor with the incident field and subsequently the refractive index n_a is complex. We expand r in the dilute approximation to get:

$$r = r_0 + \rho\bar{\chi} \tag{2.2}$$

where r_0 is the reflection coefficient from the interface without considering the change in susceptibilities of the atom and $\rho\bar{\chi}$ is the atomic-vapor induced reflectivity change. Using Equation (2.1),we find ρ to be,

$$\rho = \frac{1}{2}\frac{dr}{dn_a}_{n_a=1} \tag{2.3}$$

The reflectance from the interface is then given by

$$R = |r|^2 \simeq R_0 + 2Re[r_0^*\rho\bar{\chi}] \tag{2.4}$$

where the second term gives the selective reflection signal, which would be explained in details in Section 2.2.3.

2.2.2 Fresnel coefficients for multi-layer interfaces

To derive the second term $r_0^*\rho$ in Equation (2.4) for interfaces of interest in Figure 2.1, we start from the Fresnel formulae that relates the reflection and transmission coefficients at each interface to the refraction indices of respective layers. [62].

At normal incidence, the coefficients are:

$$r_{ij} = \frac{n_i - n_j}{n_i + n_j} \quad , \quad t_{ij} = \frac{2n_i}{n_i + n_j} \tag{2.5}$$

where the incident beam is propagating from the medium i to the medium j.

First, we derive the reflection coefficient for the atom-dielectric interface before discussing the same for the atom-metamaterial-dielectric interface. The reflection coefficient for atom-dielectric interface r_{1a} (Figure 2.1(a)) is straightforward:

$$r_{1a} = \frac{n_1 - n_a}{n_1 + n_a} \tag{2.6}$$

For the atom-metamaterial-dielectric interface (Figure 2.1(b)), one has to account for the multiple internal reflections in the metamaterials of thickness l. Such a derivation is analogous to the derivation for Fabry-Pérot transmission and reflection. The reflection coefficient for the atom-metamaterial-dielectric interface r is given by:

$$\begin{aligned} r &= r_{12} + t_{12}t_{21}\sum_{n=1}^{\infty} r_{2a}^{n} r_{21}^{n-1} \mathrm{e}^{2i\phi} \\ &= r_{12} + \frac{r_{2a}t_{12}t_{21}e^{2i\phi}}{1 - r_{2a}r_{21}\mathrm{e}^{2i\phi}} \end{aligned}$$

where the second term comes from the multiple internal reflection in the metamaterial. $\mathrm{e}^{2i\phi}$ is the propagation phase picked up in the metamaterial after a roundtrip where $\phi = n_2 l\omega/c$. c is the speed of light in freespace.

After some manipulation, and utilizing the property that $r_{ij}r_{ji} - t_{ij}t_{ji} = -1$, we find:

$$r = \frac{r_{12} + r_{2a}e^{2i\phi}}{1 - r_{2a}r_{21}\mathrm{e}^{2i\phi}} \tag{2.7}$$

$$= \frac{(n_1 - n_2)(n_2 + n_a) + (n_1 + n_2)(n_2 - n_a)\mathrm{e}^{2i\phi}}{(n_1 + n_2)(n_2 + n_a) - (n_2 - n_1)(n_2 - n_a)\mathrm{e}^{2i\phi}}. \tag{2.8}$$

where the last step is perfomed by subsituting Equation (2.5) into Equation (2.7). n_1, n_2, n_a are the refractive indices of the dielectric, metamaterial, atomic vapor layers respectively.

2.2.3 Selective contribution to the reflection

The second term, $r_0^*\rho$ of Equation (2.4) is not trivial as the terms contain the response of the atom-interface in reflection spectroscopy. In this section, we will use the reflection coefficients derived in the previous section to derive an analytical expression of the term $r_0^*\rho$. The effective atomic susceptibility $\bar{\chi}$ in Equation (2.4) will be derived in Section 2.2.5.

Differentiating Equation (2.6) in the Equation (2.3), we get the ρ expression for atom-dielectric interface. Similarly we would get the same for atom-MM-dielectric interface by differenting Equation (2.8) in Equation (2.3).

From Equation (2.3),

$$\begin{aligned} r_0^*\rho &= \frac{r_0^*}{2}\frac{dr}{dn_a}_{n_a=1} \\ &= \frac{|r_0|^2}{2}\frac{1}{r_0}\frac{dr}{dn_a}_{n_a=1} \\ &= \frac{|r_0|^2}{2}\frac{d\,ln\,r}{dn_a}_{n_a=1} \end{aligned} \tag{2.9}$$

For atom-dielectric interface, Equation (2.9) gives:

$$r_0^*\rho = \frac{|r_0|^2 n_1}{1-n_1^2} \tag{2.10}$$

For atom-MM-dielectric interface, it is:

$$r_0^*\rho = \frac{4|r_0|^2 n_1 n_2^2 \mathrm{e}^{2i\phi}}{(1+n_2)^2(n_2^2-n_1^2)+2(n_1^2+n_2^2)(1-n_2^2)\mathrm{e}^{2i\phi}+(1-n_2)^2(n_2^2-n_1^2)\mathrm{e}^{4i\phi}} \tag{2.11}$$

2.2.4 Reflection signal of frequency modulated spectroscopy

In this section, we include the frequency modulation terms into the reflection coefficient expressed in Section 2.2.1. This would be followed by taking the simplest case where the beam is weakly modulated and we would see that the demodulated signal contains the dispersive and absorptive features of the atomic susceptibility.

Frequency modulating the incident beam introduces frequency sidebands to the incident electric field according to:

$$E_0(t) = E_0\mathrm{e}^{-\mathrm{i}\omega_0 t}\sum_{N=-\infty}^{\infty} J_N(M)\mathrm{e}^{-\mathrm{i}N\omega_m t} \tag{2.12}$$

J_N represents the Bessel function of the first kind, where N is the sideband order, M is the modulation index and ω_m is the modulation frequency.

The reflected field is given by:

$$E_r = E_0\mathrm{e}^{-\mathrm{i}\omega_0 t}\sum_{N=-\infty}^{\infty} r(\omega_0+N\omega_m)J_N(M)\mathrm{e}^{-\mathrm{i}N\omega_m t} \tag{2.13}$$

The reflected intensity is:

$$I_r = |E_r|^2 = E_0^2 \sum_{N,N'=-\infty,-\infty}^{\infty} r(\omega_0 + N\omega_m) r^*(\omega_0 + N'\omega_m) J_N J_{N'} \mathrm{e}^{-\mathrm{i}(N-N')\omega_m t} \tag{2.14}$$

where $r = r_0 + \rho\bar{\chi}(\omega_0 + N\omega_m)$.

The reflectance $R = |E_r^2/E_0^2|$ reads:

$$\begin{aligned} R &= \sum_{N,N'=-\infty}^{\infty} r(\omega_0 + N\omega_m) r^*(\omega_0 + N'\omega_m) J_N J_{N'} \mathrm{e}^{-\mathrm{i}(N-N')\omega_m t} \\ &= r_0^2 + r_0^* \rho \sum_{N,N'=-\infty,-\infty}^{\infty} \Big[\bar{\chi}(\omega_0 + N\omega_m) + \bar{\chi}^*(\omega + N'\omega_m) \Big] J_N J_{N'} \mathrm{e}^{-\mathrm{i}(N-N')\omega_m t} + c.c. \end{aligned} \tag{2.15}$$

The second term gives us the response of the atomic vapor to the frequency modulated beam. Note that $\bar{\chi}$ is a complex variable and the real part yields the dispersive response of the atomic vapor and the imaginary part yields the absorptive response of the atomic vapor.

At weak modulation index (when M is small), only the Bessels function of the zeroth and first order J_0 and $J_{\pm 1}$ dominate, and the response of the atomic vapor to the frequency modulated beam, which we denote as δR is left with:

$$\begin{aligned} \delta R = r_0^2 + r_0^* \rho \Bigg\{ & \Big[\bar{\chi}(\omega_0 + \omega_m) + \bar{\chi}^*(\omega_0) \Big] J_1 J_0 \mathrm{e}^{-\mathrm{i}\omega_m t} \\ & + \Big[\bar{\chi}(\omega_0) + \bar{\chi}^*(\omega_0 - \omega_m) \Big] J_0 J_{-1} \mathrm{e}^{-\mathrm{i}\omega_m t} \\ & + \Big[\bar{\chi}(\omega_0) + \bar{\chi}^*(\omega_0) \Big] J_0 J_0 \\ & + \Big[\bar{\chi}(\omega_0 + \omega_m) + \bar{\chi}^*(\omega_0 + \omega_m) \Big] J_1 J_1 \\ & + \Big[\bar{\chi}(\omega_0 - \omega_m) + \bar{\chi}^*(\omega_0) \Big] J_{-1} J_0 \mathrm{e}^{\mathrm{i}\omega_m t} \\ & + \Big[\bar{\chi}(\omega_0) + \bar{\chi}^*(\omega_0 + \omega_m) \Big] J_0 J_1 \mathrm{e}^{\mathrm{i}\omega_m t} \Bigg\} \end{aligned} \tag{2.16}$$

The demodulated signal at ω_m will select the terms evolving with $\mathrm{e}^{-\mathrm{i}\omega_m t}$. The δR at modulation frequency ω_m is left with:

$$\delta R(\omega=\omega_m) = r_0^* \rho J_0 J_1 \Big[\bar{\chi}(\omega_0+\omega_m) + \bar{\chi}^*(\omega_0) - \bar{\chi}(\omega_0) - \chi^*(\omega_0-\omega_m)\Big]\mathrm{e}^{-\mathrm{i}\omega_m t} \tag{2.17}$$

In experiment the demodulated reflection signal is detected by an optical detector and the signal is converted to an electric voltage. Thus, the voltage of the demodulated signal consists of the in-phase $V_p(\omega)$ and in-quadrature $V_q(\omega)$ terms where the in-phase component is the real part of the demodulated signal whereas the in-quadrature component is the imaginary part of the demodulated signal:

$$V_p(\omega) = V_0 \mathrm{Re}\{r_0^* \rho[\bar{\chi}(\omega+\omega_m) - \bar{\chi}(\omega-\omega_m)]\} \tag{2.18}$$

$$V_q(\omega) = V_0 \mathrm{Im}\{r_0^* \rho[\bar{\chi}(\omega+\omega_m) + \bar{\chi}(\omega-\omega_m) - 2\bar{\chi}(\omega)]\} \tag{2.19}$$

where the voltage amplitude V_0 depends on the reflectance amplitude and the overall sensitivity of the detection scheme. The in-phase component $V_p(\omega)$ consists a pair of dispersive duplets and the in-quadrature component $V_q(\omega)$ consists a summation of three triplets. When the modulation frequency is smaller than the atomic linewidth $\omega_m \ll \gamma$, we get the derivatives of the selective reflection signal [63]. This allows us to remove the broad slow varying Doppler background and amplify our Doppler-free response.

2.2.5 Atomic vapor - light coupling in terms of the susceptibility

In this section, we give the expression of the effective susceptibility $\bar{\chi}$ used in Equations (2.18) and (2.19). We derive the effective susceptibility performing integration over the velocity and spatial distribution of the atoms above the interface. We take the interface plane as xy plane and the incident propagation axis as the z axis, as labeled in Figure 2.1. We assume translational invariance in the xy plane, even for the case of metamaterial, as the variation of the localized plasmon is well smoothed by the finite response time of the atomic coherence.

The effective susceptibility can be written as:

$$\bar{\chi} = N \int_{-\infty}^{\infty} \mathrm{d}^3\boldsymbol{v} W(\boldsymbol{v}) \chi(\boldsymbol{v}) \tag{2.20}$$

in which N is the atomic density, $W(\boldsymbol{v})$ is the normalized atom velocity distribution. $\chi(\boldsymbol{v})$, the specific susceptibility is defined as:

$$\chi(\boldsymbol{v}) = -\frac{2ik\mu}{\epsilon_0 E_0}\int_0^\infty \mathrm{d}z\sigma_{eg}(z,\boldsymbol{v})\mathrm{e}^{2ikz} \tag{2.21}$$

where μ is the electric dipole moment, $k = 2\pi/\lambda$ is the wavenumber, ϵ_0 is the electrical permittivity in vacuum, E_0 is the electric field amplitude, $\sigma_{eg}(z,\boldsymbol{v})$ is the off diagonal density matrix element of an atom at distance z and with velocity $\boldsymbol{v}$ where the value depends on the past evolution of the atom and e^{2ikz} is the round trip propagation phase factor.

The time evolution of the off diagonal density matrix element is governed by the optical Bloch equations:

$$\frac{\mathrm{d}}{\mathrm{d}t}\sigma_{eg} = -[\frac{\gamma_{eg}}{2} - \mathrm{i}\delta + ikv_z]\sigma_{eg} + \frac{\mathrm{i}\Omega}{2}(\sigma_{gg} - \sigma_{ee}) \tag{2.22}$$

where γ_{eg} is the natural decay rate, $\Omega = 2\mu E_0/\hbar$ is the Rabi frequency, $(\sigma_{gg} - \sigma_{ee})$ is the difference in population between the ground state and the excited state, kv_z is the Doppler shift term.

Due to atom-surface interaction, we have a frequency shift that depends on z where $\delta = \omega - \omega_0 + \Delta C_3/z^3$ in the non-retarded potential [64, 65], where ΔC_3 denotes the strength of the differences in van der Waals shift between the excited and ground states. We treat the ΔC_3 to be a complex number, which accounts for the decay losses of the coupling of atoms to the plasmonic surface.

Making the assumption that the optical coupling is in linear regime and far from saturation ($\Omega < \gamma_{eg}$) such that $\sigma_{gg} \approx 1$ and $\sigma_{ee} \approx 0$. Equation (2.22) becomes:

$$\frac{\mathrm{d}}{\mathrm{d}t}\sigma_{eg} = -[\frac{\gamma_{eg}}{2} - \mathrm{i}(\omega - \omega_0 + \frac{\Delta C_3}{z^3}) + ikv_z]\sigma_{eg} + \frac{\mathrm{i}\Omega}{2} \tag{2.23}$$

The time derivative in Equation (2.23) is a convective derivative $d/dt = \partial/\partial t + \boldsymbol{v}\cdot\nabla$. In the steady state regime, σ_{eg} is only dependent on z and we get:

$$\frac{1}{v_z}\frac{\mathrm{d}}{\mathrm{d}z}\sigma_{eg} = -[\frac{\gamma_{eg}}{2} - \mathrm{i}(\omega - \omega_0 + \frac{\Delta C_3}{z^3}) + ikv_z]\sigma_{eg} + \frac{\mathrm{i}\Omega}{2} \tag{2.24}$$

Equation (2.24) is solved by introducing a new variable $\mathcal{L}(z)$ as the integration of:

$$\frac{\mathrm{d}}{\mathrm{d}z}\mathcal{L}(z,v_z) = \frac{\gamma_{eg}}{2} - \mathrm{i}(\omega - \omega_0 + \frac{\Delta C_3}{z^3} - \mathrm{i}kv_z) \tag{2.25}$$

Solving for $\mathcal{L}$,

$$\mathcal{L}(z, v_z) = \frac{\gamma_{eg} z}{2} - \mathrm{i}[(\omega - \omega_0)z - \frac{\Delta C_3}{2z^2} - izkv_z] \tag{2.26}$$

We can express the solution for σ_{eg} for an atom transversing starting from the vertical position z_0 to the position z in terms of $\mathcal{L}(z)$ by integrating Equation (2.24) with respect to z. We get,

$$\sigma_{eg}(z, v_z) = \mathrm{i}\frac{\Omega}{2v_z}\int_{z_0}^{z} \mathrm{e}^{[\mathcal{L}(z', v_z) - \mathcal{L}(z, v_z)]/v_z} \mathrm{d}z \tag{2.27}$$

Now, we can express the effective susceptibility, from Equation (2.21)) as:

$$\chi(v_z) = \frac{2k\mu^2}{\epsilon_0 \hbar}\frac{1}{v_z}\int_0^{\infty}\int_{z_0}^{z} \mathrm{e}^{[\mathcal{L}(z', v_z) - \mathcal{L}(z, v_z)]/v_z} \mathrm{e}^{2ikz} \mathrm{d}z' \mathrm{d}z \tag{2.28}$$

Atoms that are moving towards the surface (Case 1 : $v_z < 0$) are integrated from $z_0 = \infty$ and atoms that are moving away from the surface (Case 2 : $v_z > 0$) are integrated from $z_0 = 0$ where at $z_0 = 0$ the coherence of the atoms are disrupted when they collide with the surface. For case 1, we have:

$$\chi(v_z < 0) = \frac{2k\mu^2}{\epsilon_0 \hbar}\frac{1}{v_z}\int_0^{\infty}\int_{\infty}^{z} \mathrm{e}^{[\mathcal{L}(z') - \mathcal{L}(z)]/v_z} \mathrm{e}^{2ikz} \mathrm{d}z' \mathrm{d}z \tag{2.29}$$

For case 2, we have:

$$\chi(v_z < 0) = \frac{2k\mu^2}{\epsilon_0 \hbar}\frac{1}{v_z}\int_0^{\infty}\int_{0}^{z} \mathrm{e}^{[\mathcal{L}(z') - \mathcal{L}(z)]/v_z} \mathrm{e}^{2ikz} \mathrm{d}z' \mathrm{d}z \tag{2.30}$$

We show that $\chi(v_z < 0) = \chi(v_z > 0)$ by using the identity:

$$\int_0^{\infty} \mathrm{d}z \int_{\infty}^{z} \mathrm{d}z' = -\int_0^{\infty} \mathrm{d}z' \int_0^{z'} \mathrm{d}z \tag{2.31}$$

to replace the double integrals in Equation (2.29) with Equation (2.31), we get:

$$\begin{aligned}\chi(v_z < 0) &= \frac{2k\mu^2}{\epsilon_0 \hbar}\frac{1}{-|v_z|}\int_0^{\infty}\int_{0}^{z'} \mathrm{e}^{[\mathcal{L}(z', -|v_z|) - \mathcal{L}(z, -|v_z|)]/-|v_z|} \mathrm{e}^{2ikz} \mathrm{d}z \mathrm{d}z' \\ &= \chi(v_z > 0)\end{aligned} \tag{2.32}$$

The above equation shows that the unit susceptibility of the atoms does not depend on the z direction of which the atoms is travelling. For atoms with $v_z = 0$, the specific susceptibility (Equation (2.28)) can be simplified to:

$$\chi(v_z = 0) = \frac{2k\mu^2}{\epsilon_0 \hbar} \int_0^\infty \frac{\mathrm{e}^{2ikz}}{\frac{\gamma_{eg}}{2} - \mathrm{i}(\omega - \omega_0 + \frac{\Delta C_3}{z^3} - kv_z)} \mathrm{d}z \tag{2.33}$$

Following that, the effective susceptibility in Equation (2.20) can now be expressed in terms of $+v_z$ and $-v_z$ distributions since we already assume traslational invariance in the xy plane,

$$\bar{\chi} = \frac{2Nk\mu^2}{\epsilon_0 \hbar} \int_0^\infty \mathrm{d}v_z \frac{W(v_z) + W(-v_z)}{v_z} \int_0^\infty \int_0^z dz dz' \mathrm{e}^{[\mathcal{L}_0(z') - \mathcal{L}_0(z)]/v_z} \mathrm{e}^{\mathrm{i}k(z+z')} \tag{2.34}$$

by substituting Equations (2.29) and (2.32) into Equation (2.20) and velocity symmetricity of $\chi(v_z)$ allows us to truncate the integral of v_z from $v_z = 0$ to $v_z = \infty$. Since we assume the spatial variation of atoms polarization along xy can be neglected, we are left with integral over v_z.

We define another variable $\mathcal{L}_0(z)$ as:

$$\mathcal{L}_0(z) = \mathcal{L}(z, v = 0) = \frac{\gamma_{eg} z}{2} - \mathrm{i}[(\omega - \omega_0)z + \frac{\Delta C_3}{2z^2}] \tag{2.35}$$

so that we withdraw the Doppler shift kzv_z term from Equation (2.26) and combine with the phase propagation term e^{2ikz} in Equation (2.34)).

The Doppler width $k\bar{u}$ is much larger than γ, where $\bar{u}$ is the mean of the velocity distribution. In this Doppler limit, the velocity distributions $W(v_z)$ and $W(-v_z)$ are approximately constant at the velocity interval $v_z = \pm\gamma_{eg}/k$). This approximation gives us:

$$\bar{\chi} = \frac{2Nk\mu^2}{\epsilon_0 \hbar} W(0_+) + W(0_-) \int_0^\infty \int_0^z \mathrm{e}^{\mathrm{i}k(z+z')} dz dz' \int_0^\infty \frac{1}{v_z} \mathrm{e}^{[\mathcal{L}_0(z') - \mathcal{L}_0(z)]/v_z} \mathrm{d}v_z \tag{2.36}$$

The integration of $\mathrm{d}v_z$ over $\mathrm{e}^{[\mathcal{L}_0(z') - \mathcal{L}_0(z)]/v_z}/v_z$ would yield exponential integral $-\mathrm{Ei}([\mathcal{L}_0(z') - \mathcal{L}_0(z)]/v_z)|_0^\infty$ which has discontinuity poles at both $v_z = 0$ and ∞, which would cause the integral to be undefined. To circumvent the problem, we analyze our selective reflection signal by computing the derivative of $\bar{\chi}$ with respect to ω and integrate over ω to get $\bar{\chi}$, such that:

$$\frac{\mathrm{d}\bar{\chi}}{\mathrm{d}\omega} = \frac{2Nk\mu^2}{\epsilon_0 \hbar} W(0_+) + W(0_-) \int_0^\infty \int_0^z dz dz' \mathrm{i}(z - z') \mathrm{e}^{\mathrm{i}k(z+z')} \int_0^\infty \frac{1}{v_z^2} \mathrm{e}^{[\mathcal{L}_0(z') - \mathcal{L}_0(z)]/v_z} \mathrm{d}v_z \tag{2.37}$$

where the derivative with respect to ω only acts on $\mathrm{e}^{[\mathcal{L}_0(z')-\mathcal{L}_0(z)]/v_z}$, which garners us an extra $\mathrm{i}(z-z')/v_z$ term.

Integrating with respect to v_z:

$$\frac{\mathrm{d}\bar{\chi}}{\mathrm{d}\omega} = \frac{\mathrm{i}Nk\mu^2}{\epsilon_0\hbar}W(0_+) + W(0_-)\int_0^\infty\int_0^z dzdz'\mathrm{e}^{\mathrm{i}k(z+z')}\frac{z-z'}{\mathcal{L}_0(z)-\mathcal{L}_0(z')} \tag{2.38}$$

Taking the Boltzmann velocity distribution where $W(v_z) = 1/(\sqrt{\pi}\bar{u})\mathrm{e}^{v_z^2/\bar{u}^2}$, we get:

$$\frac{\mathrm{d}\bar{\chi}}{\mathrm{d}\omega} = \frac{i2Nk\mu^2}{\sqrt{\pi}\bar{u}\epsilon_0\hbar}\int_0^\infty\int_0^z dzdz'\mathrm{e}^{ik(z+z')}\frac{z-z'}{\mathcal{L}_0(z)-\mathcal{L}_0(z')} \tag{2.39}$$

Using Equation (2.39), integrated over ω to get $\bar{\chi}$ and Equations (2.18) and (2.19) which define the constituents of $\bar{\chi}$ in the demodulated signal, we can use it to fit the demodulated signal to obtain ΔC_3.

A brief discussion on the characteristics of the FM-SR spectroscopy is warranted after laying down the analytic expression of the spectrum. In the last term of Equation (2.37), $1/(v_z^2)\mathrm{e}^{[\mathcal{L}_0(z')-\mathcal{L}_0(z)]/v_z}$ denotes the function of contribution of atoms with velocity v_z to the spectrum. $\mathrm{e}^{[\mathcal{L}_0(z')-\mathcal{L}_0(z)]/v_z}$ is a complex term and $1/v_z^2$ is big when $v_z \approx 0$. This demonstrates that the dominant contribution are from atoms with velocity v_z close to zero and moving parallel to the surface with $v_z \simeq 0$. In addition to that, due to the wavevector selection of the field (See Equation (2.22)), $\bar{\chi}$ does not experience Doppler broadening for velocities parallel to the surface. This explains for the Doppler free spectrum we get on the FM-SR spectroscopy.

The surface sensitive feature of the susceptibilities can be seen from the integrand over $\mathrm{d}z$ of Equation (2.39), which in the denominator is the difference between $\mathcal{L}_0$ at location z versus z'. From the definition of Equation (2.35), we can rewrite the integrand as

$$\frac{z-z'}{\mathcal{L}_0(z)-\mathcal{L}_0(z')} = \frac{z-z'}{zL_0(z)-z'L_0(z')} \tag{2.40}$$

where $L_0(z) = \gamma_{eg}/2 - \mathrm{i}[(\omega-\omega_0) + \Delta C_3/(2z^3)]$. At z distance far away from surface; i.e. $\Delta C_3/z^3 \ll \gamma_{eg}$, $L_0(z) = L_0(z') = \gamma_{eg}/2 - \mathrm{i}(\omega-\omega_0)$ and Equation (2.40) reduces to $1/L_0$. We see that the integrand are independent of z and z' and the double-space integral over z and z' only harvests constants for z and z' away from the surface. The only terms that give non-trivial contributions to the integral are non-local relations in Equation (2.40) between

i) surface atoms - surface atoms, and ii) surface atoms - free space atoms in the double-space integral. Next we can estimate a characteristic surface sensitive length scale d_z by calculating how much is the mean distance travel by the atoms that contributes to the Doppler free linewidth of γ_{eg} in a coherence time t_{coh}. In approximation, $d_z \approx v_z^{(Df)} t_{coh} = v_z^{(Df)} 1/\gamma_{eg}$ where $v_z^{(Df)} = \gamma_{eg}/k$ is the characteristic Doppler free (Df) velocity in $\mathrm{d}\bar{\chi}/\mathrm{d}\omega$ and $t_{coh} = 1/\gamma_{eg}$ denotes the characteristic coherence time of the atom. This gives us $d_z = k^{-1} = \lambda/(2\pi)$, which is the characteristic length scale of the surface sensitive region above $z = 0$.

At the vicinity of plasmonic metamaterials, the evanescent plasmonic fields can be represented by a sum of electric fields with wavevectors tangential to the surface plane, i.e; $k_x\hat{\boldsymbol{x}}, k_y\hat{\boldsymbol{y}}$. As we would see in Section 4.3.1 and Figure 7.5, the plasmonic fields are characterized by large tangential wavevectors where k_x, $k_y \gg k_0$ and k_0 is the propagating wavevector. In the weak field limit, all of the plasmonic fields could be approximated to couple as an independent sum to the atomic excitations, each of them with much larger Doppler shift than that created by the propagating field ($k_0 z$) in the evolution of the density matrix component σ_{eg} in Equation (2.22). Large Doppler terms of $k_x v_x$ & $k_y v_y$ in the integral $\mathcal{L}(z)$ in Equation (2.26) results in much broader detuned contribution to $\bar{\chi}$ by the plasmonic fields, which is far away in detunings from the contribution to $\bar{\chi}$ by the propagating optical field. Therefore in our analysis in upcoming sections, we can analyse the Doppler-free SR spectra in terms of only the propagating field and model the plasmonic metamaterials as a homogeneous material with an effective mean-field refractive index which affects the SR spectra via $r^*\rho$ as explained in Section 2.2.3.

2.2.6 Discussion

In this section, we illustrate the behavior of the frequency modulated selective reflection spectra with various surface parameters. This would give us some insights on the influences of the plasmonic layers and ΔC_3 on the selective reflection lineshapes in general. We plot the theoretical selective reflection curves of Equations (2.18) and (2.19), taking the modulation frequency $\omega_m = \gamma$, which is approximately the modulation frequency regime that our experiments are done in.

We define a dimensionless van der Waals parameter $A = 2\Delta C_3 k^3/\gamma_{eg}$ and plot the lineshapes with various A values in Figure 2.2 with no plasmonic phase

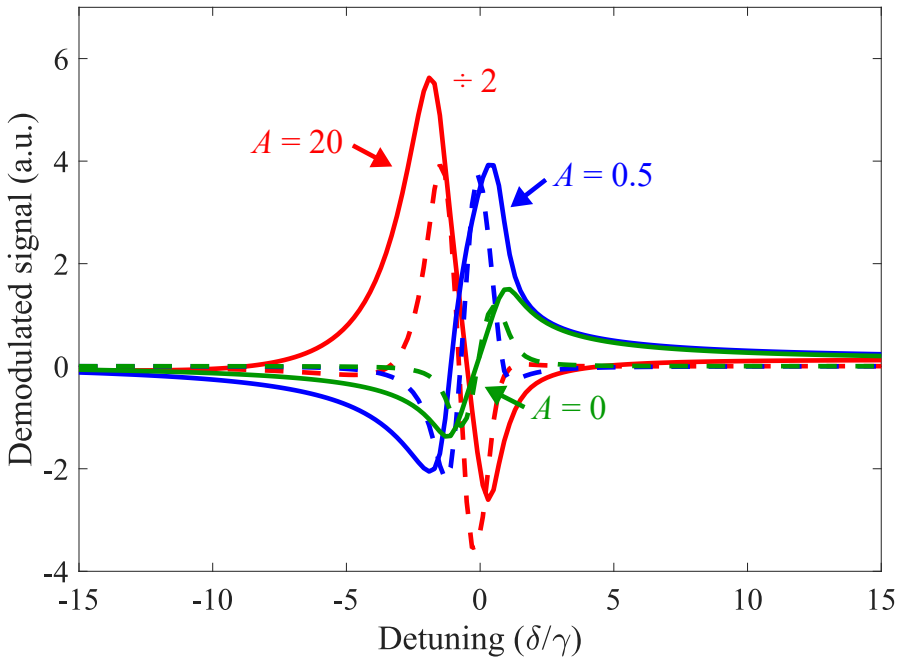

Figure 2.2: Comparison of selective reflection spectra with (a) (green) $A = 0$, (b) (blue) $A = 0.5$, (c) (red) $A = 20$. The red curve magnitude is reduced by 2 times for visual clarity. Solid lines are the in phase signals and in dashed lines are the quadrature signals.

shift. In green, the spectrum corresponds to an atomic transition without van der Waals interaction. We see that the spectrum is anti-symmetric around $\delta = 0$. Progressing from blue to red, the surface interaction A is increased from 0.5 to 20. We see that as A increases, the spectra: i) magnitude increases, ii) get more asymmetric, iii) experiences larger red shift of the line center; i.e. $\Delta C_3 > 0$ in Equation (2.24) where the red shift in frequency is a characteristic of the surface van der Waals interaction, iv) flips in sign for an enormous A; enourmous attractive van der Waals potential with the surface, which is not the regime our experiments are performed in.

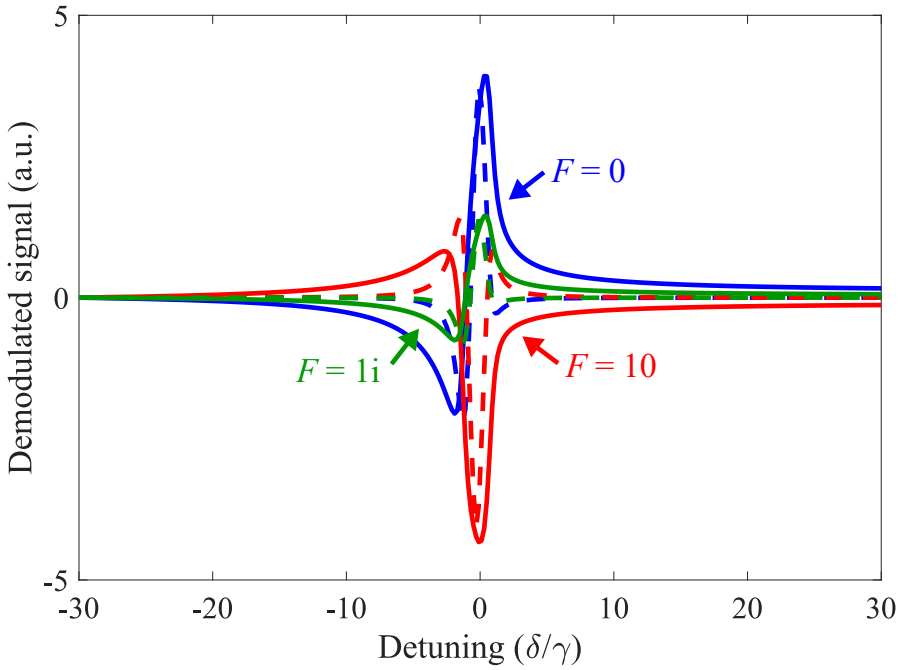

Figure 2.3: Comparison of the selective reflection spectra with (a) (blue) $F = 0$, (b) (red) $F = 10$, (c) (green) $F = 1i$. Solid lines are the in phase signals and in dashed lines are the quadrature signals.

Next, we introduce plasmonic layer phase shift (see Equations (2.8) and (2.11)) to the system where we define a normalized term $F = r_0^* \rho / 2R_0$. we fix the $A = 0.5$ for all curves to illustrate the behavior of F clearly in Figure 2.3. The blue curve is the same as the blue curve in Figure 2.2 where there is no plasmonic phase shift and $A = 0.5$. In red is the spectra with positive phase shift $F = 10$. This results in a flip in the sign in the curve

(compare with (a)) due to the approximately π rotation in phase. In blue. we have an imaginary $F = 1i$ where the effect is purely an absorption to the SR spectrum. This effect could come from the imaginary part of the refractive index of the plasmonic layer for instance.

We give a comparison between the effect of the Van der Waals interfaction A and the plasmonic layer phase shift F on the spectrum. Non-zero value of A causes a frequency shift in the spectrum but F does not. Both non-zero values of F and A cause an asymmetricity in the lineshape and both sufficient high values of F and A flip the sign of the spectrum. It is also possible for the asymmetricity effect from F to compensate for the asymmetricity effect from the Van der Waals interaction A. which has been reported by Chevrollier and co-authors [57]. In practice, in order to avoid misleading interpretation between F and A, we first extract the value of F using the reflection and transmission measurements on our metamaterial interface before fitting our slective reflection curve to obtain A. This point will be discussed in detail in Chapter 4.

2.3 Conclusion

In this chapter, we lay down the theoretical foundations of frequency modulated selective reflection spectroscopy for deriving the results in the following experimental sections. The derivation for frequency modulated selective reflection theory is done assuming the incident beam is normal, atom-light coupling is in the linear regime, frequency modulation index is small and Doppler width is much larger compared with the natural atomic linewidth and atomic vapor is dilute, which all of these assumptions are valid in our experiments. Equally important, the arguments for the surface-sensitive and velocity-selective property of frequency modulated selective reflection is presented in relations to the theoretical expression. To give a flavour of the frequency modulated selective reflection spectroscopy to the reader, we show in the discussion section, the theoretical curves to illustrate the behavior of the i) Van der Waals interaction, ii) dielectric and plasmonic inter-layer on the frequency modulated selective reflection lineshapes. This should prepare the reader to understand our results on hot atom vapor close to a plasmonic metamaterial surface discussed in Chapters 4, 5 and 7.

Chapter 3

Experiment design and setup

This chapter describes the experimental design and procedures applicable to the following chapters dealing with hot atomic vapor (Chapters 4 to 7). The first section describes the construction of vacuum chamber that houses the hot cesium vapor. In its subsections, we discuss the technical design of the atoms-metamaterial interface on dielectric window and on fiber. This is followed by Section 3.2, a discussion on the metamaterial fabrication and designs. Section 3.3 describes how we image the laser beam shape for an optimum overlap with the metamaterial arrays for Chapters 4 and 7. Section 3.4 iterates the frequency stability of lasers required for the experiments. Subsequently, the next section, Section 3.6 elaborates on the methods to stabilize the frequency drift of the laser. Section 3.7 explains the procedures to obtain vapor temperature from the absorption of cesium bulk vapor.

3.1 Design and construction of the ultra-high vacuum system

For large majority of the experiments on hot atomic vapor in this thesis (Chapters 4, 5 and 7) , the Cesium atomic vapor is contained in a stainless steel ultra-high vacuum (UHV) chamber. The chamber is shown in Figure 3.1. A vacuum valve controls the flow to the turbomolecular pump and the mass spectrometer and another valve controls the gate for diffusing cesium vapor to the main chamber. The main chamber consists of a spherical cube from Kimball Physics (Model No: MCF275-ExpCube-C6A8) with six expanded DN40 ports allows flexibility in mount. Commercial silica viewports are

mounted on one optical axis for transmission measurements (Section 3.7 for transmission measurement), and wedge window viewports or fiber feedthrough are mounted on another axis to do the selective reflection measurements. More information on the technical design of customized wedge viewport and fiber feedthrough designs are explained in Sections 3.1.1 and 3.1.2 respectively.

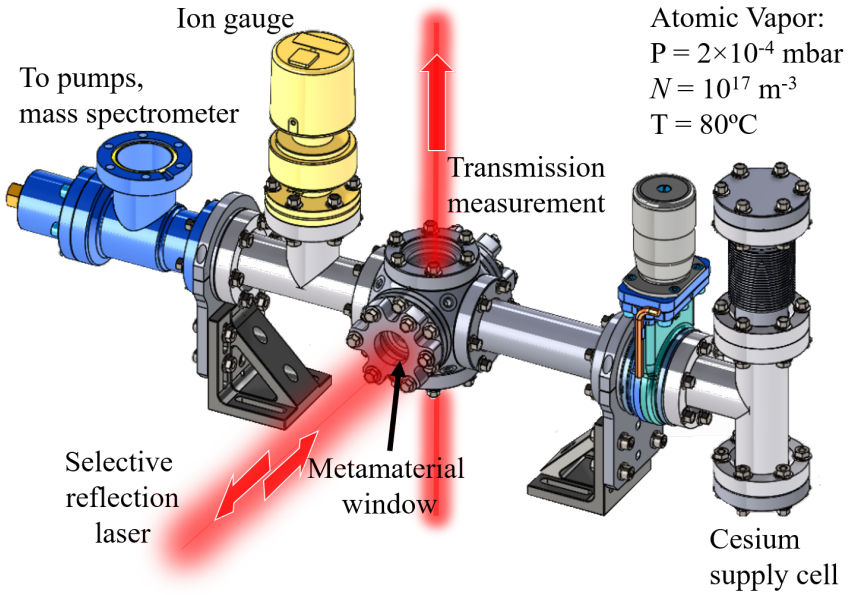

Figure 3.1: Main chamber for hot atomic vapor experiments. On the top right are the typical pressure, density and temperature of the atomic vapor in the chamber.

The source for the cesium is a commerical 1 gram of cesium ingot sealed in glass tube bought commercially which we house in the reservoir section. UHV vacuum is obtained by baking the whole chamber with heat tapes before releasing the cesium. The heat tapes are also used for maintaining the vapor temperature in the experiment. A mass spectrometer and an ion gauge are used to measure the remnants gases and satisfactory vacuum level of 1×10^{-8} mbar is achieved. The cesium is released by crushing the ingot via tightening the bellow at the reservoir. Transmission through the Kimball chamber (See Section 3.7) is used to monitor the cesium density in the main chamber.

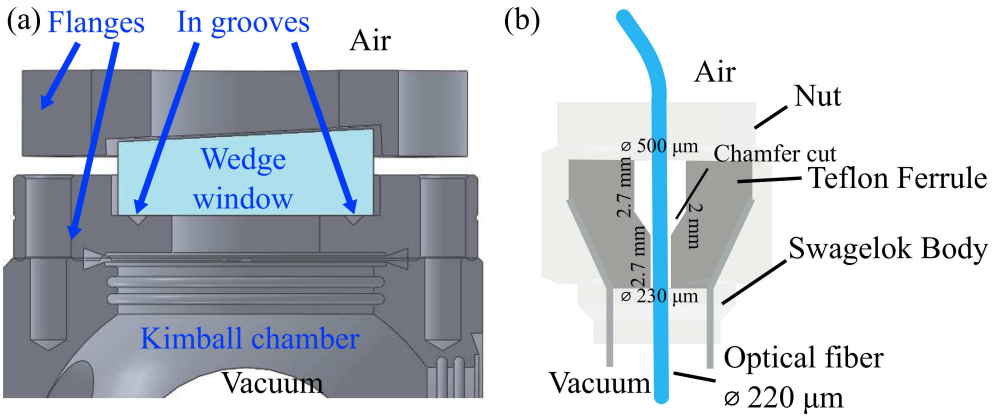

Figure 3.2: (a) Cross-section of the wedge viewport design. The angle of the wedge window is 3°. The wedge window (with or without metamaterial) sits on the bottom flange. Indium wire is placed in a machine groove for tight vacuum seal. Tightening of the top flange to the Kimball chamber with vacuum screws compresses the indium wire and forms an ultrahigh vacuum seal around the circumference of the wedge window. (b) Cross-section of the vacuum seal ferrule.

3.1.1 Wedge window on the UHV system

Multiple internal reflection on the glass layer create unwanted inteference on the selective reflection signal. For atom-metamaterial experiments in Chapters 4 and 7, we design an easily dismountable angled wedge window to avoid this issue. The design also allows for easy removing of the window for metamaterial fabrication process. The design of the wedge window and the holder are shown in Figure 3.2(a). To make an UHV compatible seal, the contact surface of the wedge window with thechamber flange is lined with 1 mm diameter indium wire. The indium wire behaves like a malleable metal that forms a tight seal when compressed. We operates the chamber at temperatures lower than the melting point of indium (150 °C) for our experiments and a good vacuum level ($< 10^{-8}$ mbar) is obtained.

3.1.2 Optical fiber feedthrough

For the experiment of atoms on the tip of the fiber (Chapter 5), an reliable and reusable way of placing the fibers whilst minimizing vacuum leak is

needed. This is done using a Teflon ferrule as the sealing gasket in a Swagelok connection See Figure 3.2(b).

At the center axis of the Teflon ferrule, a 220 µm diameter hole is drilled from the bottom and 500 µm hole is drilled from the top. A chamfer cone hole is done (See figure) at the middle of the ferrule. This allows optical fiber of up to ≈ 220 µm in diameter to feedthrough into the chamber. When tightened by the Swagelok nut, the seal is formed at the tightest point of the chamfer. After tightening, leaks are tested at various temperature to $T_{\max} = 230°\text{C}$ by using a helium test with a mass spectrometer as well as on vacuum gauge reading. The seal over the fiber has a consistent good vacuum performance ($< 10^{-8}$ mbar) throughout the experiment. The Teflon seal only leaks if the chamber is cooled down too fast due to contraction of Teflon. The leak can be stopped easily by tightening the Swagelok nut by a quarter range. No leaks are detected in the cooling cycles if the chamber is cooled down slowly at 3 - 4 K/hour.

3.2 Metamaterial design and fabrication

3.2.1 Metamaterial design

Both silver and gold are appropriate material for plasmonic application for ther relatively low losses in near infra-red (NIR) region [66]. However as gold reacts with cesium [67], silver is instead chosen as our plasmonic material for its inertness with cesium atom. For experiments by optical excitation with free space lightbeam (Chapters 4 and 7), a 50 nm thick layer of silver is thermally evaporated on top of a vacuum compatible wedge window Section 3.1.1 and another 8 nm protective layer of silicon dioxide is thermally evaporated over the silver layer. For experiments by optical excitation through optical fiber (Chapter 5), a 50 nm thick layer of silver is thermally evaporated on top of the cleaved tip of a commercial Thorlabs FG200UEA multimode silica fiber and a 3 nm thick layer of silicon dioxide protective coating is then evaporated on top of the silver layer. An extra 5 nm thick layer of silver is further coated on the sidewalls of the fiber to extinguish evanescent electric field leakages outside the fiber from the higher order cladding modes.

This thin silicon dioxide layer protects the silver layer from being tarnished by trace materials present in the Focused Ion Beam machine (FIB). Metamaterials are engraved on the deposited layers by FIB beam. Figure 3.3(a)

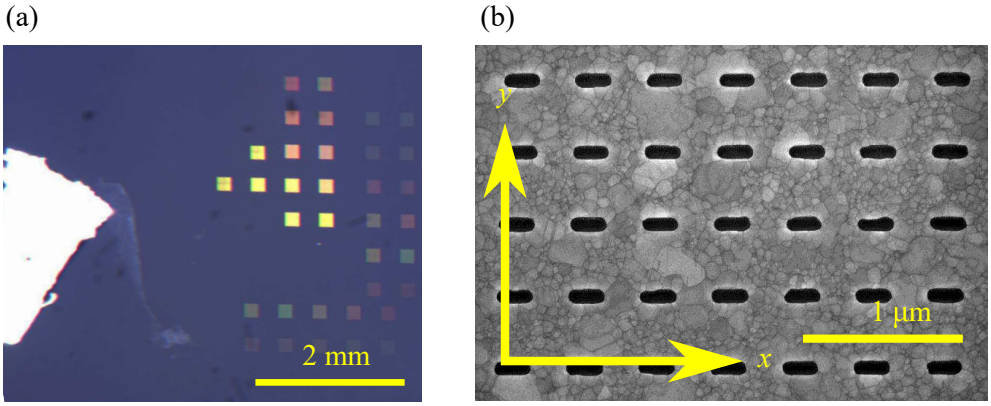

Figure 3.3: (a) Image of the metamaterial on dielectric window. Each colored square is one array of metamaterial (200 µm by 200 µm). White area on the left is dielectric window with no deposition. (b) Scanning electron microscope image of the slit metamaterial.

depicts the pictures taken of the metamaterial deposited on the inner surface of the dielectric wedge window.

Two types of geometries are used for the metamaterials. For experiments by optical excitation with free space lightbeam (Chapters 4 and 7), negative slits are engraved on the silver layer. Each of this slit behaves like a plasmonic resonator with a polarized light perpendicular to the slits. On the other hand, polarized light parallel to the slits does not excite the plasmonic resonance. By changing the sizes and the periodicity of the cavity, the wavelength of plasmonic resonance can be tuned. Section 3.2.2 explains the measurements of the plasmonic resonance of metamaterials in our experiment. Figure 3.3(b) shows scanning electron microscope (SEM) image of the metamaterial.

For experiments by optical excitation through optical fiber (Chapter 5), a two-dimensional array of 185 nm outer diameter, and 155 nm inner diameter plasmonic metamaterial rings is engraved on the silver layer. The period of the array is 370 nm and the metamaterial covers fully the surface of the fiber core. Rings metamaterial instead of slits are engraved because rings possess rotational symmetry, which responses isometrically to light polarization as we are using a non-polarization maintaining multimode optical fiber. Other rotational symmetric designs were initially considered but rings metamaterial are chosen as they possess well frequency separated plasmonic resonance. The optical reflection measurements of the metamaterials designs considered is

Table 3.1: Table of metamaterials dimensions and optical characterizations

#	Resonance λ (nm)	Dimensions (nm)			852nm	852nm
		length	width	period	Transmission	Reflection
1	973	246	70	540	2%	96%
2	943	237	70	520	4%	89%
3	898	228	70	500	8%	73%
4	858	219	70	480	19%	42%
5	820	210	70	460	26%	28%
6	795	201	70	440	23%	47%
7	770	192	70	420	14%	67%
8	740	183	70	400	13%	74%
9	707	174	70	380	7%	87%
10	668	165	70	360	8%	88%
11	615	149	90	328	19%	84%

Metamaterials 1-10 are prepared for the Casimir-Polder tuning experiment in Chapter 4. Metamaterial 11 is prepared for investigation on localized plasmon coupling with electric quadrupole transition in Chapter 7.

shown in Section 3.2.4.

3.2.2 Metamaterial experimental characterization

Reflection measurements with vertical polarization with white light on the metamaterials are performed on a Jasco MSV5200 microspectrophotometer machine. The reflection curves are shown in Figure 3.4. The geometry of the slits with longest plasmonic resonance wavelength is 246 nm length and 70 nm width (See Table 3.1). Starting from the slit above mentioned, the length and period are decreased in steps of 9 nm and 20 nm respectively while the width is kept constant at 70 nm. By keeping the ratio of period and the length fixed for all metamaterials at 2.2, the plasmonic resonance linewidth is kept fixed at 85 nm or 35 THz while the central resonance is tuned across 970 nm to 615 nm (Column 2 of Table 3.1).

After the metamaterial window is mounted onto our vacuum chamber and hot cesium is introduced into the chamber, transmission and reflection measurements with our diode laser at $\lambda = 852$ nm is conducted on each metamaterial. The laser frequency is detuned to a few of GHz away off

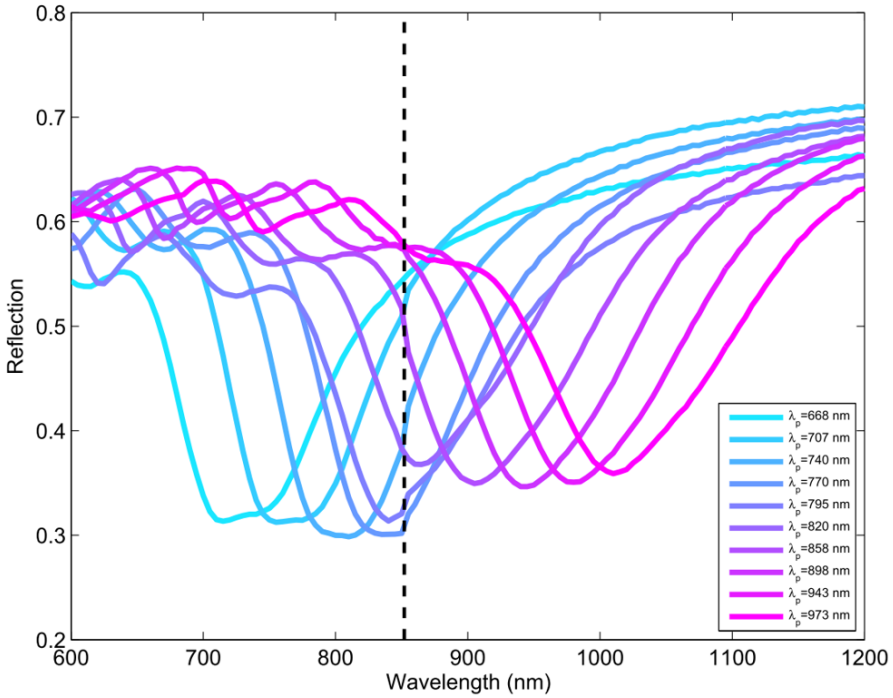

Figure 3.4: Reflection spectra of the metamaterials prepared for Chapter 4. Incident light polarization is perpendicular to the slits. The reflection spectrum of the metamaterial for Chapter 7 is shown in Figure 7.1b.

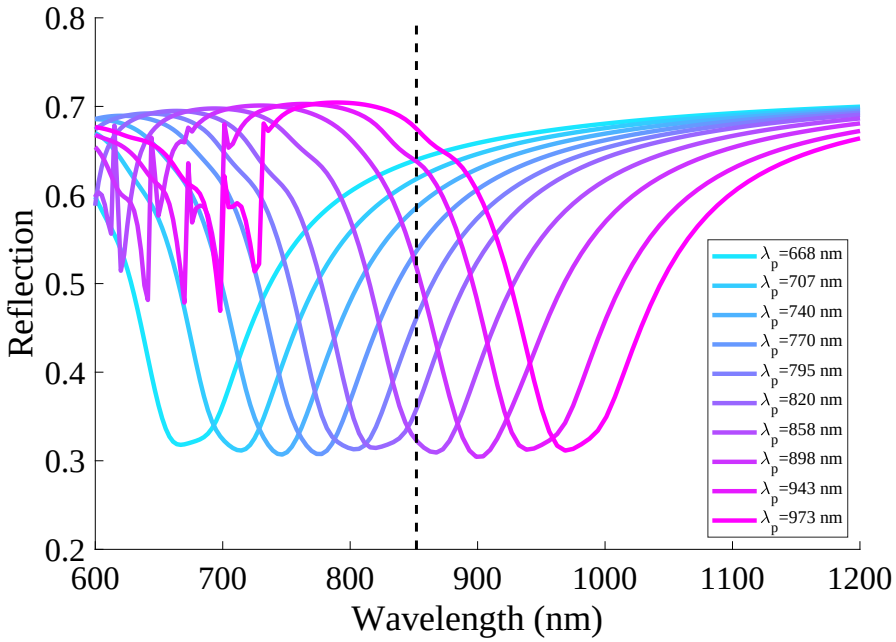

Figure 3.5: Reflection spectra of the metamaterials prepared for Chapter 4 from Finite Difference Frequency Domain simulation. Incident light polarization is perpendicular to the slits. The simulated reflection spectra demonstrate the same plasmonic characteristics with that of experimental reflection spectra in Figure 3.4.

resonance from the Cs D2 transition to avoid absorption of light by the cesium vapor in the chamber. The measurements with the laser, shown in columns 4 and 5 of Table 3.1, display a consistent plasmonic behavior with the spectra on the microspectrophotometer machine with white light illumination. This shows that our metamaterial is preserved against attacks from the reactive cesium gas.

3.2.3 Fitting optical transmission and reflection of metamaterial

We perform a Finite Difference Frequency Domain (FDFD) simulation of the metamaterials in Chapter 4. We extract the expected far-field reflectance and transmittance intensities of the metamaterials. The reflectance and transmittance intensities show good quantitative agreement with the experimental data (See Figure 3.5 and Figure 3.4). However, we perform a global adjustment of the contrast of the reflectance and transmittance of the FDFD results by a factor of 0.7 and 0.5 respectively. This adjustment accounts for frequency independent optical losses, not encountered in the FDFD simulation. Contributions may come from photon scattering at the metamaterials, imperfect size matching of the beam to the metamaterial or possible long-range inhomogeneity of the metamaterial geometry. The results are summarized in Figure 3.6. The error uncertainty of the results are 10 nm in the experimental plasmonic resonance. The good agreement demonstrates consistency between our simulation and experimental data and justifies the extraction of the effective index of refraction of the metamaterial n' and the quantity $F = r_0^* \rho / 2R_0$ depicted in Section 2.2.3 from our FDFD simulation in Section 4.3.3.

3.2.4 Isotropic metamaterial experimental characterization

Figure 3.7 shows the reflection measurements with white light done on metamaterials with rotational symmetries of the same diameter and periodicity (185 nm and 370 nm respectively). The characteristics of a good candidate for

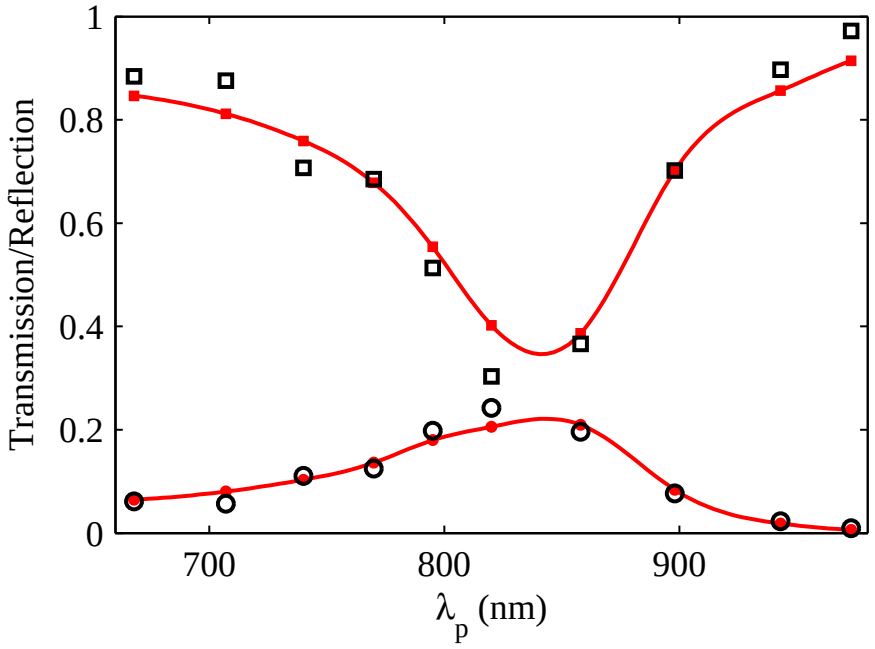

Figure 3.6: Experimental reflection (open squares) and transmission (open circles) of the ten metamaterials measured with the 852 nm laser. The x-axis corresponds to p, the position of the plasmon resonance of each metamaterial. The solid red squares (circles) corresponds to the reflection (transmission) obtained by finite-difference frequency domain numerical simulation. The lines, connecting simulation results, are guides for the eye.

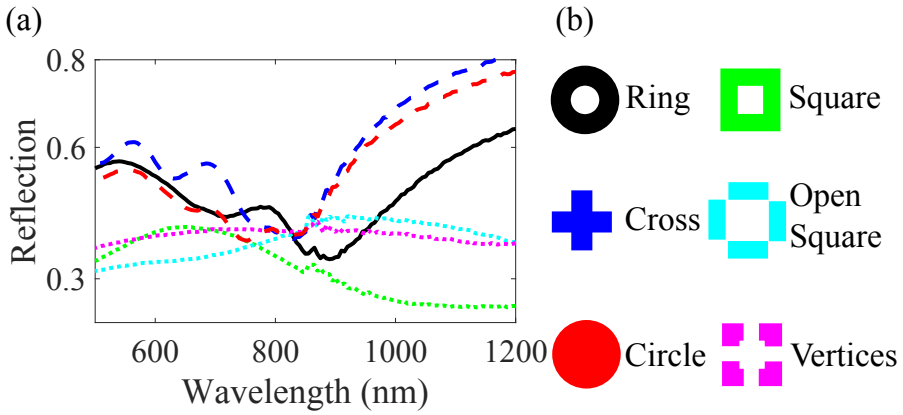

Figure 3.7: (a) Reflection measurements of different rotational symmetric metamaterials designs with the same diameter. Corresponding metamaterial shapes to the curves are; black - ring, blue - cross, red - circle, green - square, cyan - open square, and magenta - vertices.(b) Sketch of the shapes of metamaterials tested. The light polarization is in the vertical direction.

atom- metamaterial surface selective reflection spectroscopy would be a sharp and distinct plasmonic resonance. Of all shapes tested; squares, open squares and vertices have resonances that are very broad. Since the metamaterial resonances lie in the red, using them would necessitate much smaller diameter, which would be difficult to control during fabrication. Rings, circles and crosses possess the good characteristics of comparatively narrow resonances. Ring metamaterial, among all the shapes, is chosen for experiment on optical fiber in Chapter 5 because the zero order and first order resonance are well-separated (Compare solid black curve and dashed curves in Figure 3.7).

3.3 Optical imaging of metamaterial

In our experiments probing $\lambda = 852\,\text{nm}$ electric dipole transition (Chapters 4 and 7), we excite the transition with intensities below the saturation intensity of the transition to avoid saturation effects. This limits the collection intensity on our detector. To ensure we get maximum signal, we make sure that the whole array of metamaterials are evenly illuminated by doing an imaging of a 200 µm by 200 µm square mask on the metamaterial. The square mask is constructed by overlapping two commercial Thorlabs slit apertures with

a width of 200 µm orthogonal to each other. The schematics is shown in Figure 3.8. Motorized mirror in vertical and lateral axes are done to move the beam from one metamaterial array to the next. By maintaining the distances from the square mask to the lens and the metamaterials window at focus distance f, we retain even illumination on the entire array of metamaterials when translating the beams horizontally and vertically from one set of metamaterial to the next.

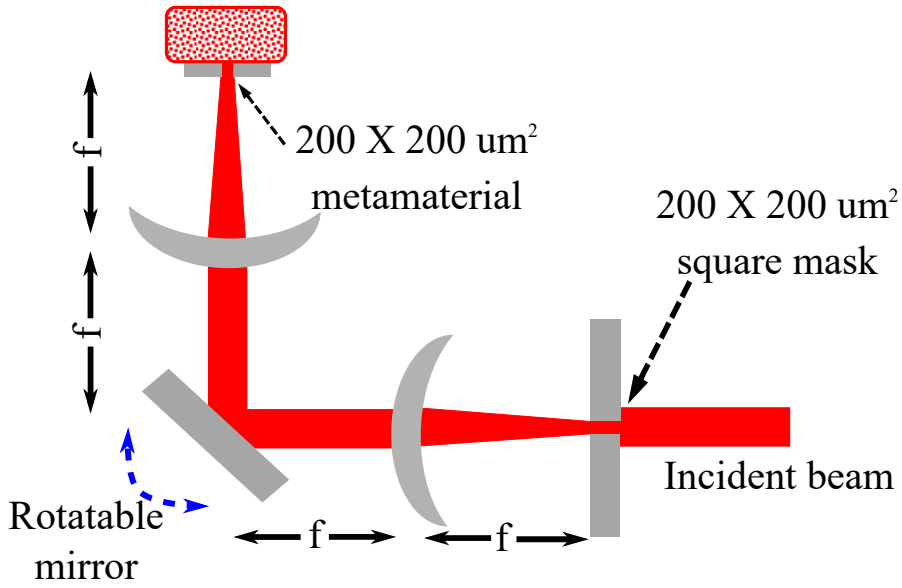

Figure 3.8: Schematic of the imaging system. The rotatable mirror at focus distance f translates the beam between different sets of metamaterial while maintaining the size and shape of the square beam.

3.4 Diode lasers stability

In all the experiments, we use commercial diode lasers tuned to $\lambda = 852\,\text{nm}$,and 685 nm as the sources of optical excitations. The experiments on metamaterials typically take hours to days of integration time in comparison of matter of minutes for that of dielectric window. This is due to the light collection area is limited by the $200\mu m \times 200\mu m$ structured area for the metamaterial case. The long averaging time requires us to ensure the frequency stability of the lasers in the experiments during this time span. To have an idea of

the frequency stability required for the experiment, we need to compare the linewidths of the atomic transitions versus the frequency drift of the lasers in our experiments. Figure 3.10(a) shows the typical frequency drift of few hundred MHz over 12 hours. The drift are much larger compared to the natural linewidth of $6^2S_{1/2} - 6^2P_{3/2}$ and $6^2S_{1/2} - 5^2D_{5/2}$, that is 5.2 MHz and 123 kHz respectively, it is evident that frequency compensation and/or stabilization mechanisms are needed.

For the $6^2S_{1/2} - 6^2P_{3/2}$ electric dipole (E1) transition at 852 nm, an averaging technique is done for Chapters 4 and 5 and standard frequency locking to the peak of the transition in a hole-burning spectroscopy is done for Chapters 6 and 7. The averaging technique is described in Section 3.5 and frequency locking mechanism is detailed in Section 3.6. Conversely, locking $6^2S_{1/2} - 5^2P_{5/2}$ electric quadrupole (E2) transition by hole-burning spectroscopy is challenging because of the weak saturation effect of electric quadrupole interaction. A novel optical pumping method is devised to overcome frequency locking mechanism and is elaborated in its own chapter in Chapter 6.

3.5 Hole-burning spectroscopy based averaging technique

To obtain a good signal to noise ratio on our selective reflection experiments in Chapters 4 and 5, the acquisition of data take hours to days of integration time. However, averaging the signal to get the results over a timespan of hours and days needs to frequency drifting of the laser. The experiment is done with a free-running diode laser. We track the saturation (hole-burning) spectrum drift by minimizing the residue between the differences in each subsequent run of data of saturated spectrum and averaging our selective reflection data by compensating for the relative drift of the saturation spectrum over time .

The signal at M run, $f_M(x)$, is translated by $X \Rightarrow f_M(x+X)$:

$$\Delta f_M(x+X) = f_M(x + X) - F_{M-1}(x) \tag{3.1}$$

where $F_{M-1}(x)$ is the averaged signal for all previous runs, $\Delta f_M(x+X)$ is the difference between current signal at M run translated by X and the averaged signal.

The differences for each translation, X, is summed up to get the residue for X, S_M^X.

$$S_M^X = \sum_x |\Delta f_M(x + X)| \tag{3.2}$$

The signal is translated by X_M with the minimum residue, $S_{M(min)}^X$ and added to the average till M runs, $F_M(x)$.

$$F_M(x) = \sum_N^M \frac{f_M(x + X_M)}{M} \tag{3.3}$$

We track the drift of the laser in each run M by tracking X_M. The advantage of this method is that the method is insensitive to the profiles of the reference signal, provided that the first data has sufficient signal to noise ratio, which we have in a single shot of data. Figure 3.9 shows an example from an experiment run in Chapter 4 for two acquisition timescale; 3 minutes and 12 hours respectively that we perform with this technique. The noise of the signal is reduced to 6×10^{-4}V after 12 hours of averaging, which allows us to resolve the profiles of the selective reflection signal clearly.

3.6 Laser lock

3.6.1 Experimental setup

This section explains the optical and electronic setup used to stabilize the frequency of the 852 nm laser. The setup scheme is illustrated in Figure 3.10(b). A 1 MHz signal is generated by a function generator and supplied to a homemade circuit board. An impedence matched potential divider on the board (labeled *) separates the 1 MHz oscillations into two, one supplied directly to the AC current modulation port of the diode laser and another to the local oscillator port of a frequency mixer (Model: Mini Circuits ZX05-1L+). The laser beam passes through a frequency hole-burning setup [68] and the probe beam is collected on an amplified silicon detector. The collected signal is sent back to the error signal generation circuit. The circuit consisting of a mixer and a low pass filter is further described in Section 3.6.2. The generated error signal from the circuit is sent to a Proportional-Integral-Derivative (PID) laser servo (Model: Vescent D2-125) which compensates

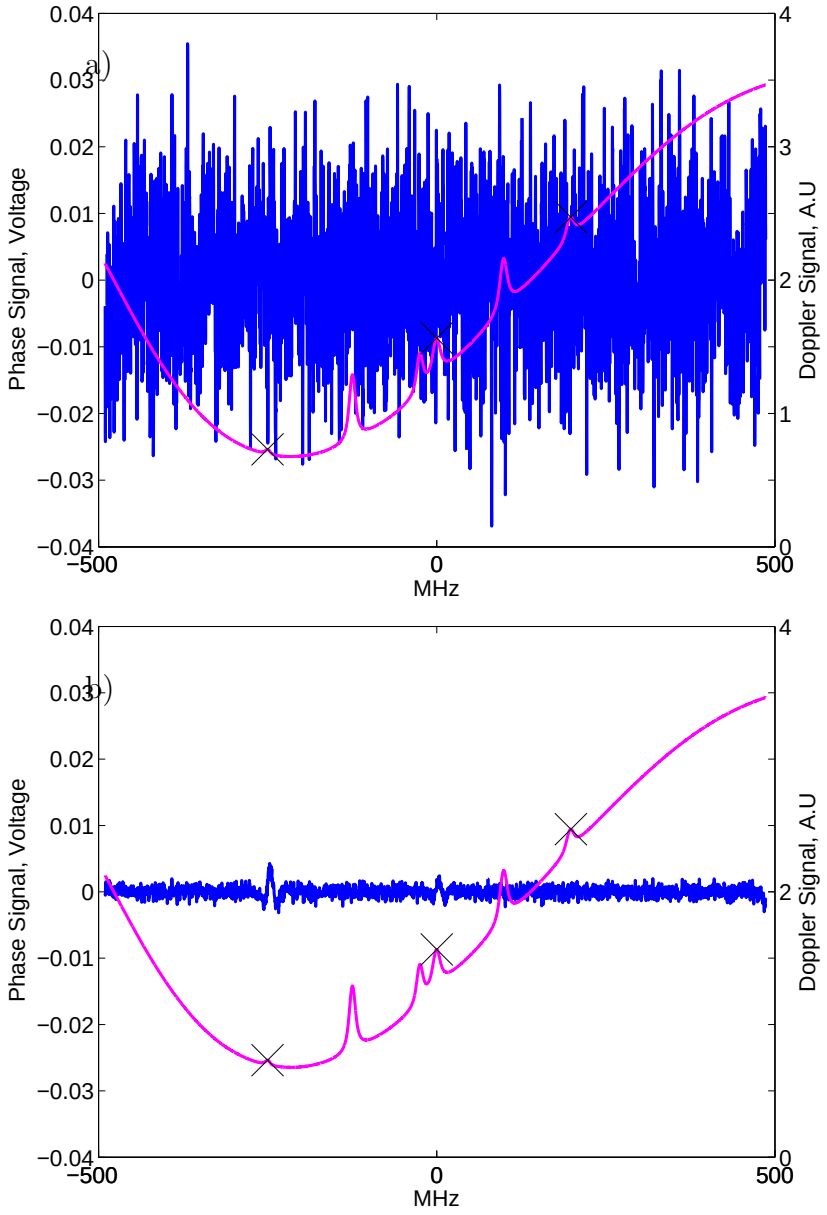

Figure 3.9: The two plots show the selective reflection signal (blue) referenced to the saturation spectrum (pink). The three crosses on the pink curve marks the position of the 3 hyperfine atomic transition. a) Figure shows the demodulated signal for an acquisition of 3 minutes, b) Figure shows the signal after integration for 12 hours.

for the drift of the laser. The servo output (control signal) goes to the DC current modulation port of the diode laser which modulates the laser current to compensate for the laser frequency drift. The entire schematics makes an active feedback loop to stabilize the laser frequency around a set point.

3.6.2 Reference signal splitter and error signal generation circuit

The error signal generation circuit (Figure 3.11) consists of 3 parts: A potential divider, a frequency mixer and a low pass filter. In the first part, the potential divider serves two purposes: 1) Impedence matching and 2) splitting the reference input voltage to the diode laser for current modulation and the frequency mixer for frequency reference in a 1:4 ratio.

On another side, the feedback signal from hole burning setup is amplified with a broadband amplifier (Mini Circuits ZX60-43+) and is sent to the radio frequency port of a frequency mixer (Mini Circuits ZX05-1L+). The frequency mixer mixes the reference and feedback signals. The frequency summed components of the mixed signal is filtered out by a home-made low-pass-filter circuit. The remaining frequency difference gives an error signal. This is done by sending the output from frequency mixer through a low-pass-filter circuit. We choose a second order Bessel type low-pass-filter design which is a relatively simple design but still offer us a sufficient gain on the lock signal. The model of operational amplifier we used is Analog Devices OP27G. The equations for the circuitry are [69]:

$$A(f) = -\frac{\mathrm{R_2/R_1}}{1 + i(2\pi)^2 f_c f \mathrm{C_1(R_2 + R_3 + R_2R_3/R_1)} - (2\pi)^4 (f_c f)^2 \mathrm{C_1C_2R_2R_3}} \tag{3.4}$$

$$\mathrm{A_0} = -\mathrm{R_2/R_1} \tag{3.5}$$

$$\mathrm{R_2} = \frac{a_2 \mathrm{C_2} - \sqrt{a_1^2 \mathrm{C_2^2} - 4 b_1 \mathrm{C_1 C_2 (1 - A_0)}}}{4\pi f_c \mathrm{C_1 C_2}} \tag{3.6}$$

$$\mathrm{R_3} = \frac{b_2}{4\pi^2 {f_c}^2 \mathrm{C_1 C_2 R_2}} \tag{3.7}$$

where the respective $\mathrm{R_i}$ and $\mathrm{C_i}$ are the resistors and capacitors values in Figure 3.11(a). $\mathrm{A_0}$ is the filter gain at DC value. $a_2 = 1.3617$ and $b_2 = 0.6180$ are the characteristic parameters that characterize the Bessel filter. $A(f)$

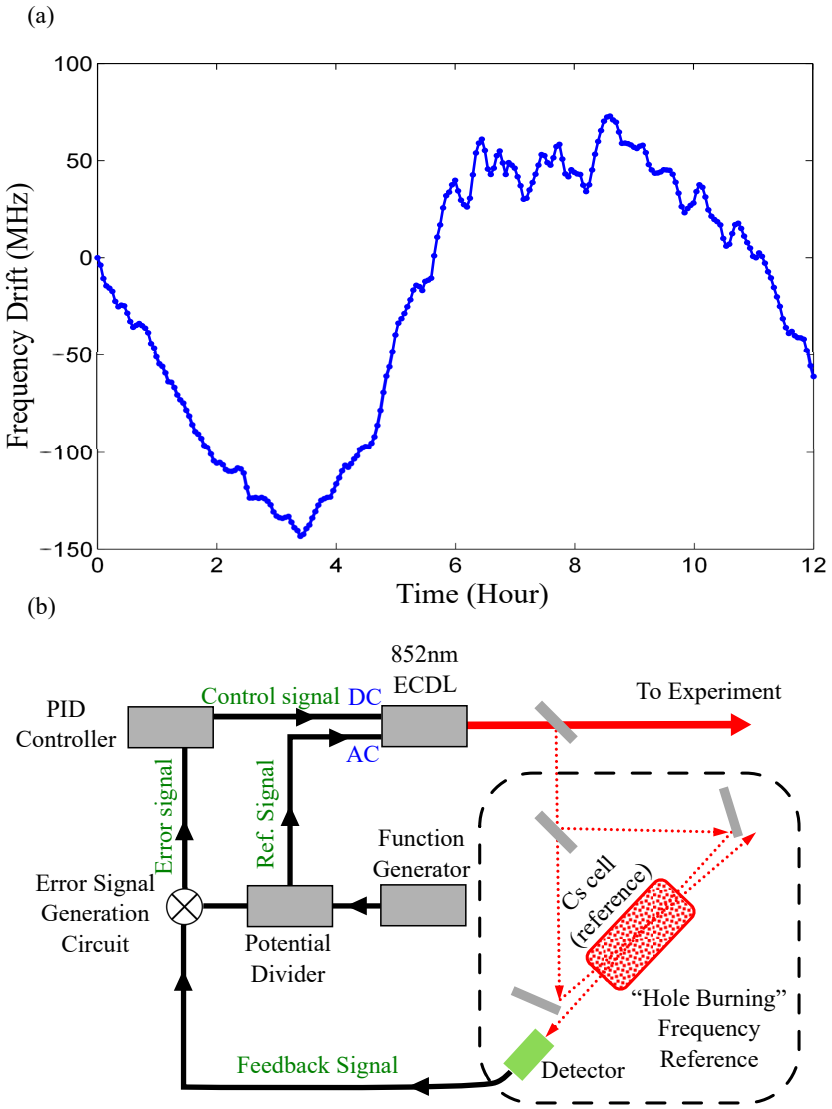

Figure 3.10: (a) Drift of the unlocked 852 nm laser over a period of 12 hours, in a typical timespan for one experimental run. (b) Schematic of the laser lock. Potential divider splits the reference signal into two; one to modulate the laser current and another as a control signal at the mixer. The feedback signal from the detector is mixed and filtered to get the error signal. This is sent to the commercial proportional-integral-derivative controller to generate feedback signal on the laser current. ECDL: External Cavity Diode Laser. PID: Proportional-Integral-Derivative

gives the response of the circuit with an input with frequency f and is termed as the transfer function of the filter.

There are five electronic values to decide with three simultaneous equations and thus we have the two additional degree of freedom. We choose the capacitors to be $C_1 = 1\,\text{nF}$ and $C_2 = 33\,\text{nF}$. The resistors values are then selected based on Equations (3.5) to (3.7) to give the designed gain of $A_0 = 30$ and $f_c = 8\,\text{kHz}$. A variable resistor for R2 (in dark brown) allows the tuning of the error signal gain, $A_0 \leq 30$ when needed. The resultant error signal is sent to the PID controller to generate a servo signal which is sent to the laser to compensate for the drift.

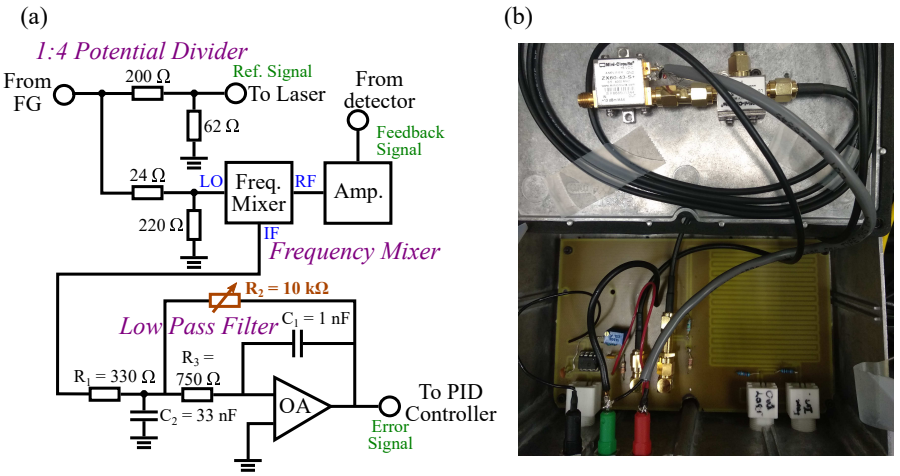

Figure 3.11: (a) Schematic of the error signal circuit. FG: 1 MHz from function generator, Ref. Signal: Reference signal, Freq. Mixer: Frequency mixer, Amp.: Broadband amplifier, OA: Operational amplifier. In blue are the 3 ports of the frequency mixer; LO: Local oscillator, RF: Radio Frequency, IF: Intermediate frequency. (b) Photo of the homemade error signal circuit. Top half of the picture is the frequency mixer and broadband amplifier. Bottom half is the printed circuit for potential divider and low pass filter.

3.7 Cesium pressure characterization

In the selective reflection spectroscopy of hot vapor in non-saturated regime, the signal amplitude is proportional to the atom vapor density. An useful and easy way to increase the signal is to increase the vapor density by increasing

the vapor temperature;i.e. an increase of 30°C increases the density by roughly an order of magnitude. In this section, we enumerate the method to calibrate the vapor density in our experiment by transmission spectroscopy technique. We send the 852 nm laser through the vacuum chamber and the transmission of laser through the bulk vapor versus laser detuning is measured. The transmittance through a homogeneous bulk medium is

$$\mathcal{T}(\delta) = e^{-\sum \alpha_i(\delta) L} \tag{3.8}$$

where L is the thickness of the medium, α_i is the absorption coefficient of a particular hyperfine transition i at laser detuning δ. For a particular resonance, the dependence of the absorption coefficient, $\alpha(\delta)$ on frequency detuning δ, is [70]:

$$\alpha(\delta) = kC_i^2 d^2 N \frac{1}{2(2I+1)\hbar\epsilon_0} \frac{S^I(\delta)}{ku} \tag{3.9}$$

Here $k = 2\pi/\lambda$ is the optical wavenumber, C_i is the transition strength, d is the reduced dipole element $\langle L|e\boldsymbol{r}|L'\rangle$, N is the vapor density that is related to temperature T by the vapor pressure model [71], $2(2I+1)$ is the degeneracy of the ground state and I is the nuclear quantum number $= 7/2$ for cesium, $u = \sqrt{2\mathrm{k_B}T/M}$ is the 1/e width of free gaseous velocity Maxwell-Boltzmann distribution.

The lineshapes represented in S is the convolution of the homogenous and inhomogeneous broadening lineshapes in the atomic vapor.

$$S(\delta) = \int_{-\infty}^{\infty} f(\delta - kv) g(v) dv \tag{3.10}$$

where $f(\delta - kv) = i/[\gamma/2 - i(\delta - kv)]$ is the homogeneous atomic lineshape, $g(v) = 1/(u\sqrt{\pi})\mathrm{e}^{-v^2/u^2}$ is the Boltzmann distribution of velocities. $\gamma = \gamma_0 + \beta_0 N$, in which γ_0 is the natural linewidth and $\beta_0 = 2fcr_0\lambda\sqrt{g_g/g_e}$ is the self-broadening coefficient [72] which takes into account the collisional broadening of atoms, N is the number density of atoms and δ is the laser detuning from transition resonance. f is the oscillator strength of the transition, c is the light speed, r_0 is the electron classical radius, g_g and g_e are the ground and excited states degeneracies respectively. The self-broadening coefficient β_0 comes from atoms-atoms dipole interaction and is measured to be $115\,\mathrm{nHz\,cm^3}$ for cesium D2 transition in literature [40]. At a typical cesium vapor temperature of

$70\,°C$, the self broadening linewidth $\beta_0 N$ is 0.25 MHz, a weak value compared with the natural linewidth of 5.2 MHz for the Cesium D2 line.

The natural atomic lineshape $f(\delta - kv)$ can be expressed in two parts: the real and imaginary parts:

$$\begin{aligned} f(\delta - kv) &= \frac{i}{\gamma/2 - i(\delta - kv)} \\ &= -\frac{\delta - kv}{\frac{\gamma}{2}^2 + (\delta - kv)^2} + i\frac{\frac{\gamma}{2}}{\frac{\gamma}{2}^2 + (\delta - kv)^2} \\ &= f^R(\delta - kv) + if^I(\delta - kv) \end{aligned} \tag{3.11}$$

We can now express S in terms of the real and imaginary part:

$$\begin{aligned} S(\delta) &= S^R(\delta) + iS^I(\delta) \\ &= \int_{-\infty}^{\infty} f^R(\delta - kv)g(v)dv + i\int_{-\infty}^{\infty} f^I(\delta - kv)g(v)dv \end{aligned} \tag{3.12}$$

where S^I gives the Voigt profile of the absorption coefficient in Equation (3.9) and S^R gives the dispersion of the atomic lineshape.

We are particularly interested in evaluating S^I [70] as it gives the absorption strength in the absorption coefficient in Equation (3.9), which we use to determine the vapor density:

$$\begin{aligned} S^I(\delta) &= \int_{-\infty}^{\infty} f^I(\delta - kv)g(v)dv \\ &= \frac{1}{u\sqrt{\pi}}\int_{-\infty}^{\infty} \frac{\frac{\gamma}{2}}{\frac{\gamma}{2}^2 + (\delta - kv)^2} \mathrm{e}^{-\frac{v^2}{u^2}} dv \\ &= \frac{\sqrt{\pi}}{2}\left[\mathrm{e}^{z_+^2} erfc(z_+) + \mathrm{e}^{z_-^2} erfc(z_-)\right] \\ &= \frac{\sqrt{\pi}}{2}\left[\mathcal{F}(z_+) + \mathcal{F}(z_-)\right] \end{aligned} \tag{3.13}$$

where the third line could be derived from the second line by taking the product of Fourier transform of $f^I(\delta - kv)$ and $g(v)$. $erfc(z_\pm)$ is the complex error function, $\mathcal{F}(z_\pm)$ is the Faddeeva function, which are related to each other by:

$$\mathcal{F}_\pm(z) = \mathrm{e}^{z_\pm^2} erfc(z_\pm) \tag{3.14}$$

and $z_{\pm}$ in Equation (3.13) is labeled as:

$$z_{\pm} = \frac{\gamma}{2ku} \pm i\frac{\delta}{ku} \tag{3.15}$$

In the first term, γ contains the homogenous natural linewidth γ_0 and broadening from collisional self broadening $\beta_0 N$. In the second term is the frequency detuning δ from the resonance.

By fitting Equations (3.9) and (3.13) to the transmittance in Equation (3.8) through the cesium chamber with only the temperature, T as the free parameters, and $N = N(T), u = u(T)$, the vapor density in the chamber, N is obtained. Figure 3.12 shows one experimental data on Cesium D2 $6^2S_{1/2}\,F = 4 \rightarrow 6^2P_{3/2}$ transitions. The allowed hyperfine transitions are $F = 4 \rightarrow F' = 3, 4, 5$ which contributes to the absorption. The constants used for the fit are: $k = 2\pi/852\,\text{nm}$, $C_i = [7/72 \quad 7/24 \quad 11/18]$ for $F = 4 \rightarrow F' = 3, 4, 5$ respectively, $d = 3.80 \times 10^{-29}\,\text{Cm}$ [71]. In this figure, the absorption coefficient is contributed from 3 allowed excited states where $\sum_{F'=3}^{F'=5} \alpha_{F'}(C_{F'}, \delta)$. The fit in the figure gives a vapor temperature of 70 °C and an atom density of $2.2 \times 10^{12}\,\text{atoms}\,\text{cm}^{-3}$ and vapor pressure of 767 mTorr.

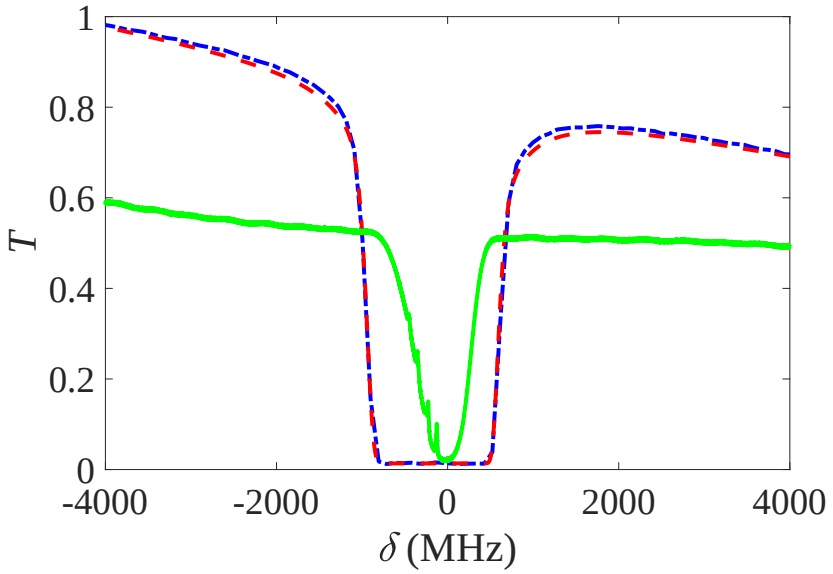

Figure 3.12: One example of the transmission fit. The transmission fit gives a temperature of 70°C. Dashed-dotted blue - Experimental data, dashed red - Theoretical fit, solid green - saturated absorption reference curve.

3.8 Conclusion

In this chapter, we have illustrated the experimental setups and designs for our hot atomic vapor experiments. In Section 3.1, we explain the building block of the chamber that is reconfigurable to adapt to various experiment designs in Section 3.1. We also illustrate the customized design of wedge window which removes multi-reflection from the spectroscopy. This is followed by establishing a proper fiber conduit into the chamber that maintains ultra high vacuum (UHV) vacuum level and resistant to attack from cesium vapor. In Section 3.2, metamaterials used in following experiment chapters were characterized and fabrication parameters were explained. To focus light and maximize the signal from the relatively small array of metamaterials, a 1:1 object to image optical system used is explained Section 3.3. Next, in order to compensate for the laser drift larger than the atomic linewidth, laser lock circuit is designed to lock the laser to a saturated transmission spectroscopy spectrum in a secondary cesium cell. This is illustrated in Section 3.6.2. Equal in importance, the method we used to obtain the cesium pressure in the chamber is presented in Section 3.7. Overall, the chapter gives the reader an idea of the technical method to conduct the experiments.

Chapter 4

Tuning of Casimir - Polder Forces with metamaterial

4.1 Introduction

The Casimir-Polder force has been largely perceived as an obstacle for placing atoms close to surfaces. Nevertheless, ambitious proposals have emerged that suggest the possibility of utilizing atom-surface interactions to achieve tight trapping at record distances from surfaces [22] and in particular photonic bandgap waveguides [73, 74]. The tantalizing possibility of subwavelength atom trapping is made more difficult due to the predominantly attractive nature of the Casimir-Polder interaction that does not allow stable trapping potentials in all directions. Experimental demonstration of an efficient tuning of the atom-surface interaction, particularly between attraction and repulsion represents therefore a milestone in the field of hybrid systems.

Among the various approaches to modify the Casimir-Polder interaction, one relies on the resonant coupling between excited atoms and surface resonances. Thus, experiments with Cesium atoms in high lying excited states next to a sapphire surface have demonstrated resonant Casimir-Polder repulsion [14, 15] or an exaltation of the Casimir-Polder attraction with temperature [75]. The key parameter here, that governs both strength and sign of the Casimir-Polder interaction, is the relative detuning of the plasmonic resonance frequency compared to the predominant atomic dipole coupling (transition). Active engineering of the atom-surface interaction is therefore severely limited by the selection of dielectrics that are available in nature.

An alternative solution would be to use nanostructured periodic planar metamaterials that allow a broad tunability of plasmonic surface resonances across the visible and near infrared spectrum. This spectral domain, where plasmonic or polaritonic resonances are usually scarce in bulk material, is of particular interest since it matches with low-lying transitions of alkali atoms, routinely used in laser cooling or atomic spectroscopy experiments. Moreover, thin metallic planar metamaterials have enhanced light transmission at the plasmon resonance. It thus becomes possible to perform reflection spectroscopy on a vapour/metamaterial interface. Previous experiment on Cesium vapor and plasmonic surface demonstrated a modification of the surface reflectivity [7], however, analysis of the Doppler broadened spectra did not provide quantitative information on the frequency shift or the atomic lifetime modification at the proximity of the metamaterials.

In this chapter, we report on high resolution frequency modulated selective reflection spectroscopy of Cesium $6^2P_{3/2}$ atoms in vicinity of a wide range of metallic planar metamaterials. First we present the experimental configuration and metamaterials design in Section 4.2. This is followed by a mean-field treatment of the metamaterial surface and developing the theoretical treatment of selective reflection in Section 4.3, allowing us to measure the dispersive non-retarded Casimir-Polder shift / van der Waals shift of the $6^2S_{1/2} - 6^2P_{3/2}$, Cesium D2 transition. For an adequately chosen metamaterial, the frequency shift on the Cesium transition, induced by the Casimir-Polder interaction, can be almost suppressed. A calculation of the non-retarded Casimir-Polder interaction is shown to reproduce the basic features of our experimental data. This is presented in Section 4.4.

4.2 Experimental Procedure

The system under investigation is depicted in Figure 4.1a. A vacuum chamber is maintained at base pressure of 10^{-8} mbar, A Cesium vapor at $T = 80°C$ is introduced into a vacuum chamber. The construction of the chamber is elaborated in Section 3.1 and the determination of the vapor temperature is elaboared in Section 3.7. The density of the atoms is around $N = 10^{17}\,\mathrm{m}^{-3}$ whereas the thermal velocity is $\bar{u} = 150\,\mathrm{ms}^{-1}$ measured from the optical transmission through the chamber that is explained in Section 3.7. Ten different metamaterials are engraved one quartz wedge window 3° (See Section 3.1.1 for wedge window design) of the vacuum chamber. The details

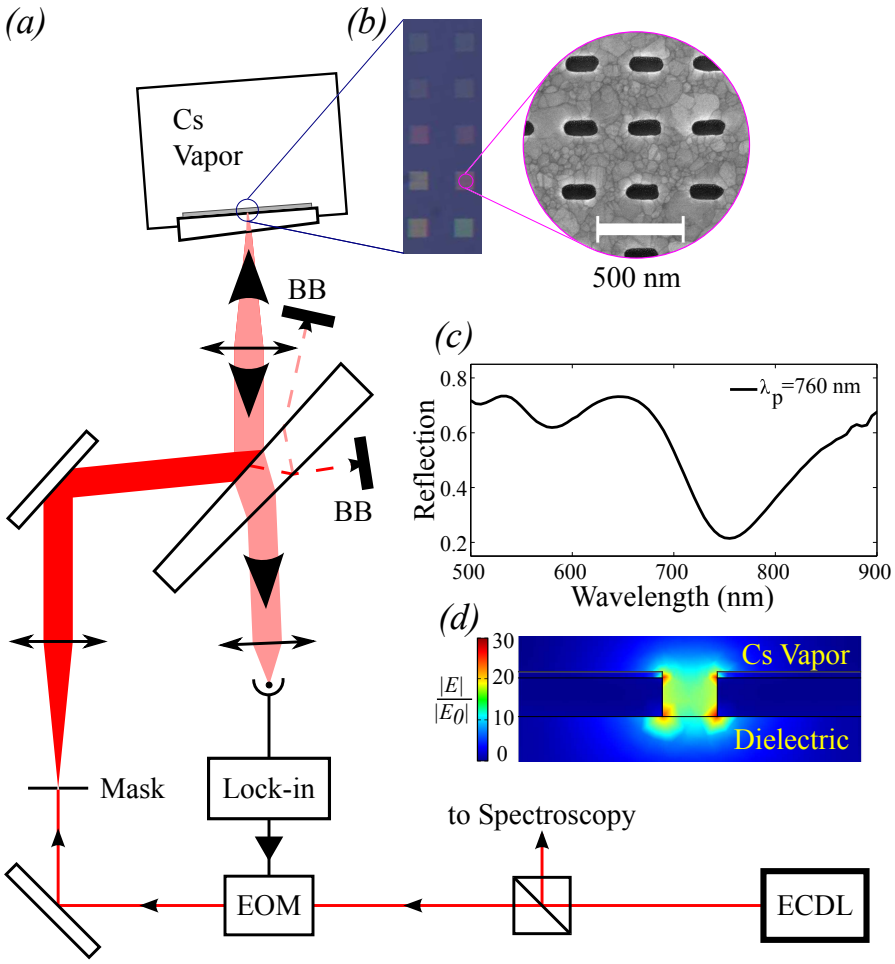

Figure 4.1: Schematic of the experimental set-up. (a) Experimental set-up. (b) Real color back-illuminated images of the ten metamaterials. The zoom corresponds to a scanning electron microscope image. (c) A typical reflectance curve of a metamaterial showing a main plasmon resonance at = 760nm. (d) Cut along one nanoslit. The false colors represent the electric field magnitude, normalized by the amplitude of the incident field, as obtained by finite-difference frequency domain simulation.

of fabrication and characterization are presented in Section 3.2. We achieve plasmonic resonances, characterized by their central position, covering a wavelength range from 670 nm to 980 nm. Each plasmon resonance has a typical width of 60 nm (see an example in Figure 4.1). The large linewidth of the plasmon resonance is due to the Ohmic losses from the absorption of the metal [76, 77]. The transmission and reflection of the metamaterials is measured and compared to FDFD simulations, see Section 3.2.3. The simulations match the experimental results apart from a global factor that arises from experimental losses. This illustrates the good agreement between the metamaterial simulation models and experiments. The comparison is done without the mean-field approximation that is done in later section to approximate the atomic vapor response. The atoms/metamaterial hybrid system is excited and probed on the $6^2S_{1/2} - 6^2P_{3/2}$ Cesium D2 transition at 852 nm, using a Selective Reflection (SR) optical setup at normal incidence.

The radiation is produced by an external cavity diode laser (ECDL). Part of the light is sent to a saturated absorption spectroscopy setup used as a frequency reference. The frequency reference is used to stabilize the laser drift, explained in Section 3.5. The main beam goes through an Electro-Optic Modulator (EOM) to modulate its phase at $\omega_m/2\pi = 9\,\mathrm{MHz}$ with a modulation index of $\beta = 0.19$ and is then shaped by a square mask (See Section 3.3) to optimize its overlap with the metamaterial. The intensity of the laser is maintained below saturation, typically $I = 1\,\mathrm{mW/cm^2}$. The light polarization is chosen to be perpendicular to the metamaterial slits to excite the plasmonic resonances. The reflected light beam is collected on a fast and sensitive amplified photodetector. The signal at 9 MHz is demodulated using a lock-in amplifier, directly providing the in-phase and in-quadrature component of the reflection signal, which is purely Doppler-free and analyzed in the following.

4.3 Selective reflection results and mean-field interpretation

We tune the laser onto the $F = 4 - F' = 5$ hyperfine transition scanning over a frequency range of $100\,\mathrm{MHz} = \sim 20\,\Gamma/2\pi$, where $\Gamma/2\pi = 5.2\,\mathrm{MHz}$, is the bare frequency width of the atomic transition. The demodulated signals at 9 MHz of the beam reflectance correspond to the red points on Figure 4.2.

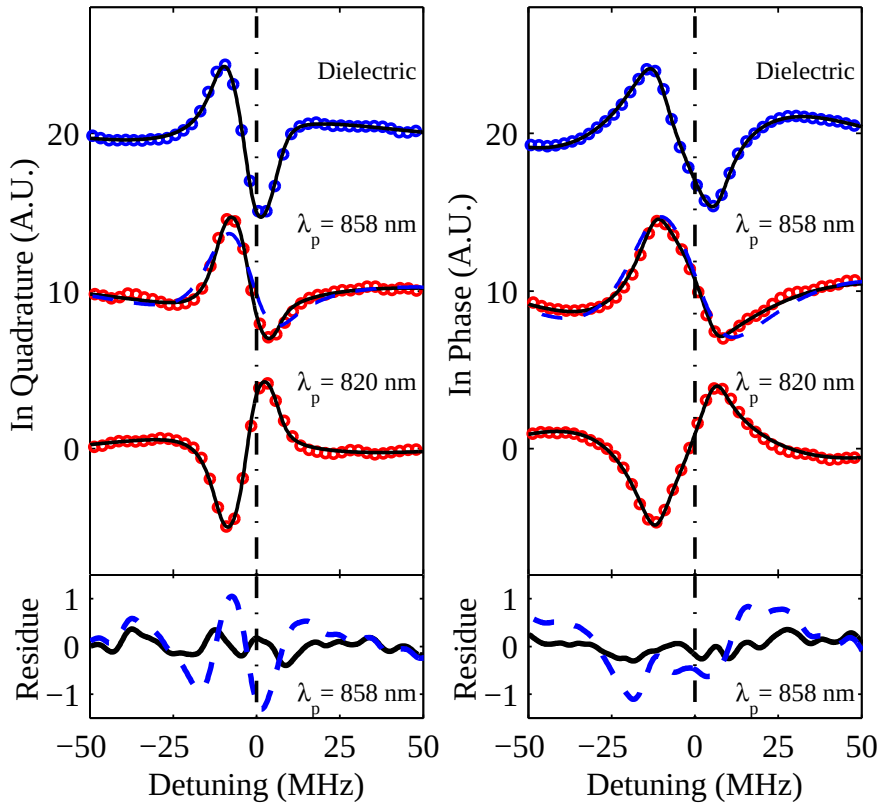

Figure 4.2: In phase and in quadrature selective reflection spectra of the plain windows (blue dots at top curves) and of two metamaterials (red dots). The black solid curves are the fits using Equation (4.2). The dashed blue line is a fit assuming $\mathrm{Im}[\Delta C_3] = 0$ for the metamaterial at $\lambda_p = 858\,\mathrm{nm}$. The residues correspond to the metamaterial at $\lambda_p = 858\,\mathrm{nm}$. The units are the same than for the main top curves.

We observe a strong modification of the Doppler-free spectrum due to the presence of the metamaterials with respect to a plain dielectric window (see blue points on Figure 4.2). The hyperfine structure of the D2 line is spectrally resolved with our selective reflection experiment, as the frequency spacing between hyperfine components (200 MHz between $\mathrm{F}' = 3$ and $\mathrm{F}' = 4$ and

250 MHz between $F' = 4$ and $F' = 5$) are much larger than the width of the observed spectra ($\sim 10 - 20$ MHz). Also, the plasmonic resonance is much broader than the hyperfine splitting therefore its effects are identical on all hyperfine components.

In order to understand the modification of the SR spectrum of Cesium $6^2P_{3/2}$ atoms in vicinity of the metamaterials, we recapitulate the theoretical framework from Chapter 2 in the next subsection. First we illustrate the stationary wave characteristics of the surface plasmon field in our two-dimensional metamaterial. Then we set forth the mean-field model we prescribed for modeling the metamaterial interface. Following that we explain the fitting procedures using the selective reflection theory. In the conclusion of this section, we present the fit that gives the complex van der Waals ΔC_3 coeffficients of Cesium $6^2S_{1/2} - 6^2P_{3/2}$ coupling with the metamaterial surfaces.

4.3.1 Surface plasmon waves

The general solutions of electromagnetic waves generated by a two-dimensional periodic nano-structured metamaterial can be decomposed into a propagating plane wave at normal incidence and surface plasmon waves. The schematic of the metamaterial with corresponding propagating wavevectors and surface plasmon wavevectors is illustrated in Figure 4.3(a). In the case of our two-dimensional metamaterial, FDFD results are shown on Figure 4.3(b). The evanescent surface plasmon waves are clearly observed if one removes the propagation component as it is shown in Figure 4.3(c).

Because of the underlying symmetry of the metamaterial, one gets

$$|E^{SP}_{+,m}| = |E^{SP}_{-,m}|. \tag{4.1}$$

$|E^{SP}_{+,m}|$ ($|E^{SP}_{-,m}|$) is the amplitude of the surface plasmon wave, with a real tangential wavevector $k^{SP}_{+,m} = 2\pi|m|/\Lambda$ ($k^{SP}_{-,m} = -2\pi|m|/\Lambda$). From Equation (4.1), we find that the surface plasmon waves are stationary waves. It also means that there is no static component corresponding to a null wavevector along the tangential plane. The absence of this static component tells us that plasmon waves do not contribute to the Doppler-free signal. Other components of the plasmon wave have a wavevector amplitude $2\pi|m|/\Lambda > |m|k_{in}$. Thus they give strongly Doppler broadened contribution, well smoothed by the relative slow response of the atomic coherence. This is also explained

in the theoretical background of SR spectra in Section 2.2.5 in terms of the contribution of tangential wavevector $k_x\hat{\boldsymbol{x}}, k_y\hat{\boldsymbol{y}}$ components to the effective susceptibilities $\bar{\chi}$.

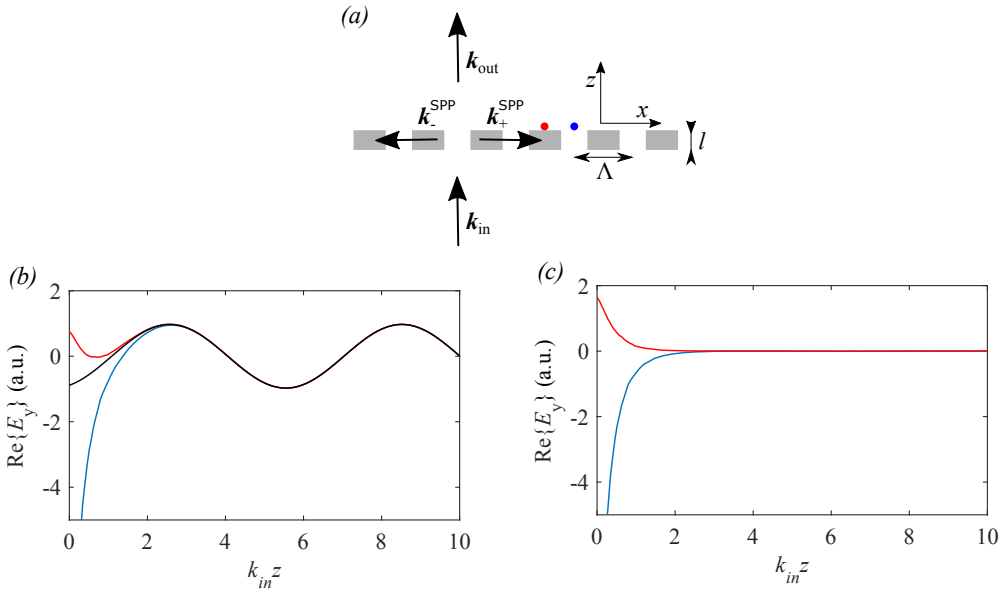

Figure 4.3: (a) Schematic of the metamaterial and the different wave vectors of the fields (b) Spatial evolution of the real part of the transmitted electric field along y, which corresponds to the incident polarization direction. We use here the finite-difference frequency domain numerical methods. $z = 0$ correspond to the outer interface of the metamaterial. The blue (red) curves correspond to the center (150 nm away for the center) of the nano-slit. The locations are indicated on (a) by a blue (red) dot. The black curve is a fit of the far-field response. It represents the propagating component of the transmitted field. It is also the transmitted field obtained using the mean-field approximation, i.e. replacing the metamaterial by a bulk material having the same far-field properties. (c) same as (b) but the propagating component has been removed. The remaining fields correspond to the surface plasmon wave localized in the vicinity of the metamaterial.

4.3.2 FDFD simulations and mean field approximation for the atomic vapour response

To analyze the selective reflection spectra, we modeled the metamaterial by a spatially homogeneous bulk material having the same thickness and the same far-field properties at normal incidence. We deduce, n', the complex index of refraction of the effective bulk material, a mean-field approximation known to well describe the far-field for transmitted and reflected fields at 852 nm [78, 79] (See Figure 4.3(b) for the transmission for one of the metamaterials. Reflection is not shown here). The complex indices of refraction extracted for all ten metamaterials are listed in Appendix A.1.

We note that the effective bulk material does not generate surface plasmon waves and the far-field propagating wave extends up to the material position, i.e. $z = 0$. Thus the near-field electromagnetic environments are very different for the metamaterial and the bulk material. Since the reflectance signal of the atomic vapor emerges from the response of the atoms in the vicinity of the metamaterial, the mean-field approximation can be questioned here. However, we find that it is a good approximation, because of the nature of the plasmon wave. We have mentioned in the previous section, indeed that the absence of null wavevector along the tangential plane implies that the local plasmon wave does contribute to the SR signal in a form of a weak and broad Doppler contribution. The contribution could not be observed in the experiment because of systematic errors on the offset of the signal. Finally we conclude that, other than modifying the index of refraction and $r * \rho$ (See Section 2.2.3 for explanation on $r * \rho$), the plasmon wave does not play other roles in our system.

4.3.3 Fitting with SR theory

In SR spectroscopy with a homogeneous material interface, the vapor can be characterized by an effective electric susceptibility, $\bar{\chi}$. Its frequency derivative is given, in the Doppler limit ($k\bar{u} \gg \Gamma/2\pi$), by (Refer to Section 2.2.5 for the derivation):

$$\frac{\mathrm{d}\bar{\chi}}{\mathrm{d}\omega} = \frac{i2Nk\mu^2}{\sqrt{\pi}\bar{u}\epsilon_0\hbar}\int_0^\infty\int_0^z dzdz'\mathrm{e}^{ik(z+z')}\frac{z-z'}{\mathcal{L}_0(\omega,z)-\mathcal{L}_0(\omega,z')}. \tag{4.2}$$

$\frac{\mathcal{L}_0(\omega,z)}{z} = \frac{\Gamma}{2} - i(\omega - \omega_0 - \frac{\Delta C_3 z^{-3}}{2})$ is the Lorentzian lineshape of the bare atomic resonance, corrected by the z^{-3} Casimir-Polder frequency shift in the non-

retarded regime. Here, ω_0 is the bare atomic resonance, k is the wavenumber of the laser beam and μ is the two-level atomic dipole moment. Spectroscopic experiments are sensitive to the energy difference between levels. We therefore denote ΔC_3 as the difference of van der Waals coefficients between lower and upper state. In our analysis, ΔC_3 is considered to be complex. As can be seen from the equations above, its real and imaginary parts denote a distance dependent shift and linewidth respectively. The metamaterial/vapor interface is located at $z = 0$. We note that the phase factor, $\mathrm{e}^{ik(z+z')}$ rapidly averages the effective susceptibility to zero for $z, z' \gg k^{-1}$. As an important consequence, only the atoms located in a layer of thickness k^{-1} contribute to the SR signal. Moreover, as it can be seen in Equation (4.2) and already discussed in Chapter 3, the signal is Doppler-free. We note as well that, since $\bar{\chi} \ll 1$, the index of refraction of the atomic vapor reads as $n_a = 1 + \bar{\chi}/2$. Under this approximation, the complex reflection coefficient of the electric field for the dielectric/metamaterial/vapor system can be linearized as:

$$r = r_0 + \rho\bar{\chi}(\omega) \tag{4.3}$$

where r_0 and ρ depend only on the indices of refraction of the metamaterial n' and of the dielectric substrate n_d (see Section 2.2.1). In the Doppler limit, $\bar{\chi}(\omega)$ is obtained by integration of Equation (4.3). In the weak modulation limit, i.e. $\beta \ll 1$ we find that the demodulated signal has the following expression for the in-phase signal (Refer to Section 2.2.4):

$$V_p(\omega) = V_0 Re\{r_0^*\rho[\bar{\chi}(\omega+\omega_m) - \bar{\chi}(\omega-\omega_m)]\} \tag{4.4}$$

and for the in-quadrature signal,

$$V_q(\omega) = V_0 Im\{r_0^*\rho[\bar{\chi}(\omega+\omega_m) + \bar{\chi}(\omega-\omega_m) - 2\bar{\chi}(\omega)]\} \tag{4.5}$$

V_0 is a factor of proportionality. Within the mean-field approximation, the complex factor $r_0^*\rho$ can be evaluated analytically, depending on the metamaterial refractive indices n', dielectric window substrate index n_d and the metamaterial thickness l (see Section 2.2.3 for the derivation) via

$$r_0^*\rho = \frac{4|r_0|^2 n_d n'^2 \mathrm{e}^{\frac{2in'\omega}{c}}}{(1+n')^2(n'^2-n_d^2) + 2(n_d^2+n'^2)(1-n'^2)\mathrm{e}^{\frac{2in'\omega}{c}} + (1-n')^2(n'^2-n_d^2)\mathrm{e}^{\frac{4in'\omega}{c}}} \tag{4.6}$$

where ω is the optical frequency, c is the speed of light. By mixing the real and imaginary part of the susceptibility, the factor $r_0^*\rho$ gives the main

contribution of the modification of the atomic resonance lineshape induced by the plasmon resonance observed in Figure 4.2. Also, the product of the susceptibility with complex value $r_0^*\rho$ in Equations (4.4) and (4.5) leads to Fano-like resonance of the atoms/metamaterial hybrid system, which is shown in the asymmetrical lineshapes in the appendix Figure A.1. This is also shown by Stern and co-authors using a Kretschman geometry [7]. In addition to the Fano-like resonance, the Casimir-Polder interaction induces an additional contribution on the SR signal that we are now aiming to reveal and discuss.

Using Equations (4.2) to (4.6), we perform a fit of the SR signals for the different metamaterials including the bare dielectric substrate. The fitting parameters are the atomic resonance linewidth Γ, the complex value ΔC_3 and a common V_0 value. The effective index of refraction of the metamaterial n', thus the factor $r_0^*\rho$ is extracted from the FDFD simulation [79, 78]. The results of the fitting procedure correspond to the black curves in Figure 4.2. The factor $r_0^*\rho$ values, fitted ΔC_3 values and curves for all ten sets of metamaterials are annotated in Appendix A.1. We observed an excellent agreement with the experimental data. The volume atomic resonance width (away from the surface) is found to be 10(3) MHz, i.e. slightly larger than the bare linewidth of 5.2 MHz. This increasing of the linewidth, encountered as well on the dielectric interface, has been also reported in similar studies [80]. It can be due to residual collisional broadening. Most importantly, an imaginary part for the ΔC_3 has to be considered. To illustrate this point, we perform another fit, setting $\mathrm{Im}[\Delta C_3] = 0$. Under this constraint, we observe that the convergence of the fitting procedure is not satisfactory (see residue comparison in Figure 4.2 for $\lambda_p = 858\,\mathrm{nm}$).

The complex van der Waals coefficients obtained from the fits are shown in Figure 4.4(a)-(b). Error bars are plotted as a range of values of F could have similar effect on ΔC_3 as discussed in Section 2.2.6. The real part of the ΔC_3 coefficient (Figure 4.4a), displays a dispersive type of resonant behavior centered at $\lambda_p =\sim 840\,\mathrm{nm}$. At the blue side of the resonance we observe a significant increase of the interaction, with respect to its off resonant value $\sim 5\,\mathrm{kHz}\,\mu\mathrm{m}^3$, followed by a sharp decrease that leads to a nearly vanishing value of the interaction at the resonance. At off-resonances at both sides, the ΔC_3 coefficient corresponds to the ΔC_3 coefficient of pure silver, confirming the validity of our data analysis. The resonance width is in agreement with the plasmon linewidth of 60 nm, confirming the plasmonic origin of the modification of the ΔC_3 values. The presence and evolution of the imaginary (dissipative) part for the van der Waals coefficients, shown in

Figure 4.4b, corresponds to a decreasing of the atomic lifetime associated with enhancement of the vacuum mode density at the plasmonic resonance. This enhanced emission rate can be also be understood as an increasing of the Purcell factor as observed for example with ultracold gas [12] or nano-antennas [81]. The enhanced radiation emission of the atom/metamaterial system can finally, either be coupled to electromagnetic propagating modes, or be lost due to Ohmic losses in the metal. The selective reflection technique does not distinguish between those two cases.

4.4 Control of surface force

We compare our experimental measurements, with the QED theory of atom-surface interactions. A complete analysis of the resonant Casimir-Polder interaction depends on knowledge of the dielectric properties of the metamaterial for both real and imaginary frequencies. For this purpose, we fit the dielectric constant $\epsilon(\omega)$, extracted by FDFD simulations, to the following function [58]:

$$\epsilon(\omega) = 1 - \frac{\omega_p^2}{\omega^2 + i\gamma_p\omega} + \sum_j \frac{f_j\omega_j^2}{(\omega_j^2 - \omega^2) - i\gamma_j\omega} \tag{4.7}$$

The first part of the equation is a Drude model that accounts for the plasma resonance of silver itself. The plasma frequency ω_p and dissipation γ_p are common values for silver [82] for all metamaterials. The second part models the metamaterial resonances. The amplitude f_j, frequency ω_j, and dissipation γ_j of each resonance are smoothly varying functions of the plasmonic resoannce λ_p of the metamaterial. By interpolating these parameters, we get the dielectric constant $\epsilon(\omega)$ for continuous range of metamaterials.

We then calculate the difference of the Casimir-Polder frequency shift between $6P_{3/2}$ and $6S_{1/2}$, which is the experimentally measured quantity in selective reflection spectroscopy. We take into account both non-resonant and resonant components of the atom-surface interaction, since our experiments are performed on excited state atoms. In the non-retarded regime, the ΔC_3 coefficient is decomposed into two components:

$$\Delta C_3 = \Delta C_3^{\{\mathrm{nr}\}} + \Delta C_3^{\{\mathrm{r}\}}. \tag{4.8}$$

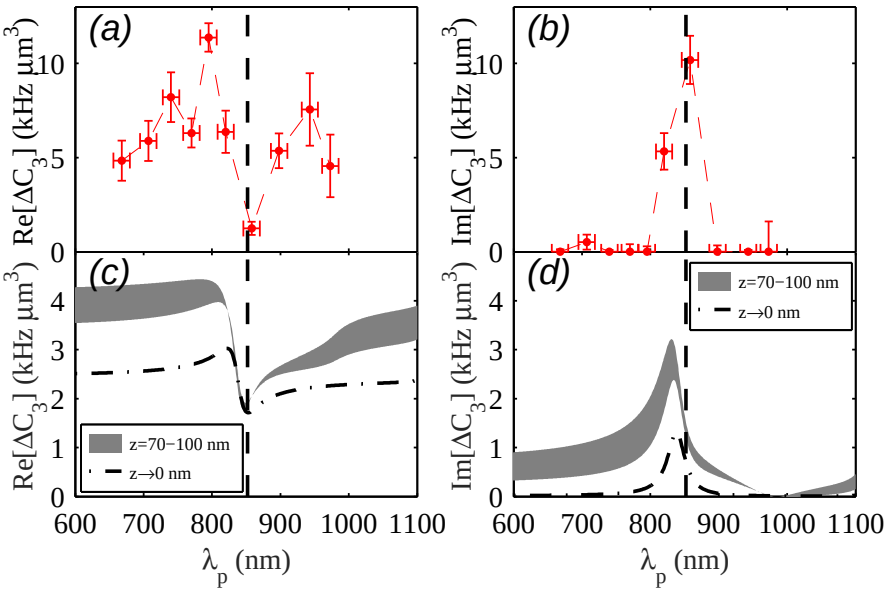

Figure 4.4: ΔC_3 coefficients as function of λ_p, the position of the plasmon resonance. Real part (a) and imaginary part (b) extracted from the fits of the selective reflection signals. Red horizontal (vertical) bar is the ΔC_3 (plasmonic resonance) uncertainty (c) and (d) are the real and imaginary parts of the ΔC_3 coefficients computed from the model. The dot-dashed curve corresponds the non-retarded case. The retarded contribution is taken into account by considering an effective distance ranging from 70 nm to 100 nm. It corresponds to the shaded grey surface. The vertical dashed lines indicate the position of the atomic resonance.

Here $\Delta C_3^{\{\mathrm{nr}\}}$ takes into account the dispersion contribution of virtual exchange of non-resonant vacuum photons, whereas $\Delta C_3^{\{\mathrm{r}\}}$ gives the contribution due to resonant photon exchange between an excited atom and the metamaterial. The $\Delta C_3^{\{\mathrm{nr}\}}$ is practically independent of the plasmonic resonance position and is mostly governed by the metallic response over the

entire frequency spectrum. $\Delta C_3^{\{\mathrm{nr}\}}$ is given by [83, 84]:

$$\Delta C_3^{\{\mathrm{nr}\}} = \frac{\sum_j \mu_j^2}{48\pi\epsilon_0} r(\omega_j > 0) \tag{4.9}$$

where the function is a summation over all possible excited states j connected by electric dipole transition from the ground state $6S_{1/2}$ and μ_j denotes the reduced dipole moment of the coupling of the ground state to excited state j. The behavior of $\Delta C_3^{\{\mathrm{nr}\}}$ over the frequency spectrum is characterized by the image coefficient $r(\omega_j > 0)$ which is defined as:

$$r(\omega_j > 0) = \frac{2}{\pi} \int_0^\infty S(\mathrm{i}u) \frac{\omega_j}{\omega_j^2 + u^2} \mathrm{d}u \tag{4.10}$$

in which $\omega_j > 0$ is positive frequency (by convention) for virtual absorptions from the ground state to state j and $S(\mathrm{i}u)$ is the surface response taken at the imaginary frequency $\mathrm{i}u$:

$$S(\mathrm{i}u) = \frac{\epsilon(\mathrm{i}u) - 1}{\epsilon(\mathrm{i}u) + 1} \tag{4.11}$$

where $\epsilon(\mathrm{i}u)$ is the dielectric constant over imaginary frequency. In Figure 4.5, we show $r(\omega_j > 0)$ as defined in Equation (4.10) for one of the metamaterials with a plasmonic resonance at 835 nm that we extract from FDFD simulation.

The influence of the plasmon resonance is contained in the resonant contribution since it concerns only the resonant photons emitted on the $6P_{3/2} \rightarrow 6S_{1/2}$ cesium D2 transition at 852 nm [58, 84], and it is mainly at the origin of the observed Casimir-Polder resonant behavior. Following reference [84], we predict:

$$\Delta C_3^{\{\mathrm{r}\}} = \frac{\mu_r^2}{48\pi\epsilon_0} 2S(\omega_r) \tag{4.12}$$

where μ_r is the reduced dipole moment of the $6P_{3/2} \rightarrow 6S_{1/2}$ coupling and $S(\omega < 0) = (\epsilon(\omega) - 1)/(\epsilon(\omega) + 1)$ is the surface response over real frequency. Following the convention defined above, emission is denoted with negative frequency, $\omega < 0$. $S(\omega < 0)$ defines the characteristic behavior of $\Delta C_3^{\{\mathrm{r}\}}$ over the frequency spectrum and the real part and imaginary part of the $S(\omega < 0)$ contributes to the real and imaginary part of the $\Delta C_3^{\{\mathrm{r}\}}$ respectively.

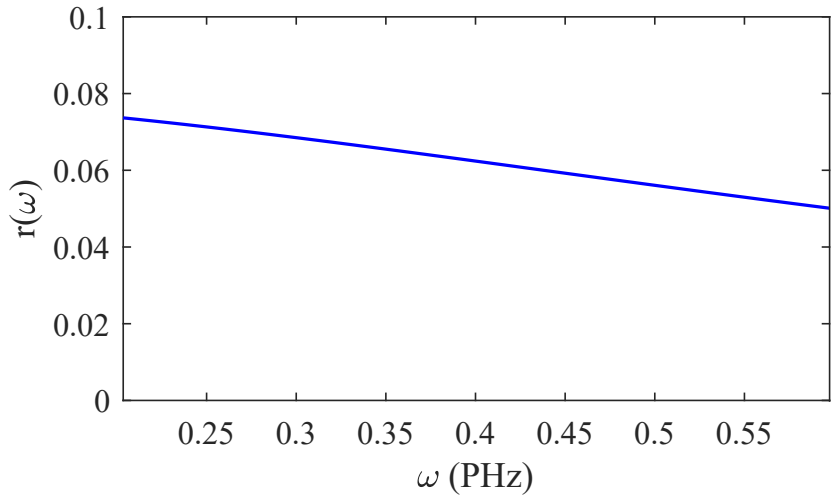

Figure 4.5: $r(\omega_j > 0)$ for our finite-difference frequency-domain method simulated metamaterial with plasmonic resonance at 835 nm. We observe the characteristic monotonic decreasing function of $r(\omega_j > 0)$ of non-resonant component of the atom-surface interaction [58].

Figure 4.6 shows the $S(\omega < 0)$ behavior of one of our metamaterial from the ϵ extracted from the FDFD simulation.

The results of this model are shown in Figure 4.7. We see an excellent agreement confirming that the resonance behavior of the Casimir-Polder interaction is due to the resonant photon exchange between an excited atom and the metamaterial.

The results of the non-retarded model are shown as dashed lines in Figure 4.4(c)-(d). The theoretical predictions exhibit a resonant behavior similar to the experimental findings, showing that our model captures the essence of the physical mechanism behind the tuning of the atom-surface interaction. However, the amplitude of the resonance is smaller than the experimentally measured one. The smaller amplitude of the ΔC_3 coefficients of the theoretical predictions could be partly explained by the van der Waals potential used. Athanasios Laliotis, our co-author for this work tackled the problem by modeling the potential with a retarded Casimir Polder potential which gives larger ΔC_3 coefficients which are closer to experimental data values. This is illustrated as shaded grey surface in Figure 4.4c-d. The details are presented in our publication. Another possible deviation between the

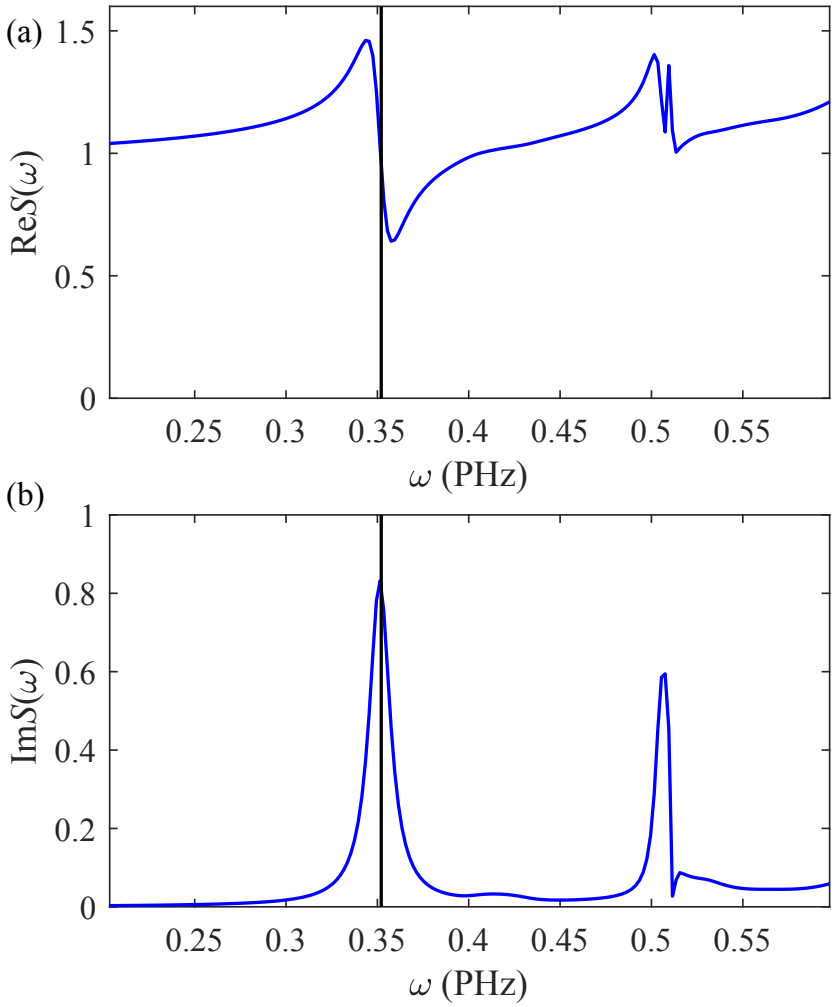

Figure 4.6: $S(\omega < 0)$ for our finite-difference frequency-domain simulated metamaterial with plasmonic resonance at 835 nm. (a) The real part. (b) The imaginary part. Vertical black line marks the frequency for the $6P_{3/2} \rightarrow 6S_{1/2}$ atomic transition at 852 nm.

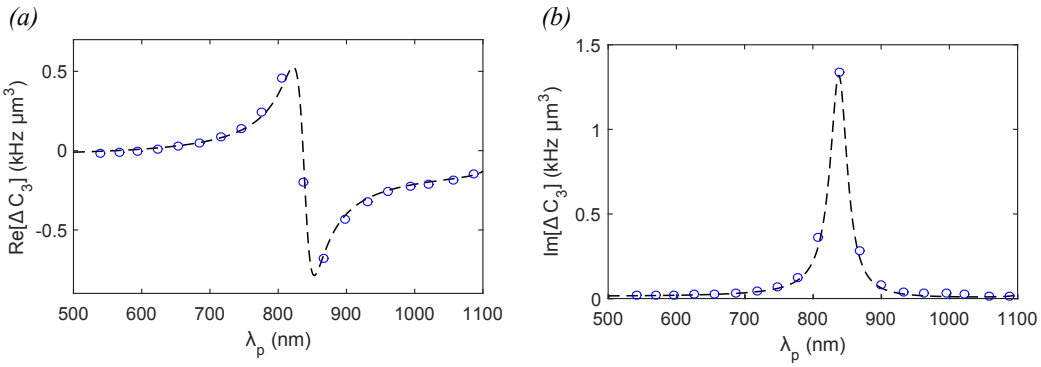

Figure 4.7: Comparison between the resonant photon exchange model (blue circle) and the completed model (black dashed line) of the Casimir-Polder interaction. The plots are as function of the plasmon resonance frequency. The resonant photon exchange model corresponds to Equation (4.12). (a) Real part of the ΔC_3 coefficient, where the background contribution has been removed. (b) Imaginary part of the ΔC_3 coefficient.

theoretical and experimental coefficients comes from the anisotropic behavior of the metamaterial. This could be addressed by expanding the anisotropic theoretical framework by Gorza et al. to include the retardation effect [85].

4.5 Conclusion

We use planar metamaterials as a testbed to control the Casimir-Polder frequency shift of the D2 line of Cs atoms. Our theoretical analysis, based on the mean field approximation (See Section 4.3), reproduces the main characteristics of the Casimir-Polder resonance albeit with a smaller amplitude. When the plasmon resonance almost coincides with the atomic resonance, the Casimir-Polder frequency shift nearly vanishes. Across the different metamaterials, the Casimir-Polder interaction is characterized by the usual real coefficient leading to a dispersive resonance, as well as a non-zero on-resonance dissipative response (Refer to Section 4.4).

This chapter is an adaptation from Science Advances **4**:eaao4223 by Chan *et al.*, and is used under a CC BY-NC 4.0 license. Exclusive licensee - American Association for the Advancement of Science. Additions and modifications of original text are listed below:

1. Addition of introductory sentences to the last paragraph of Section 4.1.
2. Addition of explanatory sentences to Section 4.2.
3. Relocation of descriptions on metamaterials fabrication in Section 4.2 to Section 3.2.
4. Addition of a second paragraph to the introduction of Section 4.3.
5. Relocation and modification of last three sentences from Section 4.3.2 to the end of Section 4.3.1.
6. Addition of the text *"...for transmitted and reflected fields at* $852\,\mathrm{nm}$*", "for one of the metamaterials" and "The complex indices of refraction extracted are listed in Appendix A.1"* to the first paragraph of Section 4.3.2.
7. Relocation and modification of the sentence *"We have mentioned...not contribute to the SR signal."* from Section 4.3.1 to Section 4.3.2.
8. Addition of text *"where* ω *is the optical frequency,* c *is the speed of light."* to the first paragraph of Section 4.3.3.
9. Addition of the text *"At off-resonances at both sides, the* ΔC_3 *coefficient corresponds to the* ΔC_3 *coefficient of pure silver,..."* to the third paragraph of Section 4.3.3.

10. Addition of new paragraphs and two new figures to Section 4.4.
11. Addition of last five sentence at the end of Section 4.5.

Chapter 5

Metamaterial on fiber tip

5.1 Introduction

With the recent development of nanofabrication on fiber technique, it is now possible to engineer the fiber tip surface with nanostructures. In particular, tailoring strong confinement of light with nanostructures have been used for surface enhanced Raman scattering where in-situ sensing of biological molecules is enhanced [86, 87, 88]. Nonetheless, investigation of hot atoms at the vicinity of a plasmonic surface of a fiber tip has not yet been demonstrated. We establish in Chapter 4 that plasmono-atom system is suited to investigate and alter surface-atom coupling . In this chapter, we present the first experimental demonstration of modification of Doppler-free selective reflection signal on hot atomic vapor with metamaterial on a fiber tip. The methods for experiment are summarized in Section 5.2. In Section 5.3, we fit the reflection lineshapes using the selective reflection theory developed in Section 2.2. In the same section, the optical saturation parameters and transit time broadening on our system are also investigated.

5.2 Experimental setup

A schematic of the experimental setup is shown in Figure 5.1. The Cesium $6^2S_{1/2} \rightarrow 6^2P_{3/2}$ transition at the tip of multimode fibers is probed using a frequency modulated selective reflection (SR) optical setup. Two optical fibers are prepared, the first with a cleaved bare dielectric tip and another with ring-shaped metamaterial fabricated on the cleaved tip. The design and

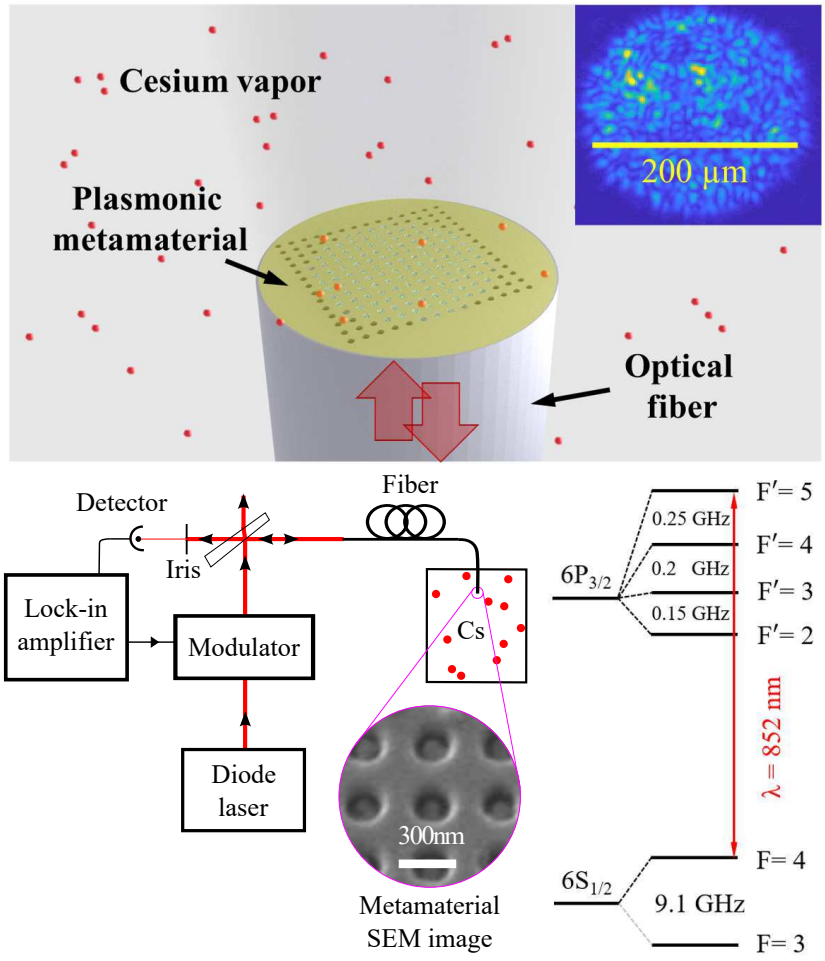

Figure 5.1: (Top) Artistic view of selective-reflection spectroscopy at the fiber tip. The red spheres surrounding the fiber tip surface represent the atoms of the thermal vapor, coupled with the plasmonic field of the metamaterial. (Inset) Speckle pattern on the fiber tip. (Bottom left) Experimental setup used to investigate the plasmono-atom coupling on the tip of the fiber. A phase modulated optical excitation is coupled into the metamaterial fiber tip that is submerged in a vacuum chamber containing Cesium vapor (Cs). The plasmono-atomic interactions on fiber tip is measured by demodulating the reflection signal with a lock-in amplifier. Scanning electron microscope image of the rings metamaterial. (Bottom right) The energy level of the Cesium D2 transition of interest (not on scale). The laser is scanned across the $6^2S_{1/2}(F = 4) \rightarrow 6^2P_{3/2}(F' = 4 - 5)$ transitions.

characterization of the metamaterial on fiber tip is presented in Section 3.2. The metamaterial has a plasmonic resonance at $\lambda = 830\,\text{nm}$ or 361 THz and a linewidth of 100 nm or 40 THz (See Figure 5.3(a) for the reflection spectrum), which is slightly blue detuned with respect to the Cesium $6^2S_{1/2} - 6^2P_{3/2}$ D2 line. Optical beam from a tunable semiconductor diode laser is phase modulated at 9 MHz with a modulation index of 0.12, and coupled into the fibers with an Olympus MPlan 10× microscope condenser. Using a vacuum sealed with a Teflon feedthrough (See Section 3.1.2 for the fiber sealed design), the fiber is inserted inside a saturated pressure Cesium vapor chamber at a temperature of 50 °C, which corresponds to an atomic density of $5 \times 10^{11}\,\text{cm}^{-3}$. The atomic density is determined using the method expounded in Section 3.7. In absence of Cesium, an ultrahigh vacuum of $< 10^{-8}$ mbar is achieved with this sealing method. The fiberized connector tip is kept at a slightly higher temperature than the rest of the chamber to prevent condensation of Cesium at the fiber tip. Two reflection spots are present on the reflection of the optical fiber, one from the input surface and another from the metamaterial-atoms interface. The latter reflection is filtered with an iris, and focused on an amplified photodetector. The detected signal is then demodulated with a lock-in amplifier. Frequency reference of the laser given by a hole burning saturated absorption frequency spectroscopy done in a bulk vapor Cesium cell (not shown in the figure) is used to compensate for the laser frequency drift. The frequency stabilization method is explained in Section 3.5.

5.3 Results and Interpretation

The selective reflection spectroscopy allows us to selectively couple the electromagnetic field with atoms moving parallel to the surface within a layer of $k^{-1} = 135\,\text{nm}$. The signal is Doppler-free (bare linewidth: $\Gamma = 2\pi \cdot 5.2\,\text{MHz}$) which resolves the Cesium hyperfine structure of the $6^2P_{3/2}$ excited level [42]. The demodulated signal shows differences of the hyperfine spectra with plasmonic metamaterial on the tip of fiber compared to the bare fiber, see Figure 5.2. When the surface plasmon resonance coincide with the atomic resonance a π phase flip of the selective reflection spectrum is observed. In a mean-field approximation picture, where the metamaterial is replaced by a bulk material, these differences in the spectra with and without the metamaterial, can be also interpreted as the modification of the reflected light due to the etalon effect in the bulk material as discussed in Chapter 4 for

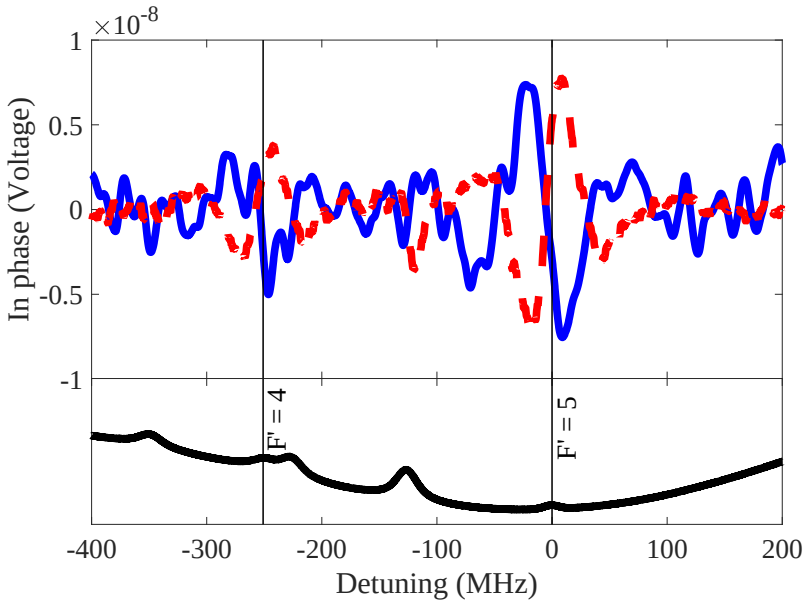

Figure 5.2: The in-phase component of the reflectivity signal measured at the frequency of phase modulation of incident laser as a function of laser wavelengths for the bare fiber (dashed red curve) and the fiber with plasmonic metamaterial structure at the tip (solid blue curve). The in-quadrature component is omitted from the plot for clarity purpose. We take into account the optical propagation phase in this spectrum. The solid black line is a frequency reference obtained by hole-burning saturation spectroscopy on a reference Cesium cell.

metamaterials deposited on a dielectric surface.

Apart from the etalon effect in the metamaterial, the coupling between the atomic resonance and plasmonic resonance modify the van der Waals energy shift in the excited state. We perform a selective reflection spectra fit on the largest hyperfine transition following the same treatment with Section 4.3.3. The fitting parameters are the spectra linewidth Γ, van der Waals coefficient ΔC_3, and the voltage amplitude V_0. We fit the spectrum of metamaterial interface with complex coefficients to account the dissipative losses from the coupling between plasmonic and atomic resonances. The fit are shown as dashed lines in Figure 5.3. The van der Waals coefficients obtained from the fit are $3(2)\,\mathrm{kHz}\,\mu\mathrm{m}^3$ for the bare fiber and $6(6) + \mathrm{i}5(7)\,\mathrm{kHz}\,\mu\mathrm{m}^3$ for fiber with metamaterials. Similar van der Waals coefficients with metamaterials on dielectric surface are found in Chapter 4.

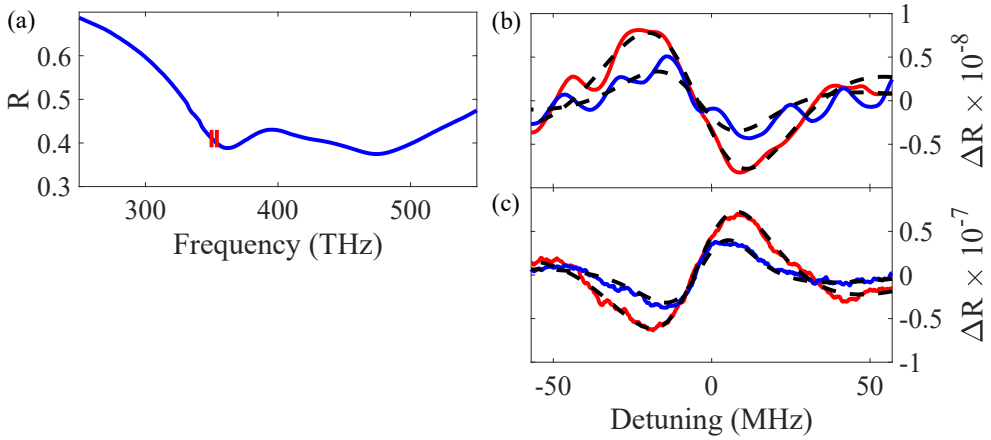

Figure 5.3: (a) Reflection spectrum of the plasmonic metamaterial structure at the fiber tip (Top left). Plasmonic metamaterial lineshape is shown in the broad frequency scan (blue). Cesium D2 atomic resonance line is indicated on the graph (Red bars).(b,c) The in-phase (red) and in-quadrature (blue) components of the reflectivity signal measured at the frequency of phase modulation of incident laser as a function of laser frequency for fiber with (b) metamaterial and (c) bare fiber for $\mathrm{F} = 4 - \mathrm{F}' = 5$ hyperfine transition. The theoretical fit including the Casimir-Polder interaction ΔC_3 is plotted in black.

The spectra measured on both bare fiber and fiber with metamaterial (Figure 5.2) have similar linewidth of about 45 MHz. The linewidth of

the signals is larger than the linewidth of 10 MHz that we measured on metamaterial on dielectric surface in Chapter 4 and is mainly attributed to the transit time broadening of atoms flying across the light intensity distribution patterns (See inset of Figure 5.1) at the fiber tip surface. This pattern results from the large transverse size of the fiber that allows the propagation of many high order transverse modes. Further discussion on the transit time characterization is presented in the next subsection.

5.3.1 Transit time broadening and intensity saturation effect

Starting from the image of the intensity distribution at the fiber tip, we compute the one-dimensional (1D) autocorrelation function,

$$C(\mu) = \langle \Delta I(x) \Delta I(x+\mu) \rangle / \langle \Delta I(x)^2 \rangle, \tag{5.1}$$

along two orthogonal direction, see Figure 5.4. $\Delta I = I - \langle I \rangle$, where $I(x)$ is the light intensity spatial distribution. $\langle . \rangle$ denotes the transversal averaging of the correlation function. We note that the autocorrelation function has a short correlation range as for a speckle pattern, and we will consider the intensity distribution as such in follow. The speckle grain size is then given by the 1/e width of the autocorrelation function [89], which turns out to be $\Delta\mu = 4.4\,\mu\text{m}$ in both orthogonal directions. This corresponds to a transit time broadening of $\bar{v}/\Delta\mu = 32\,\text{MHz}$ for atoms with thermal velocity of $\bar{v} = 140\,\text{m/s}$ which is the dominant broadening contribution to the 45 MHz linewidth in our experiment data. Other source of broadening such as atom-atom collision has been reported in similar studies and might also play a role in our experiment [80, 90, 1].

We further characterize the laser intensity impact on the spectroscopy signal. The amplitude of signal versus the incident power is plotted in Figure 5.5(a). We see a linear dependence of the amplitude of the signal on the incident power. In Figure 5.5(b), the signal is fitted with selective reflection lineshape to extract the linewidth of the signal. The fitting procedures we used are explained in Section 4.3.3. Even if the light intensity is above the saturation intensity ($I_s \leq I \leq 6I_s$, where $I_s = 2.7\,\text{mWcm}^2$ is the saturation intensity in bulk atomic vapor), we do not observe clear evidence of saturation once the laser intensity varies. We believe that this lack of saturation is due to the short transit time which increases substantially the effective saturation intensity by a factor of $2\pi\bar{v}/\Gamma\Delta\mu \simeq 6$;.

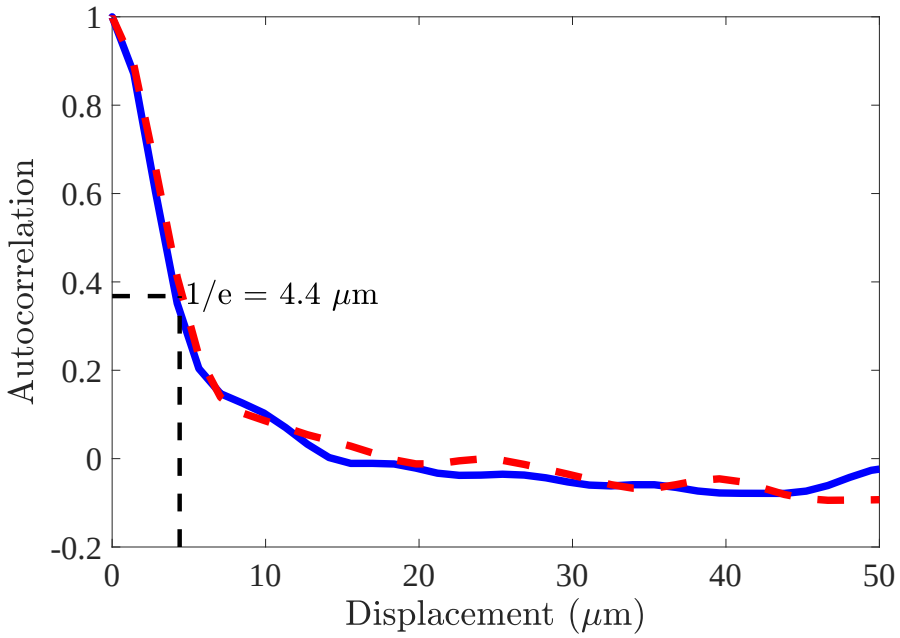

Figure 5.4: Autocorrelation function of the intensity distributions in x, y direction parallel to the fiber tip (dashed red and solid blue lines respectively) to determine the characteristic size of the hotspot in the speckle pattern. Black dashed line pinpoint the 1/e width of the speckle pattern.

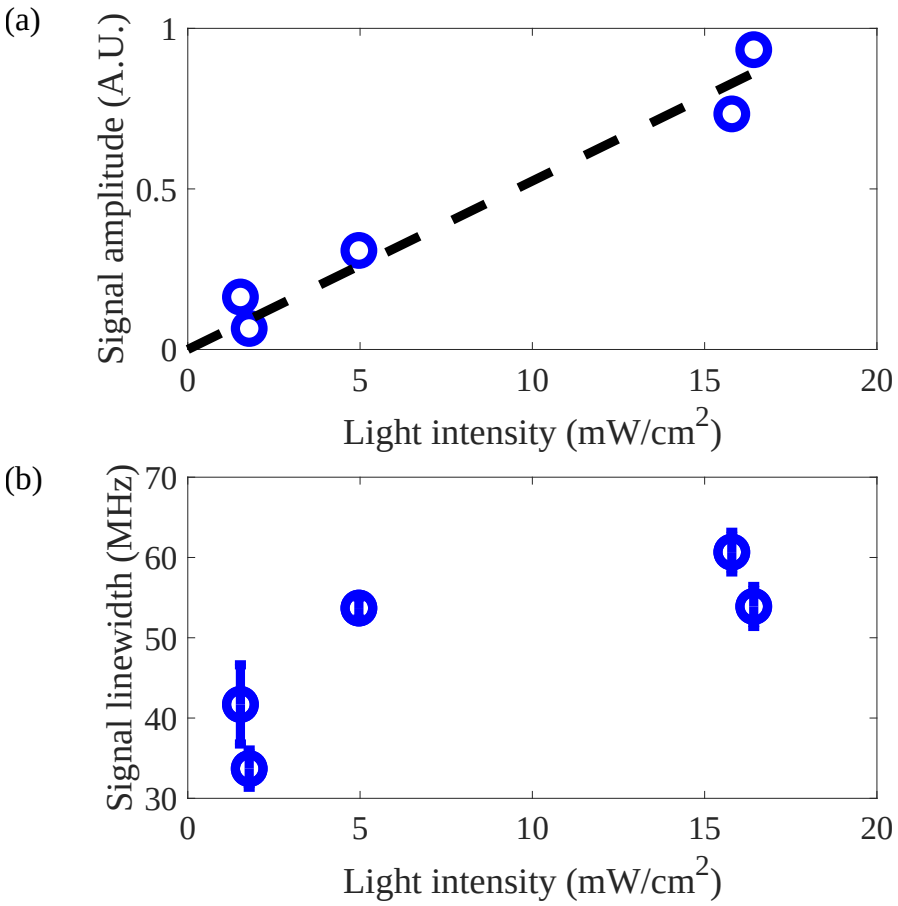

Figure 5.5: (a)Amplitude of signal of Cesium in plasmonic landscape at the fiber tip versus input intensity. (b)Linewidth of signal of Cesium in plasmonic landscape at the fiber tip versus input intensity. Error bars denotes the errors on the fit of the lineshapes to power saturation equation.

5.3.2 Propagating mode in bare fiber

On the reflection signal of the fiber with bare tip, we observe a signal at -125 MHz away from the $F = 4 \rightarrow F' = 5$ transition, which does not correspond to a Cesium hyperfine transition but it is in coincidence with the crossover $F = 4 \rightarrow F' = 4, 5$ (See Figure 5.2). This crossover is due to a velocity class which has a Doppler frequency shift in half way from the two lines such that one beam is at resonance with one transition and the contra-propagating beam is at resonance with the other transition. Reflection on the fiber tip is at normal incidence within angle of 12°corresponding to the acceptance angle of the fiber. This configuration rules out crossover signal since the atom with a normal velocity of $125\,\text{MHz} \times 852\ \text{nm} \approx 106\,\text{m/s}$ will leave the k^{-1}-thickness sensitive layer in a time much shorter than Γ^{-1} such that the interaction will not have time to take place, and the signal goes to zero. Thus, we interpret the presence of the signal at -125 MHz away from the $F = 4 \rightarrow F' = 5$, has a contribution of sidewall of the fiber. Indeed, since the cladding is thin (10 µm thick), the guided modes of fiber have non-zero evanescent field contribution outside the fiber cladding. The evanescent field interacts with the atomic vapor along the entire length of the optical fiber, which contributes to a non-negligible hole burning effect on the forward propagating and reflected lights. To get a better insight of the importance of the evanescent field in the atomic vapor, the propagation of light in the fiber is simulated by solving Helmholtz equation in the fiber including the cladding thickness. The solutions are eigenfunctions corresponding to Bessel functions of the first and second kinds. As an illustrative example, Figure 5.6 displays an in-phase summation of electric fields for all the propagating modes supported by the optical fiber. It shows a weak but non-zero evanescent field outside the fiber. After integration over the length of the fiber, and albeit small in magnitude, the evanescent field contributes to the spectrum and a clear signature is the presence of crossover-signal on bare fibers. The spectra are nevertheless dominated by selective reflection signals on the surface tip, as evidenced by the much larger signal at real transition of $F = 4 \rightarrow F' = 5$ compared to the crossover $F = 4 \rightarrow F' = 4, 5$ on the SR signal whereas in a hole burning setup, the crossovers have larger amplitudes than the real transition, as shown in the black curve in Figure 5.2. Ultimately, this contribution is suppressed by coating the optical fiber's sidewalls with a 5 nm thick of silver case for the fiber tip with metamaterials.

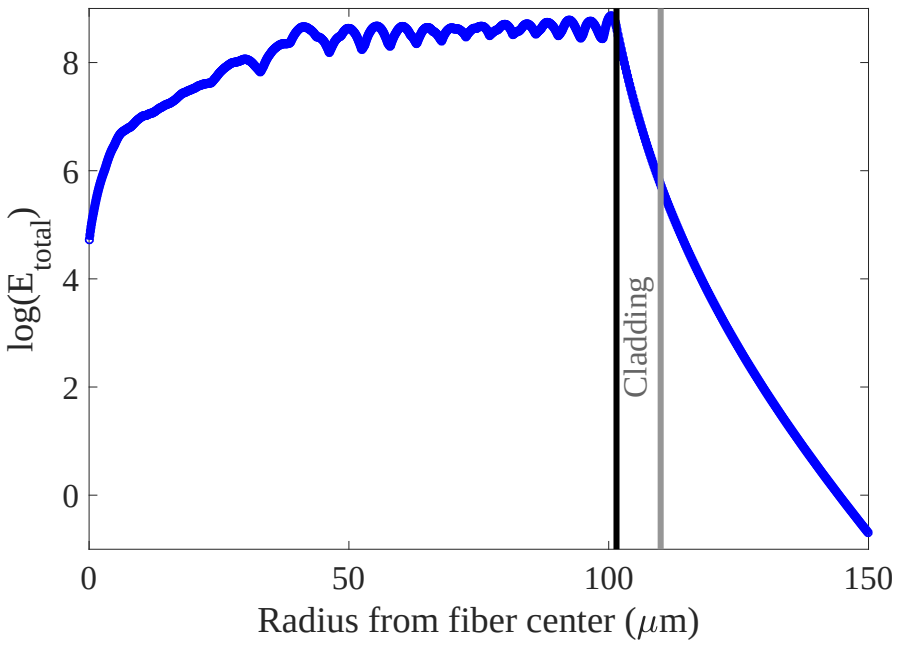

Figure 5.6: Coherent summation of guided optical modes for light at a wavelength of 852 nm in the multimode optical fiber. Non-zero evanescent mode outside the fiber cladding contributes to the spectrum on the bare fiber and in particular to the crossover signal shown in Figure 5.2.

5.4 Conclusion

We have demonstrated Doppler-free selective reflection spectroscopy of an atomic vapor coupled to a surface plasmon field at the tip of a multimode optical fiber. This paves the way for fiber-integrated surface engineering of hybrid atoms-metamaterial devices. We used an axial symmetric nano-patterning which leads to a polarization-independent plasmonic excitation. Polarization dependence on our symmetric plasmonic field can be restored if the atomic vapor becomes optically active by applying a magnetic field. In this case, extra tuning of the atom-plasmon Fano resonance can be implemented [8]. The large transverse size of the fiber allows the propagation of large order transversal modes. As a result, the field intensity distribution at the output of the fiber tip has a disordered structure similar to a speckle pattern. The transport of matter wave in such disordered optical potential has recently attract a lot of attention both for non-interacting system leading to Anderson localization [91, 92, 93], and for interacting atoms exploring thermalization in presence of many-body interactions [94]. Similar studies on the multimode fiber speckle patterns could be done, at which it would be interesting to add a surface plasmon field to gain larger amplitude and shorter length scale of the electromagnetic field. Recently, utilizing the dipole-dipole interactions of cold atoms at the nearfield of a fiber nanotip to realize a new single emitter source that has a narrow spectrum has been theoretically demonstrated [95]. It could also be desirable to tailor the fiber nanotip nearfields with nanostructures to favour the single photon emission.

Chapter 6

Doppler-free non-linear spectroscopy on an electric quadrupole transition

6.1 Introduction

With the appearance of laser sources, nonlinear Doppler-free Laser Spectroscopy (DFLS) has undergone a very fast development. It has been utilized for atomic and molecular spectral analyses, collisional studies in the vapor phase and investigation of fundamental processes [96, 97]. Up to now, in atomic physics, DFLS has been mainly performed by using laser sources resonant for electric dipole transitions. Dipole-forbidden transitions, particularly electric quadrupole transitions, are important in new avenues of atomic physics for fundamental studies like parity violation [98] or devising of ultra-high-accuracy optical clocks [99, 100, 101]. Spectroscopic studies of electric quadrupole transitions in vapors are generally hindered by Doppler broadening, and in most cases averaged over the internal structure of the electric quadrupole transition (e.g. hyperfine multiplets) [102, 103]. A noteworthy exception is the early work by Weber and Sansonetti [104] who performed resonantly enhanced stepwise excitation to high lying states of Cesium, using the $5D_{3/2}$ level as the intermediates state. In this way, they have been able to get Doppler-free spectra and resolve the hyperfine lines of the $6^2S_{1/2} - 5^2D_{3/2}$ electric quadrupole transition. Recent studies include Doppler-free 5p-6p transitions in Rubidium [105] and magnetic-field-mixing of forbidden hyper-

fine transitions of Cs D2 line [106]. Another well-explored approach to study the internal structure of highly-excited D levels of alkalis and measure their energy makes use of Doppler-free two-photon spectroscopy [107, 108].

In this chapter, we analyze Doppler-free hyperfine spectral lines of the Cs $6S_{1/2} - 5D_{5/2}$ electric quadrupole transition, as observed via three-level V-type nonlinear spectroscopy [109, 110, 111] on the $6P - 6S - 5D$ coupled system. We investigate the polarization properties and optical pumping processes responsible for the electric quadrupole spectral line intensities, and demonstrate the important role played by transit time on interpretating our spectra. In Section 6.2, we explain the Cs energy levels of interest, followed by the optical setup, paying attention on the saturation intensities of the pump and probe beams. We also explain the procedure for obtaining the frequency scale for our electric quadrupole spectral line from the fluorescent spectra of the electric quadrupole transition. In Section 6.3, we explain the structures in our Doppler-free spectra for two of our polarization - independent spectra. Subsequently, we calculate the signal strengths for the line intensities in Section 6.3.1. Lastly, we discuss a polarization - dependent spectrum in Section 6.4.

6.2 Experimental setup

To investigate Doppler-free spectroscopic characteristics on an electric quadrupole transition, we address the $6^2S_{1/2} \rightarrow 6^2D_{5/2}$ transition of Cesium at $\lambda = 685\,\text{nm}$ (Figure 6.1). This electric quadrupole line has a transition rate of $\gamma_{5D-6S} = 2\pi \cdot 3.5\,\text{Hz}$, with a total decay time of the excited state dominated by the the $5^2D_{5/2} \rightarrow 6^2P_{3/2}$ electric dipole line at $3.5\,\mu\text{m}$ of $2\pi \cdot 124\,\text{kHz}$ [103]. To monitor Doppler-free lines at 685 nm, we have adopted a pump-probe three-level spectroscopy approach [109, 110] in which population changes induced in the $6^2S_{1/2}$ ground state by a 685 nm laser are monitored on the $6^2S_{1/2} \rightarrow 6^2P_{3/2}$ line transmission at $\lambda = 852\,\text{nm}$ (Figure 6.1). The radiative linewidth of the 852 nm transition is $\gamma_{6P-6S} = 2\pi \cdot 5.2\,\text{MHz}$.

The schematic of the experiment setup is depicted in Figure 6.2. The 852 nm External Cavity Diode Laser (ECDL) is frequency locked onto one of the hyperfine transition of the $6^2S_{1/2} \rightarrow 6^2P_{3/2}$ line, using a saturated absorption side-experiment performed on an auxiliary room-temperature Cesium Vapor cell (cell 1 of Figure 6.2). The locking technique is explained in Section 3.6. We also address the 685 nm transition using an ECDL. The

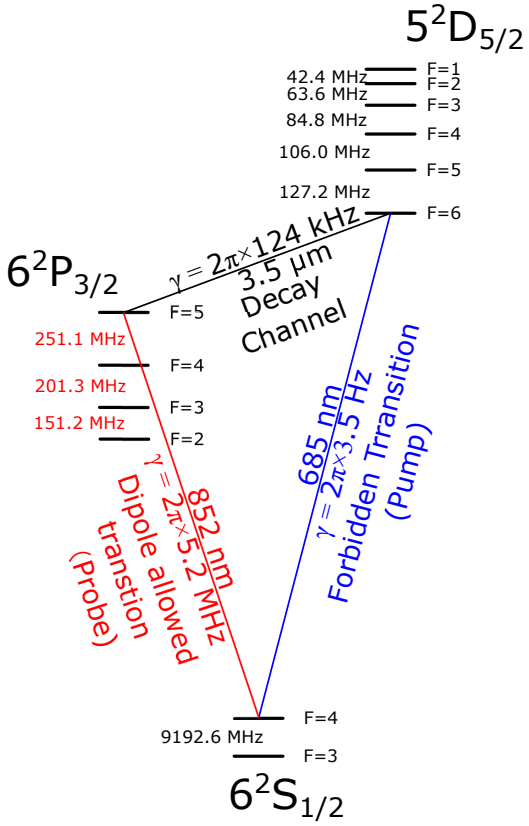

Figure 6.1: Cesium energy levels and transitions of interest.

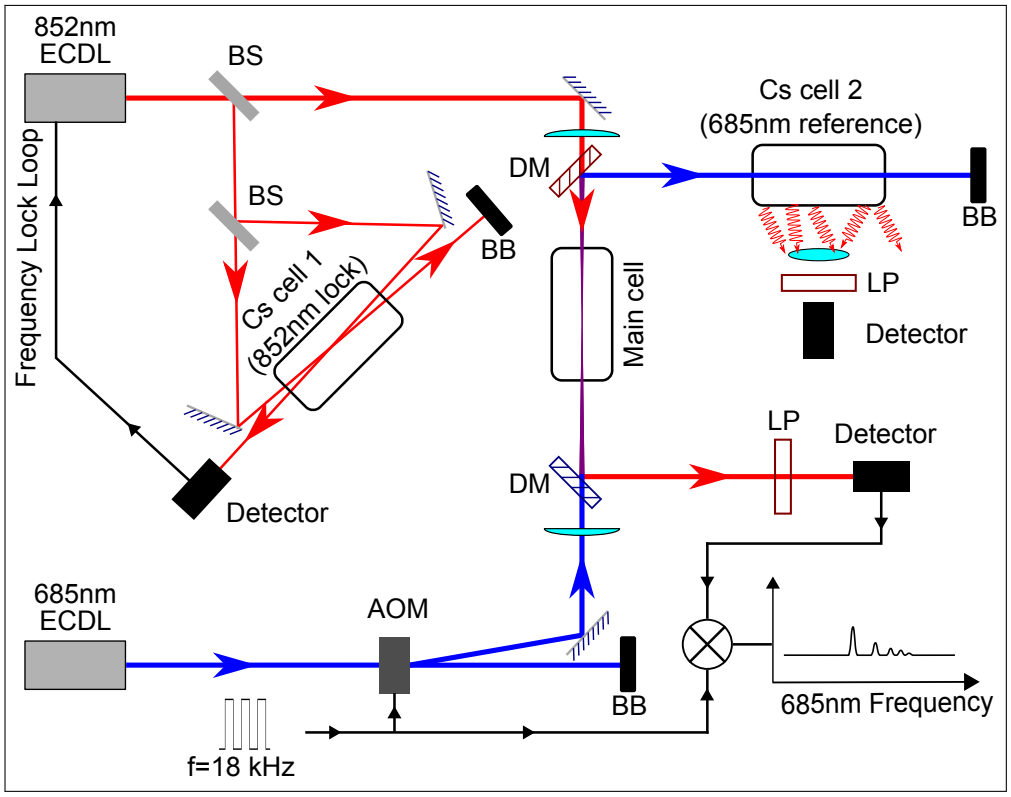

Figure 6.2: Experimental setup (BB: Beam Block, DM: Dichroic Mirror, LP: Long Pass filter, BS, Beam Splitter, ECDL: External Cavity Diode Laser)
Source: Reprinted with permission from [2], Publisher: The Optical Society (OSA)

685 nm laser beam is amplitude-modulated at 18 kHz using an Acousto-Optic Modulator (AOM) operating at 80 MHz. Beams from both 852 nm and 685 nm are focused to a beam waist of 125 µm inside a 5 cm long room-temperature main Cs vapor cell in a counter-propagating configuration. Considering solely fluorescence decay, the saturation intensity of the electric quadrupole line is $I_s = \frac{2\pi^2}{3\lambda^3}\hbar c\frac{{\gamma_{5D}^{\rm se}}^2}{\gamma_{5D-6S}} \sim 2$ Wcm^{-2}, where $\gamma_{5D}^{\rm se} = 2\pi \cdot 124$ kHz is the fluorescence rate of $5^2\mathrm{D}_{5/2}$ state which almost exclusively comes from the $5^2\mathrm{D}_{5/2} \rightarrow 6^2\mathrm{P}_{3/2}$ electric dipole line at 3.5 µm [112]. The 685 nm laser has an output power of 11 mW and a minimum beam waist around $\omega_0 = 125$ µm. So the maximum laser intensity attainable is $I \approx 40$ Wcm^{-2} which should be above the saturation intensity of the transition. However one should note that the saturation intensity is increased by transit broadening of atoms tranversing across the laser beams where the transit relaxation rate, $\gamma_t \sim \langle v_\perp\rangle/w_0 \approx 1.8\gamma_{5D}^{\rm se}$ with the transverse mean thermal velocity across the laser beam, $\langle v_\perp\rangle \approx 170$ ms^{-1}, and the beam waist, $w_0 \approx 125$ µm. Thus the effective I_s is increased by a factor of $\approx \frac{(\gamma_t+\gamma_{5D}^{\rm se})^2}{{\gamma_{5D}^{\rm se}}^2} \sim 8$. The 852 nm peak laser intensity is 2 mW/cm^2, i.e. below saturation intensity of 2.7 mW/cm^2. The 18 kHz modulation amplitude, transfered onto the 852 nm transmission via three-level saturation spectroscopy, is then extracted using a lock-in amplifier. These transmission spectra are recorded as functions of the frequency of the 685 nm laser, with the 852 nm laser frequency locked.

The 685 nm frequency, scanned over the Doppler profile is monitored by collecting the fluorescence at 852 nm in a second auxiliary vapor cell operated at temperature, $T = 55\,^\circ$C (Cell 2 in Figure 6.2). The 685 nm frequency scale is calibrated by comparing the fluorescence spectra obtained with zeroth and first order AOM diffracted beams. With only the 685 nm light, the fluorescence signal at 852 nm comes from the radiative cascade $5^2D_{5/2} \rightarrow 6^2P_{3/2} \rightarrow 6^2S_{1/2}$. An example of a fluorescence spectrum is shown in Figure 6.3. The 685 nm laser is tuned to the $F = 4$ hyperfine ground state. Thus according to the selection rules of a quadrupole transition, the $F = 4 \rightarrow F' = 2, 3, 4, 5\,\&\,6$ lines can be observed. Those transitions are not resolved in Doppler spectroscopy due to the small hyperfine splitting of the $5^2D_{5/2}$ state. However the asymmetry of the fluorescence spectrum is a clear signature of the presence of several transitions. Moreover, we calculate the transitions relative intensities, which are given by the Wigner $6-j$ symbol,

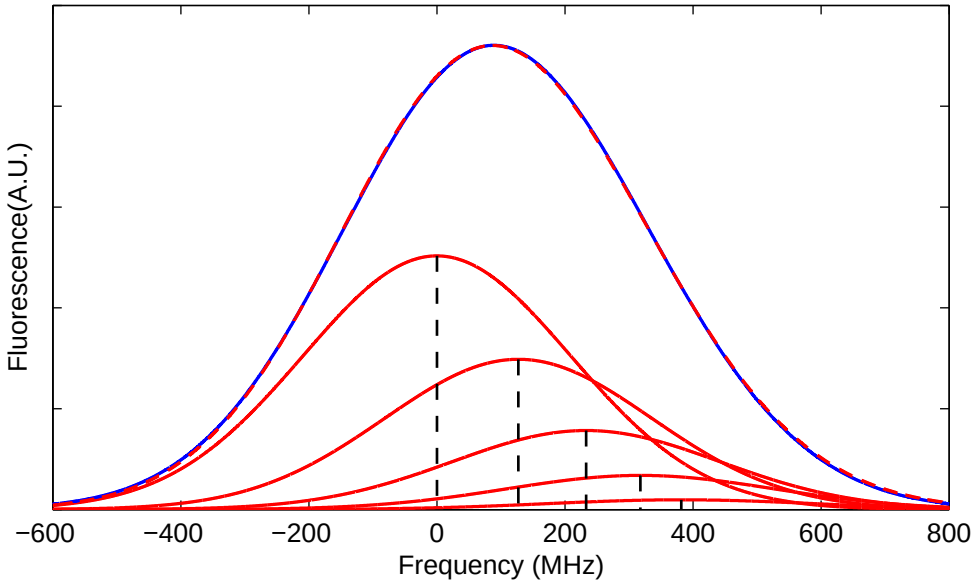

Figure 6.3: Fluorescence spectrum at 852 nm (dashed red curve) where only the 685 nm laser beam is present. The solid blue curve is a fit composed of five Gaussian profiles (red curves). The dashed vertical lines correspond to the relative position of the hyperfine structure. The origin of the frequency is taken at the $F = 4 \rightarrow F = 6$ resonance.
Source: Reprinted with permission from [2], Publisher: The Optical Society (OSA)

using the Wigner-Eckart theorem $(J, F \to J', F')$[113]:

$$S^{Q}_{FF'} = (2F'+1)(2J+1) \begin{Bmatrix} J & J' & 2 \\ F' & F & I \end{Bmatrix}^2 , \tag{6.1}$$

with $I = 7/2$. We now place a Gaussian profile for each hyperfine transition at its correct relative frequency separation (see Figure 6.3) with a relative weight, given by Equation (6.1). Using a global frequency shift and an identical width for the Gaussians as the two free fitting parameters, we are able to recover the experimental profile of the fluorescence signal at 852 nm with an excellent agreement.

6.3 Pump probe results and interpretation

Two variations of the experiment are presented here. In the first variation, we frequency locked the 852 nm probe laser to the $6S_{1/2}(F = 4) \to 6^2P_{3/2}(F' = 5)$ transition whereas the 685 nm laser is scanned across the $6^2S_{1/2}(F = 4)$ to $5^2D_{5/2}(F')$ multiplets. The Doppler-free spectra for the first type is shown in Figure 6.4. Since the lasers at 685 nm and 852 nm are sharing the same $F = 4$ ground state, the signal is revealed mainly through optical de-pumping of this state. Thus the transmission signal at 852 nm will be in-phase with the 18 kHz modulation leading to a positive, i.e. emission-like spectrum, as seen in Figure 6.4. The 685 nm light couples the hyperfine transitions satisfying the quadrupole transition selection rules, i.e. $-2 \leq \Delta F \leq 2$. Thus the excitation spectra are on the $F = 4 \to F' = 2, 3, 4, 5\,\&\,6$ lines.

In the second variation, we frequency locked the 852 nm probe laser to the same $6^2S_{1/2}(F = 4) \to 6^2P_{3/2}(F' = 5)$ hyperfine transition and scan the 685 nm laser across the $6^2S_{1/2}(F = 3)$ to $5^2D_{5/2}(F')$ multiplet. The spectrum is shown in Figure 6.5. The 685 nm and 852 nm lasers are not sharing the same ground state and the signal is solely due to the optical re-pumping to the ground state. This is observed as an absorption-like spectrum that is in antiphase with the 18 kHz modulation. Here the optical re-pumping from the ground state $F = 3$ to the ground state $F = 4$ is done through a 685 nm absorption event followed by a $5^2D_{5/2} \to 6^2P_{3/2} \to 6^2S_{1/2}$ radiative cascade event. Both absorption and radiative decays events have the same $-2 \leq \Delta F \leq 2$ selection rules. Thus only the four $F = 3 \to F' = 2, 3, 4\,\&\,5$ lines of the electric quadrupole transition are observed, whereas the $F = 3 \to F' = 1$ transition is missing since it cannot decay back to the $6^2S_{1/2}\,F = 4$ state.

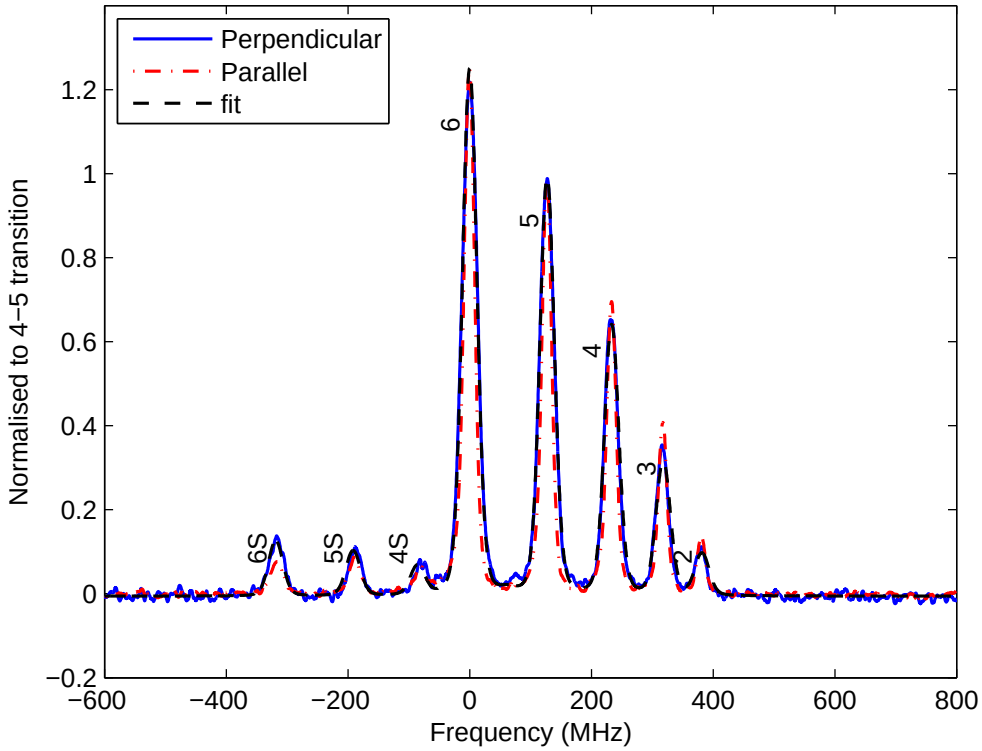

Figure 6.4: Doppler free spectra with 852 nm light locked on $6^2S_{1/2}(F = 4) \rightarrow 6^2P_{3/2}(F' = 5)$ and 685 nm light scanned across the $6^2S_{1/2}(F = 4)$ to $5^2D_{5/2}(F' = 2\text{–}6)$ transitions. Peaks marked with S correspond to sideband contributions from the $6^2S_{1/2}(F = 4) \rightarrow 6^2P_{3/2}(F' = 4)$ transition for a non-zero velocity group. The blue solid curve corresponds to the spectrum where the 685 nm and 852 nm beams polarizations are perpendicular. The dotted dashed curve is for parallel polarizations. The dashed black curve is a fit of Equation (6.2) with $\alpha = 0.56$.

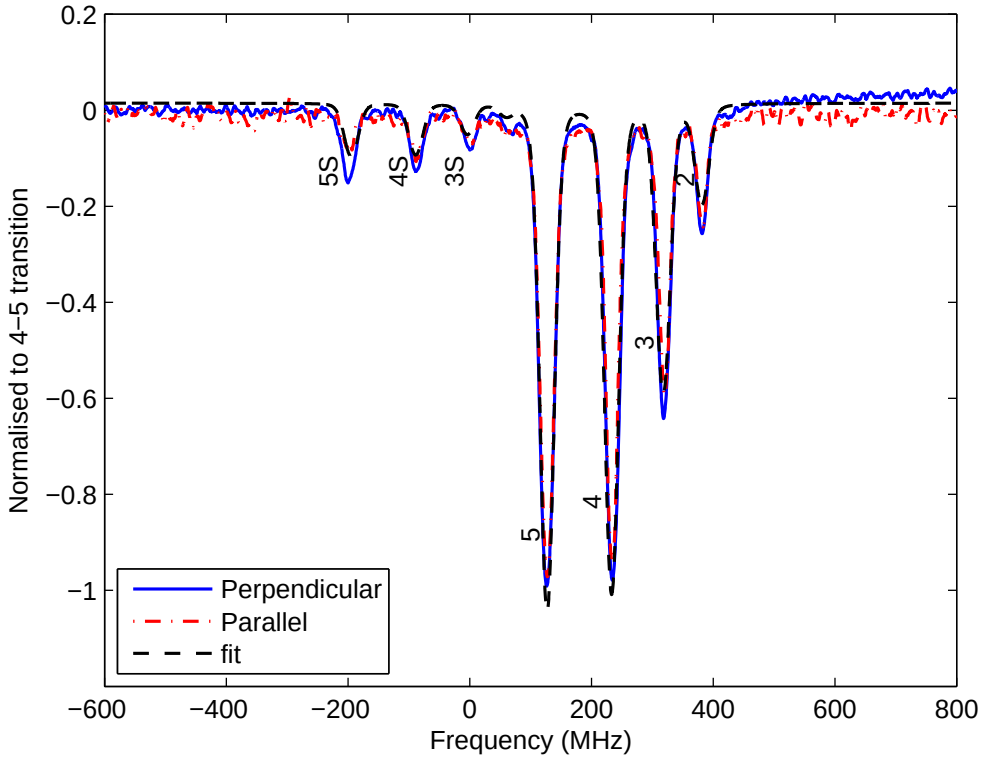

Figure 6.5: Doppler free spectra with 852 nm light locked on $6^2S_{1/2}(F = 4) \rightarrow 6^2P_{3/2}(F' = 5)$ and 685 nm light scanned across the $6^2S_{1/2}(F = 3)$ to $5^2D_{5/2}(F' = 2\text{–}5)$ transitions. We use the same notation as in Figure 6.4
Source: Reprinted with permission from [2], Publisher: The Optical Society (OSA)

Small amplitudes transmission peaks, appearing on the red side of the main resonances (marked with S in Figures 6.4 and 6.5) are sideband resonances. They correspond to the $6S_{1/2}(F = 4) \rightarrow 6P_{3/2}(F = 4)$ transition resonantly excited for a non-zero atomic velocity group[109, 110]. Taking into account the different Doppler shifts, we find a frequency shift between the two sets of resonances of $\vec{k}_{685}/\vec{k}_{852} \times \Delta_{5-4} = -312\,\mathrm{MHz}$, where $\Delta_{5-4} = 251\,\mathrm{MHz}$ is the $F = 5 - F = 4$ hyperfine splitting of the $6^2P_{3/2}$ excited state. Since the laser beams are counter propagating, the sidebands lie on the red side of the resonances. We like to mention that with co-propagating beams, the shift would be on the blue side of the main resonances.

In these two cases, we use only linear polarization for both lasers and we observe that the spectra do not depend on the relative polarization of the pump and probe lasers. We attribute the polarization independence of the spectra to the near-equivalence of linearly polarized radiation to an isotropic light probe for $F = 4 - F' = 5$ excitation, which results in the lack of dark Zeeman states in the ground state of the probe beam. This allows us to consider that the line intensities now only depend on the hyperfine transitional strength factors $S^Q_{FF'}$ of electric quadrupole absorption line (Equation (6.1)), and electric dipole emission line strengths. The full calculation for the two variations is given in Section 6.3.1.

6.3.1 Characterization of the pump - probe signal

In this subsection, we calculate the pump - probe line intensities by considering the depopulation and repopulation in the 6S level. The signal strength can be written as

$$S(F_1, F, F_2) = \delta_{F_1,F_2} S^Q_{F_1F} - \alpha \sum_{F''} S^Q_{F_1F} S^D_{FF''} S^D_{F''F_2} \ , \tag{6.2}$$

where F_1 is the hyperfine ground state $6^2S_{1/2}(F_1)$ de-pumped by the 685 nm laser, F is the hyperfine excited state $5^2D_{5/2}(F)$, F'' is the hyperfine intermediate state $6^2P_{3/2}(F'')$ in the decay process, F_2 is the final hyperfine ground state $6^2S_{1/2}(F_2)$ of the decay channel, $\delta_{i,j}$ is the Kronecker delta, $S^D_{F'F''}$ is the electric dipole emission line strengths as given by

$$S^D_{F'F''} = (2F'' + 1)(2J' + 1) \begin{Bmatrix} J' & J'' & 1 \\ F'' & F' & I \end{Bmatrix}^2 . \tag{6.3}$$

The sum is over the $6^2P_{3/2}(F'')$ hyperfine levels (F indicates the pumped $5^2\mathrm{D}_{5/2}$ hyperfine state) and

$$\alpha = \frac{\gamma_{5D}^{\mathrm{se}}}{\gamma_t + \gamma_{5D}^{\mathrm{se}}}, \tag{6.4}$$

is a re-pumping ratio which takes into account the transit relaxation rate due to transit time of atoms through the laser beams, γ_t. This transit relaxation is mainly effective in the long-lived 5D state.

An increase in the transit relaxation rate diminishes the re-pumping back to the ground state (the second term in Equation (6.2)). The transit relaxation rate may be approximated roughly by $\gamma_t \sim \langle v_\perp \rangle / w_0$. With the transverse mean thermal velocity across the laser beam, $\langle v_\perp \rangle \approx 170\ \mathrm{ms}^{-1}$, and the beam waist, $w_0 \approx 125\,\mu\mathrm{m}$, we predict $\alpha \approx 0.4$.

To check our theoretical calculation in Equation (6.2), we fit our Doppler-free spectra in Figures 6.4 and 6.5 with Voigt lineshapes (See Equation (3.13) for the Voigt expression we use), with the Gaussian linewidth as one of the fitting parameters and the Lorentzian linewidth as $852/685 \times \gamma_{6P-6S} \approx 2\pi \cdot 6.6\,\mathrm{MHz}$, where the ratio 852/685 is the difference in wavenumbers between the wavelengths at 685 nm and at 852 nm [109, 110]. The Voigt profile amplitudes correspond to the signal strengths calculated from Equation (6.2). The fitting parameters are a global amplitude, the Gaussian linewidth and the repumping ratio α. If $F_1 = F_2$ (same hyperfine ground state), the line intensity depends on both de-population and re-population pumping, as well as on the transit time relaxation.

As shown in Figure 6.4, a very good match is obtained for $\alpha = 0.56 \pm 0.02$ (i.e. $\gamma_t = 1.8\gamma_{5D}^{\mathrm{se}}$) a value not far from the rough estimate above. Note the major role of transit broadening. In its absence ($\alpha = 1$), the repopulation in the $F = 4$ ground state [after electric quadrupole excitation to the $5^2D_{5/2}(F = 6)$ level] should exactly cancel the depopulation pumping (inside the close three-level system, $F = 4 - 6 - 5 - 4$). The observation of the $F = 6$ resonance (Figure 6.4) is a direct evidence for the transit time influence responsible for losses in the optical pumping process. On the other hand, for the $F_1 \neq F_2$ cross resonances (Figure 6.5), there is no optical pumping on the ground state and the overall spectrum amplitude depends only on signal strengths of all the possible channels of the repopulation, which is the second term of Equation (6.2). As shown in Figure 6.5, a very good agreement is obtained considering only the signal strengths of the repopulation. From the experimental fits, we find the Gaussian linewidth to be about 15 MHz. The

extra broadening may be due to the 852 nm power broadening, collisions and the 685 nm laser jitter.

6.4 Polarization dependency in the spectrum

In the previous section, we only consider the hyperfine line strength transitions in our evaluation of our pump-probe data. It explains the spectra in Figures 6.4 and 6.5 that do not show polarization dependencies between the pump and the probe. In this section, we perform another set of experiment by frequency locking the 852 nm laser to the $6^2S_{1/2}(F = 4) \rightarrow 6^2P_{3/2}(F' = 4)$ transition whilst scanning the 685 nm laser across the $6^2S_{1/2}(F = 4)$ to $5^2D_{5/2}(F')$ multiplets. Similarly to the spectra in Figure 6.4, the signal is mainly due to optical de-pumping of the shared ground state which resulted in an emission-like spectrum. However, in contrast to the $6^2\mathrm{S}_{1/2}(F = 4) \rightarrow 6^2\mathrm{P}_{3/2}(F' = 5)$ transition, we observe a higher "emission" spectrum for orthogonal polarization between the 685 nm and 852 nm beams than that for parallel polarization between the two beams for the excitation of the $6^2\mathrm{S}_{1/2}(F = 4) \rightarrow 6^2\mathrm{P}_{3/2}(F' = 4)$ and $6^2\mathrm{S}_{1/2}(F = 4) \rightarrow 6^2\mathrm{P}_{3/2}(F' = 3)$ transitions. The spectrum is shown in Figure 6.6. The difference in the spectra between the two polarizations suggests that the transition strengths and populations of the magnetic sublevels of the shared ground states in $6^2\mathrm{S}_{1/2}(F = 4)$ play a role in the experiment.

We propose one possible interpretation for the discrepancy between the spectra for the two polarizations. We choose the electric field axis of the 685 nm pump as the quantization axis of the atoms. For parallel polarization between the two beams, the selection rule for 852 nm probe is $\Delta m_F = 0$. The selection rule prevents the excitation by the probe from $6^2\mathrm{S}_{1/2}(F = 4,\, m_F = 0)$ to $6^2\mathrm{P}_{3/2}(F' = 4,\, m'_F = 0)$. This creates a dark state in the $m_F = 0$ ground state. For excitation from $6^2\mathrm{S}_{1/2}(F = 4,\, m_F = \pm 4)$ to $6\mathrm{P}_{3/2}(F' = 3)$ is not possible and therefore there are also dark states in $m_f = \pm 4$. In contrast, the selection rules dictate that coupling from all m_Fs states from $6^2\mathrm{S}_{1/2}(F = 4,\, m_f = \pm 4)$ to $6^2\mathrm{P}_{3/2}(F' = 5)$ are allowed. For perpendicular polarization, the selection rule for 852 nm probe is $\Delta m_f = \pm 1$. There are no dark states for couplings from $6^2\mathrm{S}_{1/2}(F = 4)$ to all three hyperfine states in $6^2\mathrm{P}_{3/2}(F = 3, 4, 5)$. The absence of dark states in perpendicular polarization is in contrast to the parallel polarization. This could explains the higher optical de-pumping signals in the perpendicular signals. For a full analysis of the signal stength

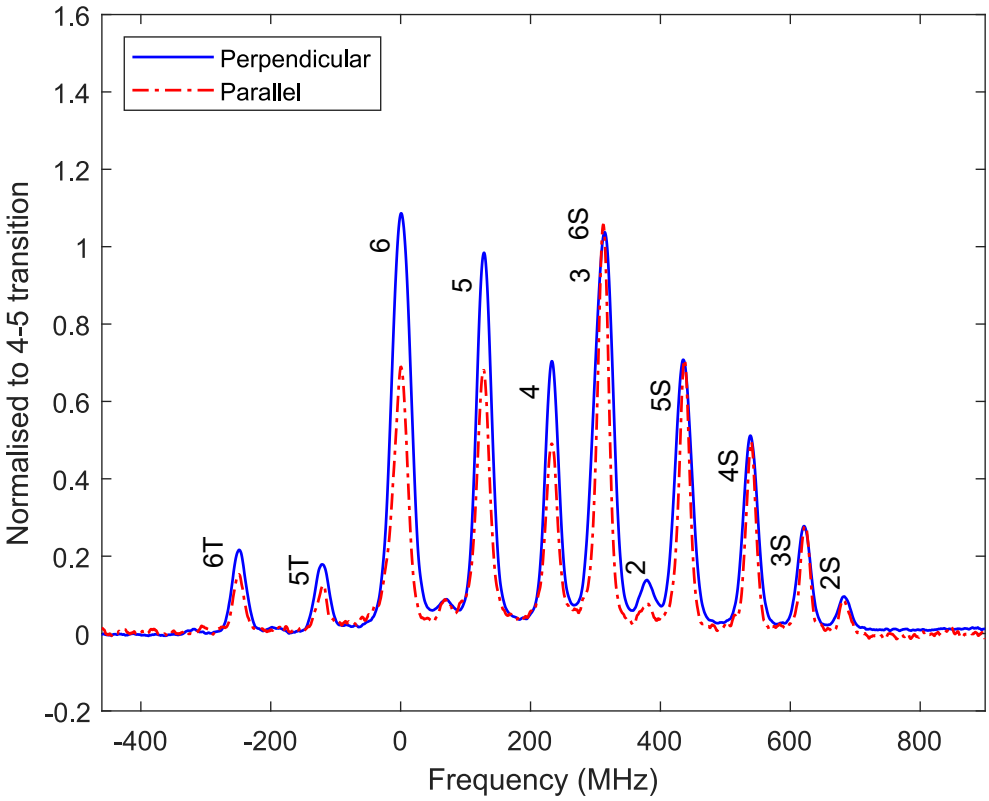

Figure 6.6: Doppler free spectra with 852 nm light locked on $6^2\mathrm{S}_{1/2}(F = 4) \rightarrow 6^2\mathrm{P}_{3/2}(F' = 4)$ and 685 nm light scanned across the $6^2S_{1/2}(F = 4)$ to $5^2D_{5/2}(F' = 2\text{–}6)$ transitions. Peaks marked with S correspond to sideband contributions from the $6^2\mathrm{S}_{1/2}(F = 4) \rightarrow 6^2\mathrm{P}_{3/2}(F' = 5)$ transition from a negative non-zero velocity group. Peak 6S overlaps with peak 3. Peaks marked with T correspond to sideband contributions from the $6^2\mathrm{S}_{1/2}(F = 4) \rightarrow 6^2\mathrm{P}_{3/2}(F' = 3)$ transition from a positive non-zero velocity group.

one requires to consider the optical de-pumping across the Zeeman states by the pump beam, the optical re-pumping by the $5^2D_{5/2} \rightarrow 6^2P_{3/2} \rightarrow 6^2S_{1/2}$ two-steps decay as well as electric dipole transition probabilities of the Zeeman states:

$$S(F_1, F, F_2) = \sum_{m_{F_2}, m_{F''}} \sigma_{m_{F_2}}(F_1, F, F_2) |\langle 6^2S_{1/2} F_2 m_{F_2} | D_\lambda | 6^2P_{3/2} F'' m_{F''} \rangle|^2 \tag{6.5}$$

where $\sigma_{m_{F_2}}(F_1, F, F_2)$ is the population distribution across the Zeeman ground states m_{F_2} locked by the 852 nm probe, D_λ is the electric dipole matrix element for 852 nm with polarization λ. $\sigma_{m_{F_2}}(F_1, F, F_2)$ can be solved by rate equations approach [114, 115] and interpreting the Doppler-free non-linear spectroscopy considering the magnetic sublevels can be a project for future research.

6.5 Conclusion

We have observed Doppler-free spectral lines on the Cs $6^2S_{1/2} - 5^2D_{5/2}$ transition and analyzed properties such as the selection rules and saturation intensities in Section 6.3.1. In a more general case in which optical pumping and dark states in ground state Zeeman levels are non-negligible, the electric quadrupole absorption depends on the relative polarization of the pump and probe. This is discussed in Section 6.4. Optical pumping of our three level Raman-type electric quadrupole transition pump - probe can be a topic of interest for future studies. In addition, comparison of electric quadrupole absorption between using Gaussian light beams (our case) and using Laguerre-Gauss (LG) beams could also be done. Angular momentum conservation in matter-light interaction involves photon spin only in Gaussian light beams. In the work presented here, one thus expects to induce $\Delta M = \pm 1$ transitions in electric quadrupole absorption at 685 nm. If instead one uses focused Laguerre-Gauss (LG) beams, one expects that orbital angular momentum of light can be absorbed and thus produce $\Delta M = 0, \pm 1, \pm 2$ transitions[116, 117]. These could be observed via electric quadrupole Zeeman transitions in applied magnetic fields. electric quadrupole transitions can be monitored in zero-electric-field regions of LG beams and should allow one to map their spatial intensity distributions[117]. This chapter also paves the way for further investigation on the influence of near-field surface potentials on electric quadrupole line emission, which is the topic of interest in Chapter 7 where we will attempt to monitor the atom

response on electric quadrupole transitions in the vicinity of metamaterials.

This chapter is an adaptation from Optics Letters **41**(9),2005-2008 by Chan *et al.*, under OSA's "Copyright Transfer and Open Access Publishing Agreement" (OAPA). Exclusive licensee - The Optical Society (OSA). Some addition and revision of the original text are done.

Chapter 7

Coupling of electric quadrupole transition with localized surface plasmon

7.1 Motivation

The plasmon - atom interaction has been investigated in Chapters 4 and 5 through resonant coupling on an atomic dipole transition. In Chapter 4, we demonstrate tuning of Casimir-Polder force on a dipole transition by coupling with metamaterial. In Chapter 5, we miniaturize the atom-plasmon interface to a fiber tip. There are interest to access higher order transitions wherein some of them are energetically isolated, and can be addressed individually, far-off resonance from strong electric dipole transitions. Accessing them opens up plethora of possibilities in terms of enabling new atom/light coupling, and possibly new cooling techniques in cold atomic physics. However, in free space the coupling constant of an emitter of order n diminished according to $\alpha(2\pi a_0/\lambda)^n$ [118], α is the fine structure constant, a_0 is the characteristic size of the emitter, λ is the wavelength of transition in freespace. Higher order transitions are thus usually considered as forbidden transitions. Nevertheless, close to a plasmonic surface, the electromagnetic field is hybridized with surface modes, and its effective wavelength diminishes leading to higher transition rates for the forbidden transitions. Rivera and co-authors suggested two-dimensional materials with large confinement factors [119] at a very close distance. In this extreme regime, all transitions could have similar

oscillator strength, conducting to a deep modification of the excitation and emission spectrum of atoms which could be exploited for tests of the quantum electrodynamic theory in some regimes never obtained so far. Positioning an atom that close to a two-dimensional material could prove to be an experimental challenge. Instead, in this chapter, we report on the observation of electric quadrupole excitation of a cesium atomic vapor at the vicinity of a metallic metamaterial. Here, the confinement of the plasmon modes is weaker but still sufficient to observe a strong enhancement. More precisely we aim to observe enhancement effect due to higher electric field gradients, as it was proposed with plasmon modes at the vicinity of metallic nano-rods [27].

The metamaterial-vapor system is probed using selective reflection spectroscopy techniques in a pump - probe configuration as introduced in Chapter 6. In Section 7.2, we discuss the experimental setup. In particular, we use a pump/probe technique which consists of a pump laser, tuned at 685 nm excites both a plasmonic resonance of the metamaterial and the cesium $6^2S_{1/2} - 5^2D_{5/2}$ electric quadrupole transition and a probe laser that probes the induced modification of the atomic ground state population on the $6^2S_{1/2} - 6^2P_{3/2}$ electric dipole transition at 852 nm. Both laser beams are normal to the surface leading to a Doppler-free signal. Surprisingly, we did not observe an enhancement effect with respet to a bare dielectric interface. Then, in Section 7.3, using selective reflection theory derived in Section 2.2, we shows that simplifying the metamaterial as a homogenous material with complex refractive index is sufficient to explain the pump-probe spectrum. The subwavelength light confinement of the metamaterial does not seemed to play a role because the localized surface plasmons have large wavevector, coupled with atom vapor with high velocities (Doppler broadening) washes out the enhancement effect on the selective reflection spectrum, as shown in theoretical calculations using full description of the electric fields in Sections 7.5 and 7.6. The remaining effect of the the Doppler broadening suppose to create an offset in the selective reflection spectrum as shown in Section 7.7 but it is difficult to observe experimentally due to systematic errors in the experiment.

7.2 Experimental Setup

A general sketch of the experimental setup is shown on Figure 7.1(a). A vacuum chamber is brought at a temperature of 90°C, and filled up with

cesium atoms at saturated vapor pressure. The typical atomic density is 8×10^{12} cm^{-3}. The atomic density is determined from optical transmission spectroscopy narrated in Section 3.7. The design of the vacuum apparatus is discussed in Section 3.1. On a fused-silica viewport, a periodic pattern of nano-slit metamaterial is engraved (See Section 3.2.2). The period and the unit cell structure (Metamaterial 11 in Table 3.1) are designed such that the metamaterial host a fundamental resonant plasmonic mode at 615 nm, almost coinciding with the cesium $6^2S_{1/2} - 5^2D_{5/2}$ electric quadrupole transition (See Figure 7.1(b-c).

All the relevant spectra are obtained using a pump-probe technique. A weak 852 nm probe laser is frequency locked on the $6^2S_{1/2}(F = 4) - 6^2P_{3/2}(F' = 5)$ hyperfine transition (cesium cell 1 in Figure 7.1(a) using a Pound-Drever-Hall circuit discussed in Section 3.6. In addition, an intensity-modulated 685 nm pump laser is scanned across the $6^2S_{1/2}(F = 4) - 5^2D_{5/2}(F' = 6)$ hyperfine transition, see Figure 7.1(c). When the pump laser is at resonance, both lasers addressed the zero velocity class. As a result, the ground state population is periodically decreased by the pump laser and modify the probe laser interaction with the vapor. Then, we demodulate the probe signal at the pump intensity modulation frequency, to provide a sensitive and ideally background-free detection technique of the ground state population. A pump-probe setup (Details are presented in Chapter 6) is employed in transmission through a vapor cell for frequency reference purpose (cesium cell 2 in Figure 7.1a). A second pump-probe setup performs selective reflection spectroscopy on the atoms-metamaterial system (vacuum cell in Figure 7.1a). The two laser beams are co-propagating and pump laser beam has a waist of 150 µm, probe laser beam is imaged with 200 µm by 200 µm mask on the metamaterial with imaging setup in Section 3.3. The reflected beams go across a colored and an low-pass interference filter to remove the 685 nm beams and detect solely the 852 nm beam. In practical a small fraction of the 685 nm light ($\sim 10^{-7}$ of the incident power) will be also detected and demodulated, which lead to an unwanted global offset of the selective reflection signal.

Using selective reflection spectroscopy, we analyze the reflection properties of the probe laser at 852 nm at an interface between the cesium vapor and, either a dielectric, or the surface metamaterial. The pump-probe setup allows us to observe the weak modification of the reflection coefficient induced by exitation at 685 nm on the 852 nm beam. A direct observation of selective reflection signal on the quadrupole transition, using a cesium vapor is possible

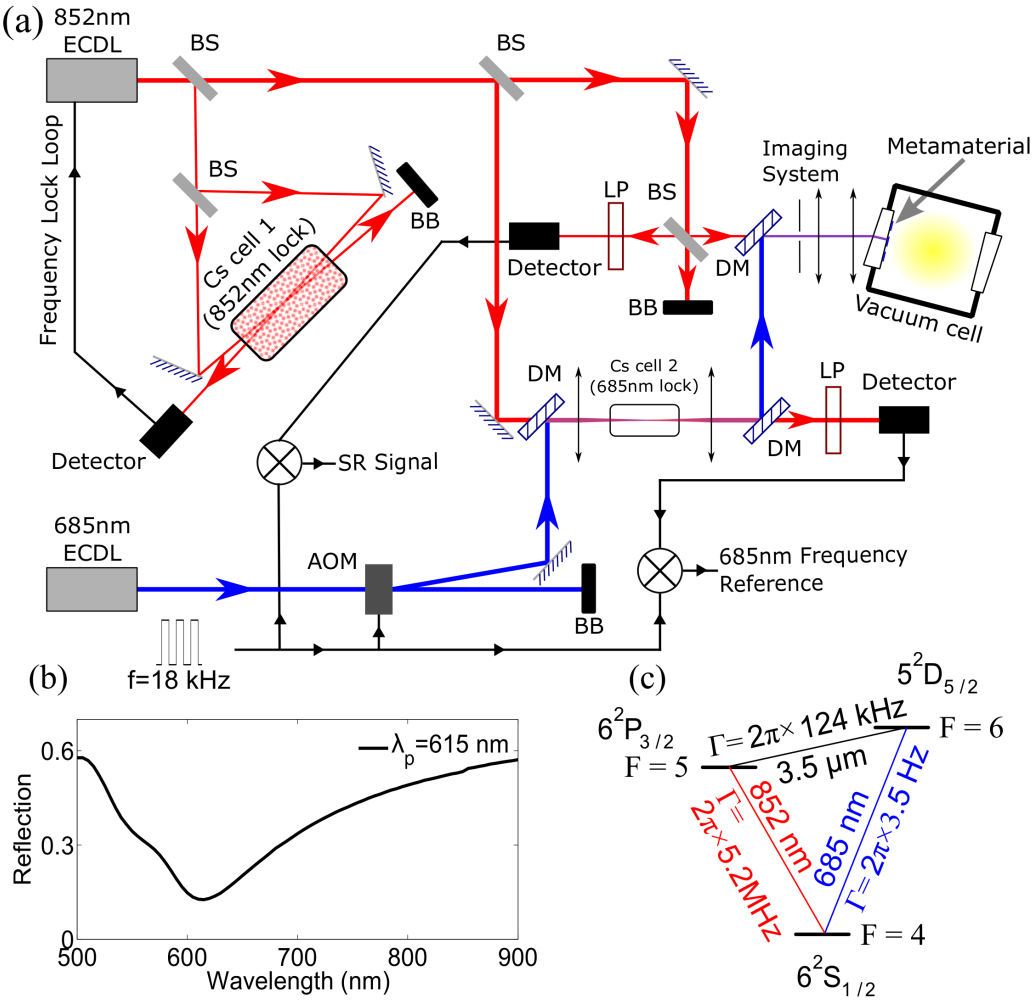

Figure 7.1: (a) Sketch of the experimental setup (b) Reflection spectrum of the metamaterial. (c) Cesium energy levels and transitions of interest. Blue; Pump beam, Red; Probe beam ECDL, external cavity diode laser; BS, beamsplitter; BB, beamblock; LP, longpass filter; DM, dichroic mirror; AOM, acousto-optic modulator

but would require much higher atomic density. The pump-probe selective reflection signal improvement is roughly given by the bare excited linewidth ratio $\gamma(6^2\mathrm{P}_{3/2})/\gamma(5^2\mathrm{D}_{5/2}) \simeq 40$. This signal improvement goes with a broadening of the selective reflection signal imposed by the large dipole transition. The broadening of the signal is seen in the experimental results in Section 7.3.

The observed relative modification of the reflection coefficient is of the order of 10^{-8} and have required several days of continuous integration. To avoid frequency drifts of the 685 nm laser during acquisition, we record the pump-probe transmission signal of the bulk reference cell (see Chapter 6) The centre-of-mass of the spectrum is calculated in real time (at a rate of $5\,\mathrm{s}^{-1}$) to find the mean laser frequency. A laser frequency drift is transposed into an error signal which is feedback to the piezoelectric ceramic controlling the laser cavity length.

7.3 Selective reflection and mean-field interpretation

We first consider a single interface between a homogenous dielectric material and the atomic vapor, see Figure 7.2. After some algebra, discussed in Section 2.2.5, one substitute Equation (2.33) into Equation (2.20) and taking Boltzmann velocity distribution $1/(\sqrt{\pi}\bar{u})\mathrm{e}^{v_z^2/\bar{u}^2}$, where $\bar{u}$ is the thermal velocity and we include the modulation of shared ground state Π_g by the electric quadrupole transition as a product in the integral, one finds that the effective susceptibility of the vapor for selective reflection at normal incidence reads :

$$\bar{\chi}(\delta) = iN\frac{2\mu_d^2}{\sqrt{2\pi}\epsilon_0\hbar\bar{u}}\int_0^{+\infty}\mathrm{d}v_z\Pi_g\frac{\mathrm{e}^{-v_z^2/2\bar{u}^2}}{\gamma_d/2 - i(\delta_d - k_d v_z)} \tag{7.1}$$

where ϵ_0, $\hbar$ are the vacuum permittivity and the Planck constant respectively. μ, γ, δ, and k are the atomic dipole moment, the bare linewidth of the excited state, the frequency detuning and the laser wavenumber, respectively. If the subscript letter d is attached to these quantities, we refer to the electric dipole transition $6^2\mathrm{S}_{1/2} - 6^2\mathrm{P}_{3/2}$. On the other hand, the absence of subscripts indicates that we consider the electric quadrupole transition $6^2\mathrm{S}_{1/2} - 5^2\mathrm{D}_{5/2}$. To simplify our theoretical approach, we disregard the fine and hyperfine structure of the transitions, the van der Waal surface interaction. Moreover, we use the weak field limit where the laser intensity is below the saturation

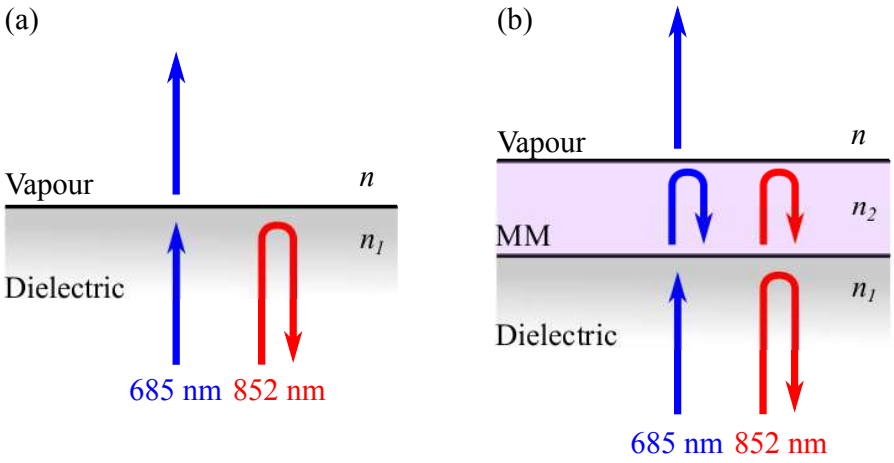

Figure 7.2: Geometry of the laser beams at; (a) the dielectric-vapor interface, and (b) the dielectric-metamaterial-vapor interface. In the mean-field approximation, the metamaterial is replaced by a homogenous material which as the same index of refraction and attenuation coefficient. U-arrows on metamaterial layer indicates that only single reflection from metamaterial-vapor interface is considered because of large absorption in metamaterial (see text for more details.)

intensity. The asymmetry in the velocity integration in Equation (7.1) is a consequence of the presence of the interface. N is the atomic density and Π_g is the ground state ($6^2S_{1/2}$) population density. In presence of the 685 nm pump laser, one has

$$\Pi_g = 1 - \frac{I}{2I_s}\frac{\gamma^2}{4(\delta - kv_z)^2 + \gamma^2}. \tag{7.2}$$

for $v_z \leq 0$ and unitary when $v_z > 0$, $I = TI_0 \simeq 0.2\,\mathrm{Wcm}^{-2}$ is the modulated pump laser intensity and $I_s = 2\,\mathrm{Wcm}^{-2}$ the saturation intensity. I_0 is the incident laser intensity and $T = 4n_1/(n_1+1)^2 \simeq 0.96$ the intensity transmission coefficient at 685 nm of the dielectric-vapor interface. $n_1 = 1.45$ is the index of refraction of the dielectric. Since $\gamma \ll \gamma_d, k\bar{v}, k_d\bar{v}$, we replace the factor $1/(4(\delta - kv_z)^2 + \gamma^2)$ by $\pi\delta_D(\delta - kv_z)/2\gamma$ in Equation (7.1) where $\delta_D(x)$ is the Dirac δ-function. Under this approximation the susceptibility takes the following analytical form,

$$\bar{\chi}(\delta) = \bar{\chi}_0 - i\frac{\sqrt{\pi}\mu_d^2}{\epsilon_0\hbar\bar{v}}\frac{I}{2I_s}\frac{\gamma}{\kappa k}\frac{\mathrm{e}^{-\delta^2/2k\bar{u}^2}}{\gamma/(2\kappa) + i\delta}\Theta(-\delta). \tag{7.3}$$

$\Theta(x)$ is the step function, and $\kappa = k_d/k = 0.8$. Here the probe laser at 852 nm is maintained at resonance, so $\delta_d = 0$. $\bar{\chi}_0 = iN\frac{2\mu_d^2}{\sqrt{2\pi}\epsilon_0\hbar\bar{u}}\int_0^\infty \mathrm{d}v_z \frac{\mathrm{e}^{-v_z^2/2\bar{u}^2}}{\gamma_d - i(\delta_d - k_d v_z)}$ is the pump intensity independent part of the effective susceptibility which does not contribute to the demodulated selective reflection signal and is regarded as a constant in our experiment. The effective susceptibility, depicted in Equation (7.3), has a simple physical interpretation. For $\delta \leq 0$, it corresponds to the susceptibility of an atomic ensemble at rest with a bare linewidth of γ/κ. For $\delta > 0$ the susceptibility is zero (see dashed black curve in Figure 7.3a).

Since the medium is diluted, $\bar{\chi} \ll 1$, and the vapor index of refraction is $n \simeq 1 + \bar{\chi}/2$. Thus, the intensity reflection coefficient of the probe is

$$R = |r_0|^2 + 2\mathrm{Re}\{r_0^*\rho\bar{\chi}\}, \tag{7.4}$$

where $r_0 = (n_1 - 1)/(n_1 + 1)$ is the amplitude reflection coefficient without atomic vapor and $\rho = dr/2dn|_{n=1} = -n_1/(n_1+1)^2$. The demodulated signal corresponds to the variation of the intensity reflection coefficient, $\Delta R = 2\mathrm{Re}\{r_0^*\rho\bar{\chi}\}$, due to the atomic vapor and in presence of the 685 nm pump laser. Since r_0, and ρ are real quantities, the demodulated signal is proportional to the real part of $\bar{\chi}$ (see Equation (7.4). On Figure 7.3(b), we

show the relative reflection coefficient $\Delta R/\langle R\rangle$ of the probe laser at 852 nm as function of the pump 685 nm laser frequency. $\langle R\rangle$ corresponds to the mean intensity reflection coefficient (DC component of the reflected signal). Since part of the reflected 685 nm laser is also detected, the demodulated signal shows a significant offset signal which has been numerically removed. The theoretical curves are given by inserting Equation (7.1) into Equation (7.4), and retaining only the demodulated term proportional to I. The experimental signal is in very good agreement with the expected theoretical prediction (see black dashed curve on Figure 7.3(b). However, we have to artificially broaden the pump transition to 1 MHz, and probe transition to 20 MHz. These extra transition broadening might be due to atom-atom collisions, and Casimir-Polder interactions, as it was reported in similar studies [80, 1, 120], and might be due as well to finite pump laser linewidth.

On Figure 7.3(c), we show the selective reflection signal obtained for the dielectric - metamaterial - vapor interface. We observed similar features than for the dielectric-vapor interface, indicating that no further frequency broadening mechanisms are at play on the selective reflection signal. We observe as well an substantial reduction of the signal amplitude of almost one order of magnitude.

To compare the experimental data with the model, developed above, for a dielectric interface, we carry out a mean-field approximation of the metamaterial. It consists of replacing the metamaterial by an homogenous material which has the same thickness and the same far-field transmission and reflection properties. Using FDFD comsol simulations, we find that the homogenous material is characterized by a complex index of refraction of $n_2 \simeq 0.02 + \mathrm{i}3.65$ at the probe wavelength 852 nm. The total intensity transmission of the metamaterial layer at 852 nm is predicted at $T_d = n_1 \left|4n_2/\left[(n_1+n_2)(n_2+1)\right]\right|^2 e^{(-2\mathrm{Im}\{n_2\}k_d L)} = 0.1$ in agreement with the measured value of 0.13. Here $L = 50$ nm is the metamaterial thickness. Since $2\mathrm{Im}\{n_2\}k_d L \simeq 2.7$, the absorption in the metamaterial material is large and only one passage in the metamaterial is considered (multi reflections can be ignored), see illustration in Figure 7.2(b). We follow this approximation, to calculate the reflection coefficient of the dielectric-metamaterial-vapor interface and found: $r_0 = (n_1 - n_2)/(n_1 + n_2)$ and $\rho = -4n_1 \left(n_2/\left[(n_2+1)(n_2+n_1)\right]\right)^2 \mathrm{e}^{(-2in_2k_dL)}$. Here, r_0 and ρ are complex quantities, meaning that the general selective reflection signal, given by Equation (7.4), with metamaterial is a mixture of the absorptive (imaginary) and reactive (real) part of the atomic susceptibility. At the pump frequency a plasmonic resonance is present leading

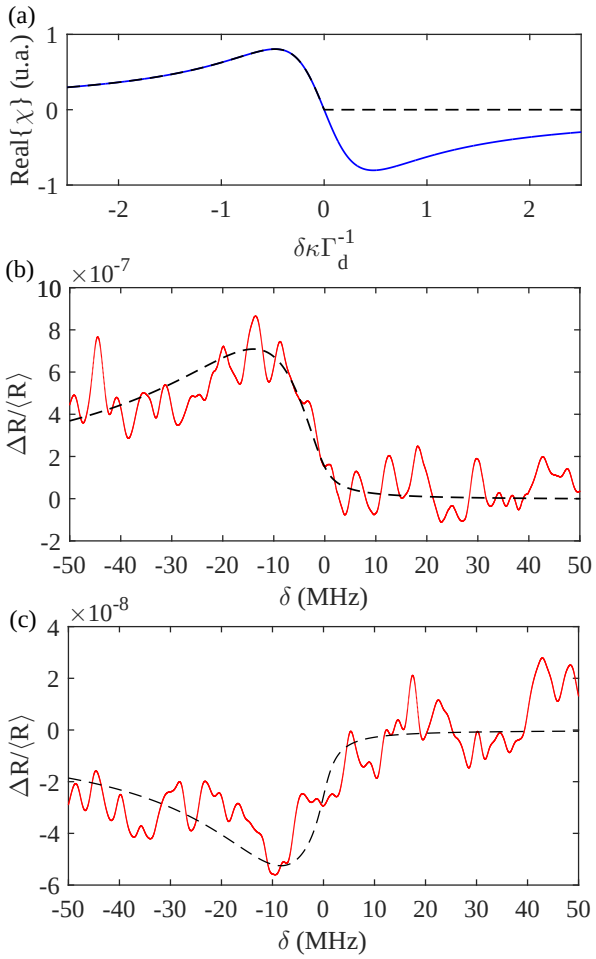

Figure 7.3: Experimental (red) and theoretical (dashed black) curves as function of the 685 nm laser frequency detuning. The frequency origin corresponds to the $6^2S_{1/2}(F = 4) - 5^2D_{5/2}(F'' = 6)$ hyperfine transition. (a) Real part of the effective susceptibility given by Equation (7.3). The linewidth corresponds to $\gamma_d/\kappa = 6.5$ MHz. The blue curve corresponds to the susceptibility of a bulk atomic ensemble at rest. (b) Relative reflection coefficient. The experiment is performed on a dielectric-vapor interface. (c) Relative reflection coefficient. The experiment is performed on a surface metamaterial-vapor interface. The selective reflection signal is weaker for the metamaterial in agreement with the mean-field approximation.

to a large total transmission coefficient, measured to be $T \simeq 0.77$. Following the same procedure than depicted earlier for the dielectric-vapor interface, we estimate the quantity $\Delta R/\langle R\rangle$, see black-dashed curves in Figure 7.3c. A same fitting parameter for the overall amplitude of the theoretical curves, is used for both the dielectric, and metamaterial cases.

The mean-field approximation gives an very good prediction of the selective reflection signal on the dielectric-metamaterial-vapor interface. At first sight, it seems a surprising result because the mean-field approximation washes out the surface plasmon (surface plasmons) modes which give a large contribution to the electromagnetic field at the vicinity of the metamaterial-vapor interface. Since the selective reflection signal comes from atoms located within a short distance k_d^{-1} from the interface, we would expect large contribution of the surface plasmons field to the selective reflection signal as well. Moreover, the surface plasmons modes are localized around the nano-slits which favor strong electric field gradient for larger coupling to the quadrupole transition. However, as shown in Figure 7.5, the surface plasmons modes are characterized by large wavevector parallel to the metamaterial-vapor interface. Thus, their contribution to the atomic response is Doppler broadened which results in a moderated global offset of the selective reflection signal, difficult to observe in the experiment (See Section 7.7). Therefore, only the propagating mode, which is normal to the interface, contributes to the selective reflection signal. This propagating mode corresponds also to the far-field contribution of the metamaterial, and it remains unchanged in the mean-field approximation. It explains why the mean-field approximation gives the correct prediction for our experiments.

7.4 Atomic simulation at steady state

In the experiment, we scan the frequency of the 685 nm laser across the $6S_{1/2} \rightarrow 5D_{5/2}$ electric quadrupole transition and we probe the $6S_{1/2} \rightarrow 6P_{3/2}$ dipole transition by selective reflection (selective reflection) spectroscopy on the surface of metamaterial with a 852 nm laser. More precisely, the 852 nm laser is locked onto the $F = 4 \rightarrow F' = 5$ hyperfine transitions and the 685 nm laser is scanned across the $F = 4 \rightarrow F'' = 6$ hyperfine transitions. Both lasers are co-propagating in the same direction. The pump - probe levels schematic is shown in Figure 7.1(a). In this section, we show that the contribution to the probe signal is given by the depopulation of the ground state and present

the optical Bloch equations for the electric quadrupole transition coupling. Subsequently, in Sections 7.5 and 7.6, we explore the depopulation effect of the ground state and the modulation on selective reflection probe signal by the quadrupole transition on a system of hot atomic vapor tranversing parallel to the metamaterial surface by decomposing the standing plasmon near field into Fourier components and solving for optical Bloch equations.

7.4.1 Coherence of the 3-levels system

In this subsection, we show that the coherent effect is limited by the relatively short relaxation time of $6P_{3/2} \rightarrow 6S_{1/2}$ transition, and the effect on selective reflection coherence is purely due to depopulation effect on the shared ground states between the dipole and quadrupole transitions.

We use the Bloch equations of 3 level atomic vapor system that have been studied extensively by Ducloy, Leite and Feld [110]. To simplify the calculation, we ignore the hyperfine and magnetic sublevels of the atomic state and assume a simple 3-levels V type system, which is sufficient to understand the coherence and population dynamics on the system.

Illustrated in Figure 7.4(b), we denote the ground state $6S_{1/2}$ by subscript $\underline{0}$, the probe excited state by subscript $\underline{1}$ and the pump excited state by subscript $\underline{2}$. The coherence of the 852 nm, $6S_{1/2} \rightarrow 6D_{3/2}$ transition, labeled as σ_{01}, which gives the selective reflection probe signal in Equation (7.1), is affected by three processes, 1) coherent effect via coupling of σ_{12} with Rabi frequency Ω_2, 2) decay channel through the $5D_{5/2} \rightarrow 6P_{3/2} \rightarrow 6S_{1/2}$ and 3) depopulation of the shared ground state σ_{00}.

The optical Bloch equations in the rotating wave approximation leads to:

$$\begin{aligned}
\dot{\sigma_{00}} - \gamma_1\sigma_{11} - \gamma_2\sigma_{22} &= -\frac{1}{2}i\Omega_1(\sigma_{01} - \sigma_{01}^*) \\
&\quad - \frac{1}{2}i\Omega_2(\sigma_{02} - \sigma_{02}^*) \\
\dot{\sigma_{11}} + \gamma_1\sigma_{11} - \gamma_2\sigma_{22} &= \frac{1}{2}i\Omega_1(\sigma_{01} - \sigma_{01}^*) \\
\dot{\sigma_{22}} + \gamma_2\sigma_{22} &= \frac{1}{2}i\Omega_2(\sigma_{02} - \sigma_{02}^*)
\end{aligned} \tag{7.5}$$

$$\begin{aligned}
\dot{\sigma_{01}} + L_1\sigma_{01} &= \frac{1}{2}i\Omega_1(\sigma_{11} - \sigma_{00}) + \frac{1}{2}i\Omega_2\dot{\sigma_{21}} \\
\dot{\sigma_{02}} + L_2\sigma_{02} &= \frac{1}{2}i\Omega_2(\sigma_{22} - \sigma_{00}) + \frac{1}{2}i\Omega_1\sigma_{21} \\
\dot{\sigma_{21}} + L_{21}^*\sigma_{21} &= -\frac{1}{2}i\Omega_1\sigma_{02} - \frac{1}{2}i\Omega_2\sigma_{01}^*
\end{aligned} \tag{7.6}$$

where $\dot{\sigma_{ij}} = d\sigma_{ij}/dt$,

$$\begin{aligned}
L_1 &= \gamma_{01} + i(\delta_1 - k_1 v) \\
L_2 &= \gamma_{02} + i(\delta_2 - k_2 v) \\
L_{21} &= \gamma_{21} + i[\delta_2 - \delta_1 - (k_2 - k_1)v]
\end{aligned} \tag{7.7}$$

In Equations (7.5) to (7.7), Ω_1 and Ω_2 are Rabi frequencies of probe and pump respectively. γ_i is the spontaneous emission rate and $\gamma_{ij} = (\gamma_i + \gamma_j)/2$ is the coherence relaxation rate, δ_i is the corresponding detuning, k_i is the wavevector of states i, j respectively, v is the atomic velocity.

Under the weak probe limit ($\Omega_1 \ll \gamma_{ij}$), the solution to Equations (7.5) and (7.6) can be expanded in zeroth and first series expansions of σ_{ij} with respect to Ω_1.

The zero-order solutions correspond to $\Omega_1 = 0$, where the probe field is absent and $\sigma_{11}^{(0)} = \sigma_{01}^{(0)} = \sigma_{21}^{(0)} = 0$. The steady state solutions $\dot{\sigma_{ij}}^{(0)} = 0$ on the pump are

$$\sigma_{02}^{(0)} = \frac{\Omega_2}{2}\frac{\delta_2 + i\gamma_2/2}{(\delta_2 - k_2 v)^2 + \Omega_2^2/2 + \gamma_2^2/4} \tag{7.8}$$

$$\sigma_{22}^{(0)} = \frac{\Omega_2^2}{4\big((\delta_2 - k_2 v)^2 + \Omega_2^2/2 + \gamma_2^2/4\big)} \tag{7.9}$$

which are the steady state solutions for a two-level atomic system.

The first-order solution with $\Omega_1 \neq 0$, is sufficient to induce coherence on the probe transition $\sigma_{01}^{(1)}$ but not sufficient to induce population change on the the probe excited state $\sigma_{11}^{(1)}$.

The first order expansion solutions are driven by pump depopulation $\sigma_{22}^{(0)}$ and pump coherence $\sigma_{02}^{(0)}$. The steady state equations are

$$L_1\sigma_{01}^{(1)} = \frac{1}{2}i\Omega_1(\sigma_{11}^{(0)} - \sigma_{00}^{(0)}) + \frac{1}{2}i\Omega_2\sigma_{21}^{*(1)} \tag{7.10a}$$

$$L_{21}^*\sigma_{21}^{(1)} = -\frac{1}{2}i\Omega_1\sigma_{02}^{(0)} - \frac{1}{2}i\Omega_2\sigma_{01}^{*(1)} \tag{7.10b}$$

The first term on the right-hand-side of Equation (7.10a) describes the response of the probe field to the depopulation on ground state by the pump and is independent of the coherences. The second term describes the response due to the coherences of the 3-level system.

The steady state values may be obtained by substituting the pump coherence and population from Equations (7.8) and (7.9) into Equation (7.10). Optical detunings and atom velocity are assumed to be zero for illustration purpose. The solutions then are

$$\begin{aligned}\sigma_{01}^{(1)} = \Omega_1\Big(&- \Omega_2^3\sigma_{02}^{(0)} + 2i\sigma_{00}^{(0)}L_2(\Omega_2^2 + 4L_{21}L_1^*) \\ &+ 4\Omega_2 L_1^* L_{21}^* \sigma_{02}^{*(0)}\Big) \Big/ \Big(\Omega_2^4 - 16|L_1|^2|L_{21}|^2\Big) \qquad (7.11)\\ \sigma_{21}^{(1)} = \Omega_1\Big(&\Omega_2^3\sigma_{00}^{(0)} + L_1^*(-2i\Omega_2^2\sigma_{02}^{*(0)} + 4\Omega_2 L_{21}\sigma_{00}^{(0)} \\ &+ 8iL_1L_{21}\sigma_{02}^{(0)}\Big) \Big/ \Big(\Omega_2^4 - 16|L_1|^2|L_{21}|^2\Big) \qquad (7.12)\end{aligned}$$

In this first order solution, it is assumed that the probe beam is weak enough such that the population is not modified by the probe. Solution in Equation (7.11) shows that in our cesium 3-levels transition, the increases in coherence with pump intensity depends mostly on the depopulation of ground state. This is because the coherence is largely washed out by the strong coherence relaxation from $5D_{5/2}$ to $6P_{3/2}$ given by an average of the lifetimes of the decay channel, which is 2.6 MHz compared to the long lifetime of the depopulation by σ_{02} which is 0.1 MHz. This ground state depopulation versus coherence dominating behavior is shown in Figure 7.4. In the figure, modification on the probe due to depopulation only (black, dotted curve) is $\sigma_{01} = 2i\Omega_1^{(0)}\sigma_{00}L_2/(\Omega_2^2 - 4L_1L_{21}^*)$ and the blue, solid curve is plotted using Equation (7.11). This diminished coherence effect is in contrast with the inverted V 3-levels system, at which coherence effect is dominant because of the similar lifetimes between the different transitions [45].

7.4.2 Depopulation of the 685nm pump

We show in Section 7.4.1 that the major contribution to the probe excitation comes from the ground state pump depopulation. In this section, the general optical excitation formula for a $L = 0$ to $L = 2$ electric quadrupole transition and only the final depopulation at steady state expression is considered. The excitations of the fine and hyperfine structures could easily be calculated using

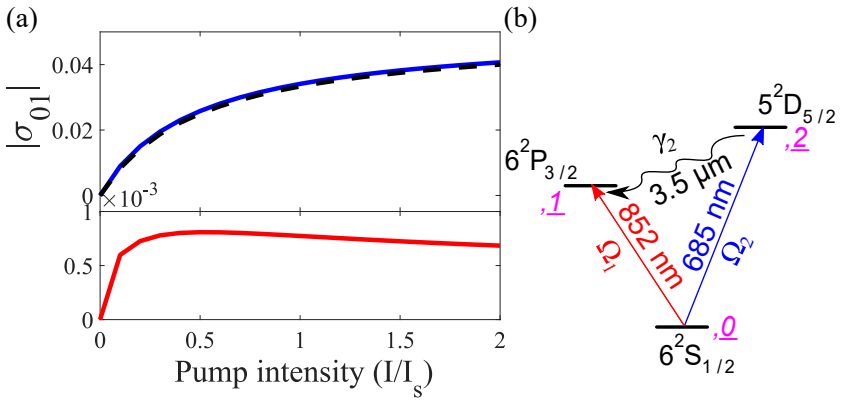

Figure 7.4: (a) Increase in $|\sigma_{01}|$ with pump intensity for depopulation contribution (black, dotted) and both depopulation and coherency coupling (blue, solid). I_s is the saturation intensity of the pump. The probe intensity assumed is a hundredth of probe saturation intensity. The bottom curve in red shows the difference between the black and blue curve. The difference between the two is less than 1%. (b) Energy levels of the 3 levels system. Numbering in magenta at each energy levels corresponds to the respective subscript labels in the optical Bloch equations.

the Wigner-Eckart theorem but the our aim is to have a general understanding of the coupling between the atomic vapor and the plasmon modes. For this purpose taking $L = 0$ to $L = 2$ transition is sufficient. It is assumed in this section onwards that all atomic parameters are referring to the electric quadrupole transitions.

The solutions of the optical excitation on the atomic states is given in terms of the density matrix by the optical Bloch equation,

$$\dot{\hat{\sigma}} = \frac{1}{i\hbar}[\hat{H}, \hat{\sigma}] + \dot{\sigma_{vac}^{\wedge}} \tag{7.13}$$

$\hat{H} = -e\boldsymbol{Q} : \boldsymbol{\nabla E}$ is the Hamiltonian of the electric quadrupole optical coupling, $\hat{\sigma}$ is the density matrix and $\dot{\sigma_{vac}^{\wedge}}$ is the decoherence matrix. The matrix elements of Equation (7.13) are the followings:

$$\begin{aligned}
H_{ii} &= \hbar\delta \\
H_{ij} &= \hbar\Omega_{ij} \ , \ i \neq j \\
\dot{\sigma_{vac_{ii}}} &= -\hbar\gamma\sigma_{ii} \\
\dot{\sigma_{vac_{ij}}} &= -\hbar\gamma\sigma_{ij} \ , i \neq j \ \& \ i \neq 0 \\
\dot{\sigma_{vac_{00}}} &= -\hbar\gamma \sum_{ii} \sigma_{ii} \ , \ i \neq 0 \\
\dot{\sigma_{vac_{i0}}} &= -\hbar\gamma\sigma_{i0}/2 \ , \ i \neq 0
\end{aligned} \tag{7.14}$$

γ is the spontaneous emission rate from $L = 2$ to $L = 0$ state, δ is the laser detuning. In Equation (7.14), the first and second equations define the diagonal and off-diagonal elements of the electric quadrupole Hamiltonian; the third and fifth equations define the diagonal elements of the decoherence matrix; the fourth and ixth equations define the off-diagonal elements of the decoherence matrix. Ω_{ij} is the Rabi frequency of the states i, j which for $L = 0 - L = 2$ transition is expressed as:

$$\Omega_{2m_l'} = \mathrm{C}\langle Y_{2m_l'}|\frac{\boldsymbol{Q}}{r^2}|Y_{00}\rangle : \boldsymbol{\nabla E} \tag{7.15}$$

where $Y_{2m_l'}$ is the spherical harmonics component of the atom wavefunction, $\boldsymbol{Q}/r^2$ is the quadrupole operator, : is the double dot product and $\boldsymbol{\nabla E}$ is the Jacobian of the electric field. C is a constant that contains the radial part of the wavefunction which does not interact with the electric quadrupole Hamiltonian. Subscript $2, m_l$ are the azimuthal, magnetic numbers of the

$L = 2$ excited state respectively, Subscript 00 denotes the ground state quantum number.

We solve the optical Bloch equations in Equation (7.14) with electric quadrupole Rabi excitation defined in Equation (7.15). In Sections 7.5 and 7.6, the optical Bloch solutions over our metamaterial surface is given.

7.4.3 Electric field parameters for the simulation

The local Jacobian of electric field, $\nabla \boldsymbol{E}(z)$is imported from Comsol (Femlab) simulation of silver plasmonic structures, corresponding to the structures used in our experiment. The simulate of the structures consists infinite 2D period of slits on silver layer. The thickness of the silver is 50 nm. On top of the silver is 8 nm of silicon dioxide layer. Below the silver is 1 µm thick of silicon dioxide substrate. The slits are 129 nm in length and 90 nm in width with a periodicity of 283.8 nm, this correspond to a plasmonic resonance peak of $\lambda_p = 685.2\,\text{nm}$. Monochromatic light with intensity of $1.3 \times 10^{-17}\,\text{mWcm}^{-2}$, much lower that the saturation intensity of Cs $6\text{S}_{1/2} \rightarrow 5\text{D}_{5/2}$ transition ($I_s = \frac{2\pi^2}{3\lambda^3}\hbar c \frac{{\gamma_{5D}^{\text{se}}}^2}{\gamma_{5D-6S}} \sim 2\ \text{Wcm}^{-2}$, where $\gamma_{5D}^{\text{se}} = 2\pi \cdot 124\,\text{kHz}$ is the fluorescence rate of $5^2D_{5/2}$ state) is normally incident on the structure.

7.5 Steady state solutions using Fourier expansion

In this section, we decompose the electric fields into its Fourier components and using assumption of weak field limit, we sum up the contributions of the field components to the depopulation of ground state independently. Such a treatment is valid as long as the Rabi frequency is much smaller than the linewidth of the transition.

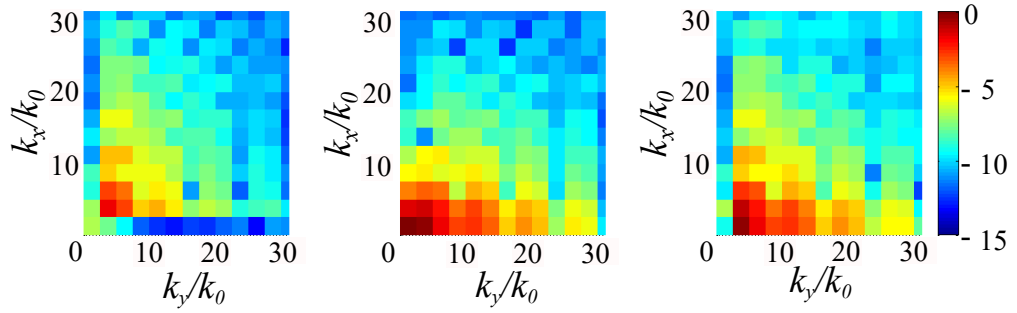

Figure 7.5: Two-dimensional Fourier transform of the three components of the electric field, in logarithmic scale. The left (resp. middle, and right) panel represents the $\tilde{E}_x$ (resp. $\tilde{E}_y$, and $\tilde{E}_z$) Fourier component of the electric field. The surface plasmons field is characterized by wavenumber larger than k_0 the free space wavenumber. The propagation field corresponds to the origin of the $\tilde{E}_y$ component.

7.5.1 Fourier components of the quadrupole factor

Considering a metamaterial located at the $z = 0$, the electromagnetic-field takes the following form, for $z > 0$ (in the atomic vapor):

$$\vec{E}(x,y,z) = E_0 \cos(k_0 z - \omega t)\hat{y} + \sum_{p,q\neq 0,0} \vec{E}^{(p,q)}(z) \times \mathrm{e}^{-i(pk_x^{sf}x-\omega t+\phi_n)}\mathrm{e}^{-i(qk_y^{sf}y-\omega t+\phi_m)}. \tag{7.16}$$

The first right-hand side term in Eq. (7.16) corresponds to the propagating transmitted field. This field is polarized along y-axis as the incident field. The second term is due to the surface plasmons waves. The components $\vec{E}^{(p,q)}(z)$ exponentially decay with a characteristic reciprocal length given by $k_{p,q} = k^{sf}\sqrt{p^2+q^2}$. The metamaterial is composed of a periodic array of nano-slits, so the wave-number of the fundamental modes of the surface plasmons wave is $k^{sf} = 2\pi/\Lambda$, where $\Lambda = 284\,\mathrm{nm}$ is the length of the square unitary cell. Moreover, the surface plasmons waves are stationary, thus $\vec{E}^{(p,q)}(z) = \vec{E}^{(-p,-q)}(z)$. The Fourier components of the surface plasmons field extracted from Comsol simulation is shown in Figure 7.5.

Fourier theorem dictates that $\boldsymbol{\nabla E}$ is equivalent to the integral of the fourier components of the electric field gradient along the xy surface. Since

∇E is periodic and varies within each unit cell, finite Fourier series is needed to capture the information of the electric field. In discrete Fourier series,

$$\boldsymbol{\nabla E} = -k_0 E_0 \sin(k_0 z - \omega t)\hat{y} - \sum_{p,q\neq 0,0} \boldsymbol{\nabla E}^{(p,q)}(z) \times \mathrm{e}^{-i(pk_x^{sf}x - \omega t + \phi_n)} \mathrm{e}^{-i(qk_y^{sf}y - \omega t + \phi_m)} \tag{7.17}$$

Both the gradient of the propagating field and surface plasmons field are contained in the summation. p and q are the indices of the Fourier components in x and y axes respectively.

Following the definition of Rabi frequency in Equation (7.15), the square of Rabi frequency for one angular momentum, m_l' is written in indices notation

$$\Omega_{2m_l'}^2 = |\langle Y_{2m_l'}|\frac{\boldsymbol{Q}}{r^2}|Y_{00}\rangle : \boldsymbol{\nabla E}|^2 = \Omega_{0_{2m_l'}}^2 + \sum_{pq}\sum_{p'q'}\sum_{ij}\sum_{i'j'} Q_{ji}^{2m_l'} Q_{j'i'}^{*2m_l'} \left(\frac{dE_i}{dx_j}\right)_{pq} \left(\frac{dE_{i'}}{dx_{j'}}\right)^*_{p'q'} \times \mathrm{e}^{-\mathrm{i}pk_x^{sf}x} \mathrm{e}^{\mathrm{i}p'k_x^{sf}x} \mathrm{e}^{-\mathrm{i}qk_y^{sf}y} \mathrm{e}^{\mathrm{i}q'k_y^{sf}y} \tag{7.18}$$

i, j denote summation over the Cartesian axes of the Jacobian. $\Omega_{0_{2m_l'}}^2 = k_0^2 Q_{zy}^{2m_l'^2} E_0^2 \cos(k_0 z - \omega t)^2$ is the Rabi frequency from coupling with propagating field, $Q_{ji}^{2m_l'}$ is the matrix element for the quadrupole operator in cartesian direction i, j. The double summation over p, q and i, j arises from taking the absolute amplitude square on the Rabi frequency.

The mean response of the atom along the surface $\bar{\Omega}_{2m_l'}^2$ is the integral of $\Omega_{2m_l'}^2$ over the unit cell area A:

$$\bar{\Omega}_{2m_l'}^2 = \iint_A \Omega_{2m_l'}^2 dxdy = \Omega_{0_{2m_l'}}^2 \tag{7.19}$$

$$+ \sum_{pq}\sum_{p'q'}\sum_{ij}\sum_{i'j'} pp'qq' Q_{ji}^{2m_l'} Q_{j'i'}^{*2m_l'} \left(\frac{dE_i}{dx_j}\right)_{pq} \left(\frac{dE_{i'}}{dx_{j'}}\right)^*_{p'q'} \delta_{pp'}\delta_{qq'}$$

$$= \sum_{pq}\sum_{ij}\sum_{i'j'} p^2 q^2 Q_{ji}^{2m_l'} Q_{j'i'}^{*2m_l'} \left(\frac{dE_i}{dx_j}\right)_{pq} \left(\frac{dE_{i'}}{dx_{j'}}\right)^*_{pq} \tag{7.20}$$

Dirac delta functions $\delta_{p,p'}$ and $\delta_{q,q'}$ apply because of the orthogonality of Fourier components. This simplifies the summation indices p, q, p', q' over k_x and k_y components.

Next, we calculate the steady state excited state populations. In the simpler case of two levels system, from Equation (7.9), in a weak field limit ($\Omega_2 \ll \gamma_2$) wherein the ground state population is weakly depleted by the pump, the excited state population can be approximated to be

$$\sigma_{22} = \frac{\Omega_2^2}{4(\delta - kv)^2 + \gamma^2} \tag{7.21}$$

and the ground state population Π_g is,

$$\Pi_g = 1 - \sigma_{22} \tag{7.22}$$

In this regime, the response is linear with respect to the Ω_2^2.

For $L = 0 \rightarrow L = 2$ states, we have contributions from $m_l' = 0, \pm 1, \pm 2$, the excited population $\sigma_{2m_l'}$ of m_l' state for an an atom with velocity $\boldsymbol{v}$ is,

$$\sigma_{2m_l'}(\boldsymbol{v}) = \frac{\Omega_{0_{2m_l'}}^2}{4\delta^2 + \gamma^2} + \sum_{p,q \neq 0,0} \frac{\Omega_{2m_l'}^2(p,q)}{4(\delta - pk_x^{sf} v_x - qk_y^{sf} v_y)^2 + \gamma^2} \tag{7.23}$$

where $\Omega_{2m_l'}^2(p,q)$ is defined in Equation (7.18) and the ground state population depletion is summed over all excited states in the weak field limit,

$$\Pi_g(\boldsymbol{v}) = 1 - \sum_{m_l'} \sigma_{2m_l'}(\boldsymbol{v}) \tag{7.24}$$

To check the validity of the expression Equation (7.19), we calculate the mean Rabi frequency $\bar{\Omega}_{2m_l'}^2$ twice; once by spatial integration from Equation (7.18) and another by integration in Fourier space from Equation (7.19). Both Rabi frequencies are substituted into Equation (7.24) for the case of atoms with zero temperature $\boldsymbol{v} = 0$ in the near field of metamaterial. Both methods give the same ground population. The results are shown in Figure 7.6.

We observe a six order of magnitude enhancement on the electric quadrupole transition by coupling with the near-field of our metamaterials between atoms with $\boldsymbol{v} = 0$ at $z = 0.02\lambda$ and atoms in free space . Figure 7.7 illustrates the magnitude of enhancement for atoms with $\boldsymbol{v} = 0$ calculated with Equation (7.24).

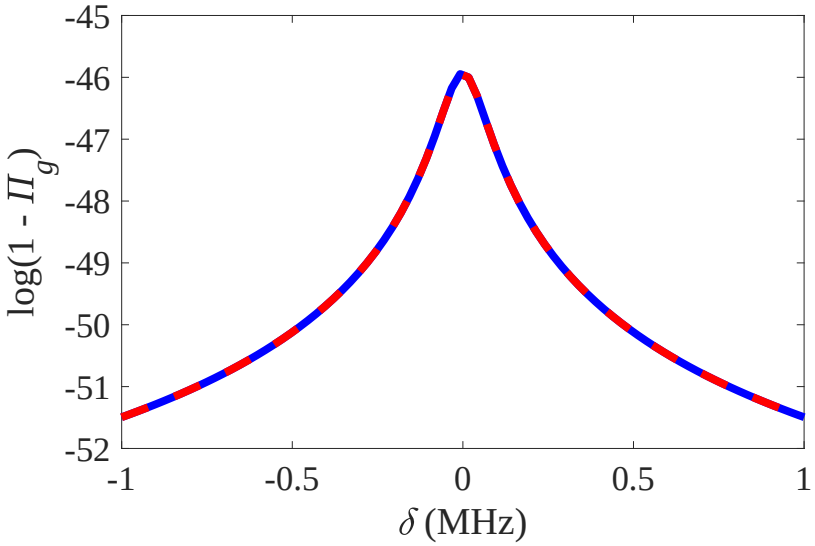

Figure 7.6: Red, dotted line is calculated from an 2D spatial average of the Rabi frequency along the metamaterial surface (Equation (7.18) in Equation (7.24)) and blue, solid line is calculated from summation of Rabi frequencies in k space (Equation (7.19) in Equation (7.23). Distance of the atoms from the metamaterial surface is $0.02\,\lambda$, $\lambda = 685\,\text{nm}$. Both methods show the same depopulation Π_g value.

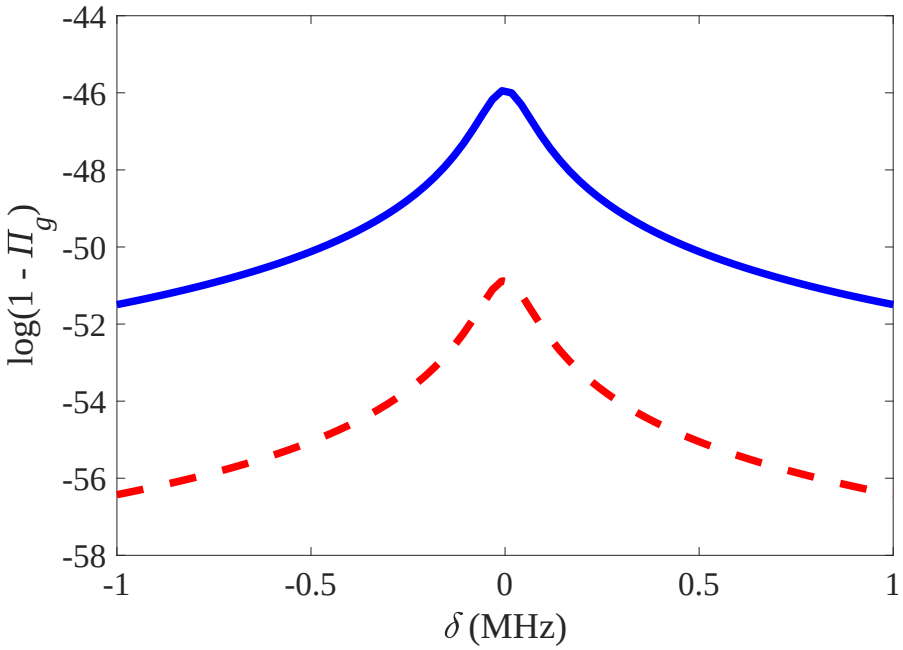

Figure 7.7: Blue, solid curve is the depopulation of ground state for atoms at $z = 0.02\,\lambda$, $\lambda = 685\,\text{nm}$. Red, dotted line is the depopulation of ground state for atoms at $z = 3.56\,\lambda$ where the near field evasnescence is negligible.

7.5.2 Simulation of thermal averaged atoms

In this subsection, we will take into account the velocity distributions of our ensemble of hot atoms in our calculations.

The mean ground population of the atom at a finite temperature is

$$\begin{aligned}\Pi_g &= 1 - \bar{\sigma}_{22} \\ &= 1 - \frac{\Omega_0^2}{4\delta^2 + \gamma^2} \\ &- \frac{1}{2\pi\bar{u}^2} \iint_0^\infty dv_x dv_y \mathrm{e}^{-\frac{v_x^2+v_y^2}{2\bar{u}^2}} \\ &\times \sum_{m_l'} \sigma_{2m_l'}(\boldsymbol{v})\end{aligned} \tag{7.25}$$

where the velocity dependent excited state population $\sigma_{2m_l'}(\boldsymbol{v})$ is defined in Equation (7.23). The double integration averages the contributions from thermal atoms with velocities v_x and v_y parallel to the surface. The z component velocity, v_z is ignored here because selective reflection technique on the probe in our experiment only detects atoms flying parallel to the surface.

In our experiment on top of metamaterial, the Doppler width is much larger than the natural linewidth. In this limit, the Lorentzian profile can be approximated as a dirac delta function in the integral of Equation (7.25) and the equation is simplified as

$$\Pi_g \simeq 1 - \frac{\Omega_0^2}{4\delta^2 + \gamma^2} - \sqrt{\frac{\pi}{2}} \frac{1}{2\gamma\bar{v}} \sum_{p,q\neq 0,0} \frac{\Omega_{2m_l'}^2(p,q)}{k_{p,q}} \mathrm{e}^{(} - \frac{\delta^2}{2k_{p,q}^2\bar{v}^2}) \tag{7.26}$$

where $k_{p,q} = \sqrt{pk_x^{sf^2} + qk_y^{sf^2}}$ is the amplitude of the wavevector.

Equation (7.26) gives the average response of thermal distributed atoms. The ground state population at $z = 12\,\mathrm{nm} = 0.02\,\lambda$ is calculated and shown in Figure 7.8(a). The central peak with full-width-half-maximum (FWHM) of $\gamma = 2\pi.124\,\mathrm{kHz}$, comes from the propagating electric field and is independent of the vertical position of the atoms. This can be seen by the same amplitude of central peak in the near field and farfield in Figure 7.8(a) and (b). The high $k_{p,q}$ components of near field electric fields, results in a large Doppler

broadened background. A fit to a Gaussian profile suggests the FWHM width to be 1.7 GHz at $T = 90°\text{C}$. We do integration of the total population area under the spectrum for the $\boldsymbol{v} = 0$ and the thermal distribution case Figure 7.6 and Figure 7.8(a) and they are verified to be the same. This shows that the strong enhancement by localized fields are present (See Figure 7.7) but is spreaded out in the frequency space.

7.6 Comparison with optical Bloch evolution

Alternative method of obtaining the depopulation of thermal averaged atoms is to time evolve the ordinary differential equations in Equations (7.13) and (7.14) across the electric field of our metamaterial. We use it as a formal check of our previous approach. The density matrices of atoms for various velocities are set to evolve until the populations and coherences reach steady state values. A demonstrative example for the evolution to a steady state is shown for $v = 1\,\text{ms}^{-1}$ in Figure 7.9(b). The velocity-dependent density matrices are then integrated according to the Boltzmann distribution of velocities and the thermal average values of depopulation is calculated against laser detuning. In this section, we explain the steps taken for such a simulation.

7.6.1 Evolution of one atom tranversing across the metamaterial slits

An atom is set to travel through the middle of the slits (convention of the direction of travel is chosen as y) at a vertical distance of $z = 12\,\text{nm}$ with the surface, which corresponds to the same vertical distance of $z = 0.02\lambda$ in Figure 7.8. First, the local Rabi frequencies $\Omega^{eq}_{2m'_l}(y)$ are calculated with $\boldsymbol{\nabla E}(y)$ from Equation (7.15). Various velocities of the atoms from $5 \times 10^{-3}\,\text{ms}^{-1}$ to $900\,\text{ms}^{-1}$of the atom are taken to account for Doppler broadening. For each velocity v, the position of the atom y is now related to the velocity by $y = vt\%\Lambda$ where t is the time of evolution, Λ is the period of one unit cell and % denotes taking the remainder.

Optical Bloch equation is evaluated until it reaches a steady state. Figure 7.9 shows two such results for the optical Bloch evaluations. For demonstration purpose, we increase the intensity of the incident field for better contrast in the curves for ease of viewing. We could see that the atom has two different regimes of velocities; i.e. (a) adiabatic regime when the time

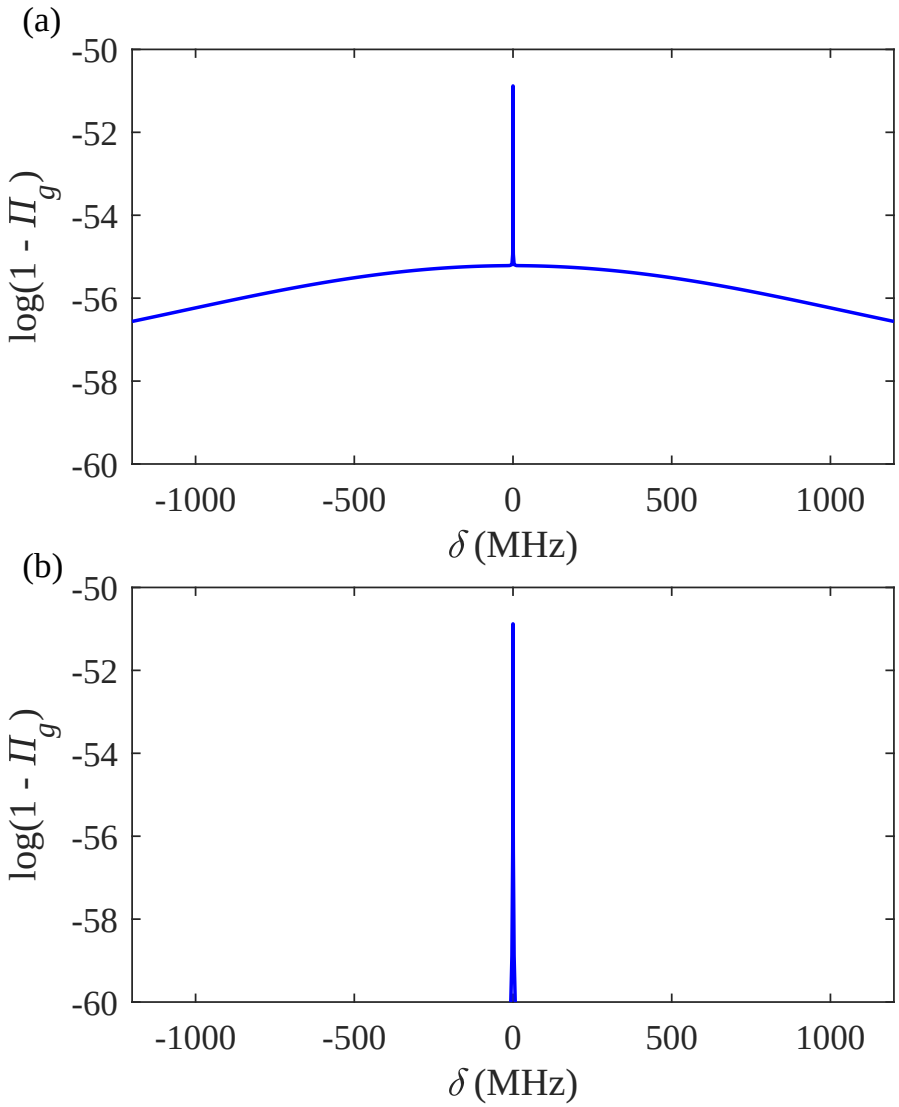

Figure 7.8: (a) Logarithmic plot of depopulation of ground state at $z = 0.02\lambda$. Central peak is a Lorentzian lineshape with linewidth γ and a Doppler broadened background of 1.7 GHz (Full width half-maximum). (b) Logarithmic plot of depopulation of ground state at $z = 3.56\lambda$. There is a central peak of the same magnitude with (a) but Doppler background is absent.

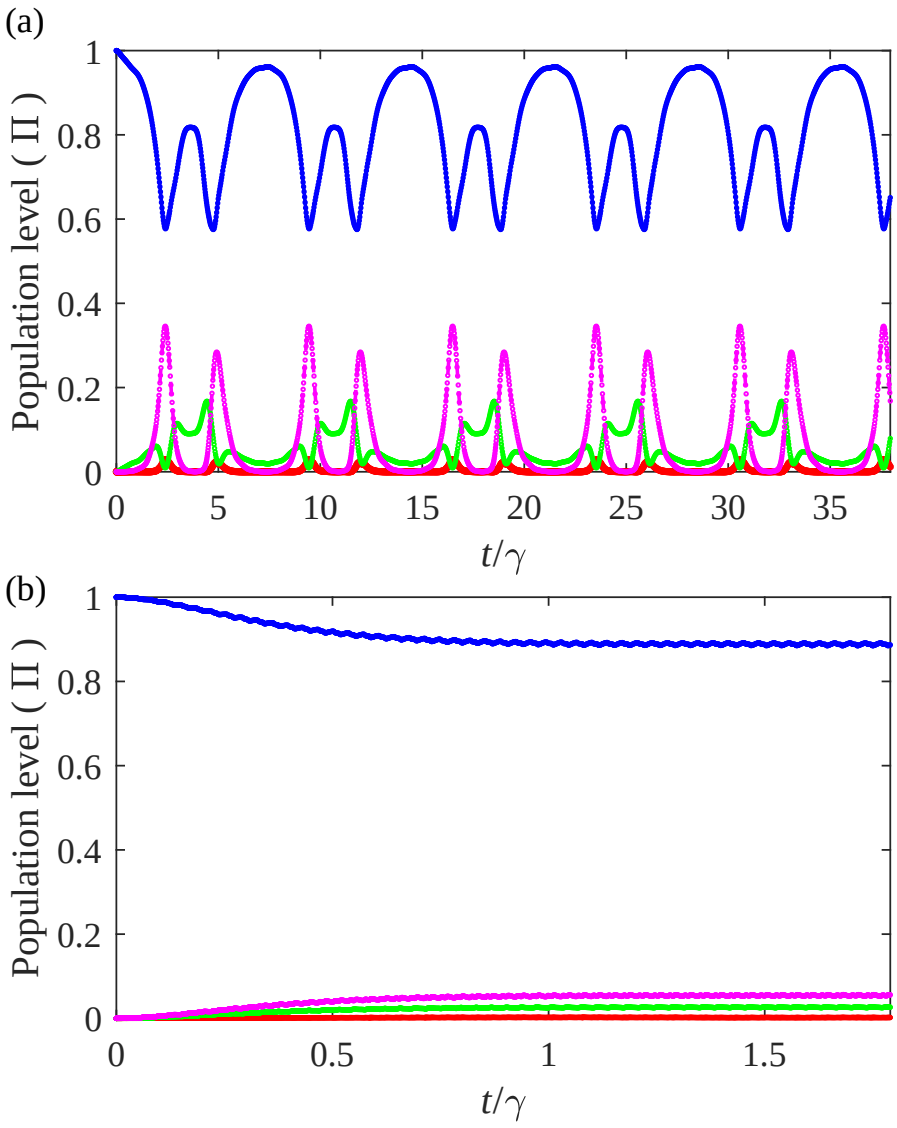

Figure 7.9: The evolution of the states population labeled In blue - $m_l = 0$; In magenta - $m_l' = 0$; In green - $m_l' = \pm 1$; In red - $m_l' = \pm 2$. (a) Adiabatic regime where each cycle corresponds to one unit cell. The speed of the atom is $v = 0.005\,\mathrm{ms}^{-1}$. Laser detuning $\delta = 0$ (b) Non-adiabatic regime where the the states are insensitive to the field change and reach equilibrium quickly. The plot corresponds to states where atoms have tranversed 8 cells. The speed of the atom is $v = 1\,\mathrm{ms}^{-1}$ and the detuning $\delta = k_d v$ where $k_d = 2\pi/\Lambda$ where Λ is the periodicity of one unit cell.

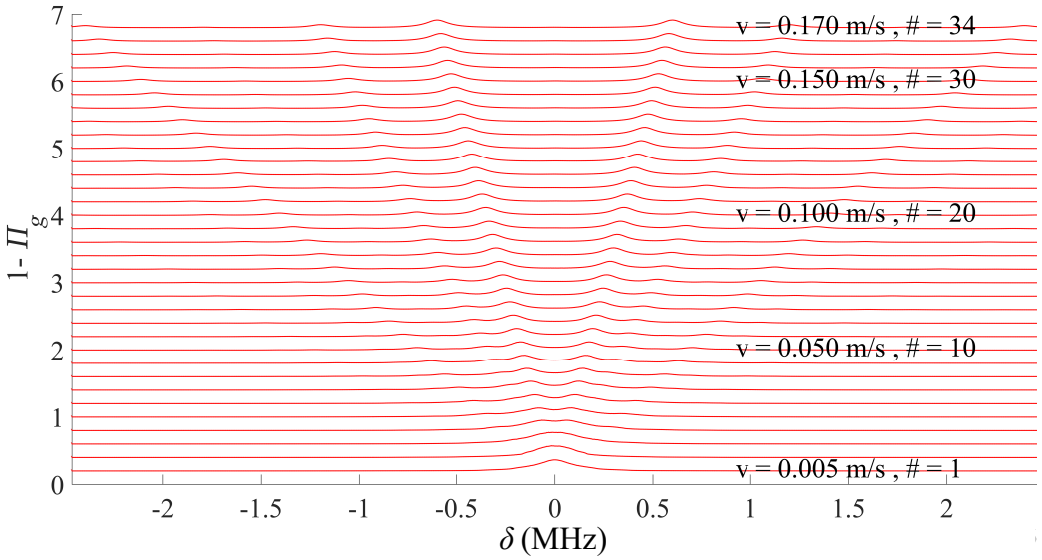

Figure 7.10: Plot of ground population depletion (inverted) versus laser detuning for slow velocities. Starting from bottomest curve to the top curve - $v = 0.005\,\mathrm{ms}^{-1}$ to $v = 0.170\,\mathrm{ms}^{-1}$ in a step of $0.005\,\mathrm{ms}^{-1}$. The velocity distribution that contributes to the zero detuning is very small; i.e. the depopulation on the first sideband is already 0.5 MHz away from the center for small $v = 0.170\,\mathrm{ms}^{-1}$.

period for one unit cell is much longer than the time constant of the transition and (b) non-adiabatic regime where the opposite is true. Adiabatic regime is the regime where the plasmonic mode is expected to give contribution to the electric quadrupole pump-electric dipole probe signal and thus most interesting to us. However, it is observed that the velocity group of atom that stays in adiabatic regime is very small. Figure 7.10 illustrates that only the atoms with $v \leq 0.005\text{ms}^{-1}$ would be in adiabatic regime and the velocity groups with $v > 0.005\text{ms}^{-1}$ would contribute to a Doppler broadened background.

7.6.2 Detuning scaling of high velocity atom ground population

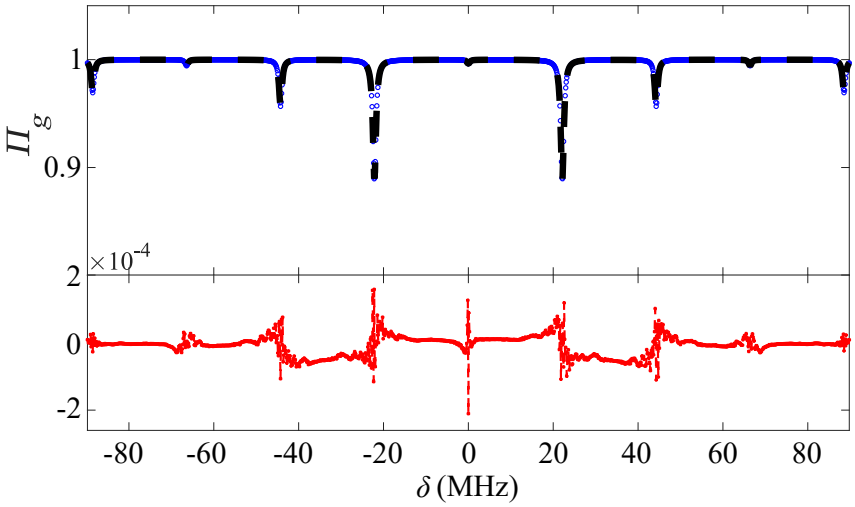

Figure 7.11: Plot of ground population depletion for $v = 1\,\text{ms}^{-1}$ case that is used as reference in the fit. There is a center dip with amplitude of 0.004 (150 times smaller than the first pair of sidebands) which is barely visible on the graph. The atomic velocity is $1\,\text{ms}^{-1}$.

At high velocity in the non-adiabatic regime, where frequencies of the first pair of sidebands are several magnitude larger than the linewidth, the response of the atom is not sensitive to local electric field gradient but is sensitive through Doppler effect to the speed at which it travels across each

unit cell. Thus there is merely translation of the frequencies of the sidebands at multiples of v/Λ, where v is the speed of the atom and Λ is the period of the unit cell and no change to the atomic linewidth. This allows us to take one non-adiabatic simulation and scale it according to the atom velocity. The computation of the optical Bloch equation thus only needs to be done once. First, Lorentzian fits of the first four sidebands for the ground population σ_{gg} are done on the lines for a nominal velocity $1\,\mathrm{ms}^{-1}$. The fit is good with around 10^{-4} in amplitude for the fit residue. The fifth sidebands onwards have less than 10^{-4} amplitude, low amplitude than the accuracy of the fit and are discarded. The sidebands and the fits are shown on Figure 7.11. The fitting parameters are then used to construct the spectrum of atom velocity that is more than $v_{\mathrm{cut\_off}} = 0.12\,\mathrm{ms}^{-1}$. For atom velocity that is below $v_{\mathrm{cut\_off}}$, the spectrum of the atom is calculated based on optical Bloch equation as explained in previous section. Scaling the frequency of sideband works well, which can be seen by low residues between the simulation data and scaled spectra on Figure 7.12.

7.6.3 Inhomogenous broadening from velocity distribution

In the same spirit with Equation (7.25) in the previous section, the Doppler broadening spectrum is given by

$$\Pi_g(\delta) = \int_0^\infty \frac{1}{\sqrt{2\pi}\bar{u}} \mathrm{e}^{-\frac{v^2}{2\bar{u}^2}} \sigma_{gg}(v,\delta)\mathrm{d}v \tag{7.27}$$

It is a numerical integral of two terms: The first term is the one-dimensional velocity distribution and; the second term is the ground population that was evaluated in Sections 7.6.1 and 7.6.2. In our simulation, the summation velocity interval Δv from $v = 0$ to $v = v_{\mathrm{cut\,off}}$ is finer at $0.005\,\mathrm{ms}^{-1}$ and coarser at $0.02\,\mathrm{ms}^{-1}$ from $v_{\mathrm{cut\,off}}$ to $v = 900\,\mathrm{ms}^{-1}$.

Red dashed curve in Figure 7.13 shows the ground population spectrum calculated for $T = 90°\mathrm{C}$. The Doppler broadening causes the depletion of the ground population at zero detuning to be about 70 times smaller than for a stationary atom.

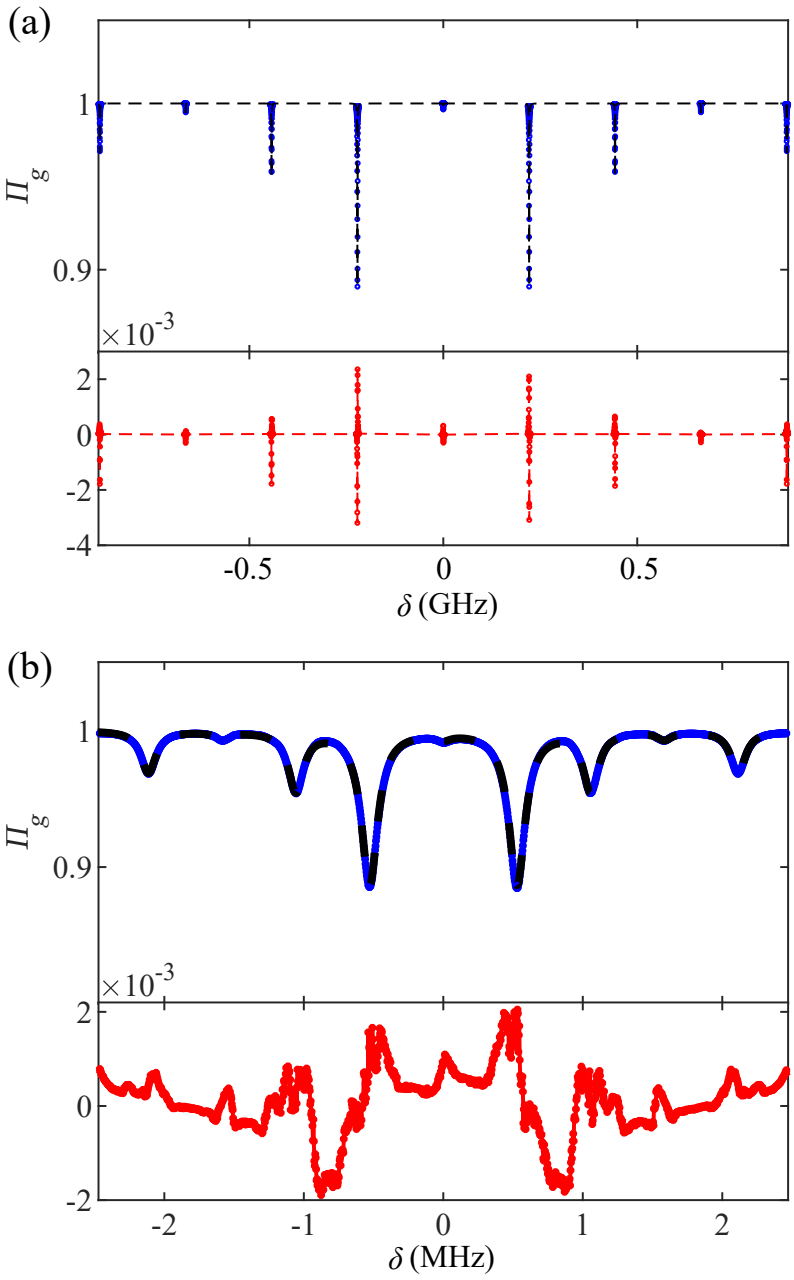

Figure 7.12: Simulation (blue circle) compared with scaled spectrum (black line) for (a) $v = 10\,\mathrm{ms}^{-1}$ and (b) $v = 0.15\,\mathrm{ms}^{-1}$. In both cases, the highest residues observed (in red) is only $\approx 2 \times 10^{-3}$.

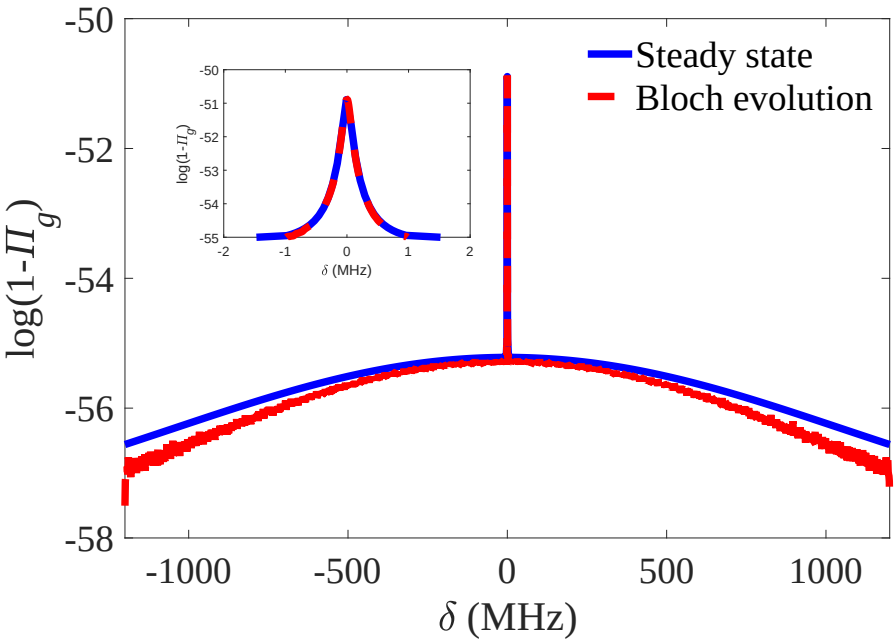

Figure 7.13: Logarithmic plot of depopulation of ground state at $z = 0.02\lambda$. The steady state solution obtained by Bloch evolution is plotted in red dotted line. Steady state solution considered in previous subsection is plotted in solid blue line (same data as Figure 7.8). Both simulations are done with the same incident electric field magnitude. The difference between the two curves at large detuning are likely because Bloch evolution is done on an 1 - dimensional cross-section of the surface but steady state solution is calculated on the whole 2 - dimensional surface. The inset shows the good agreement near zero detuning between the two approaches. The fluctuation in red curve are due to uncertainties/fluctuations when the evolution reaches steady states in Bloch evolution.

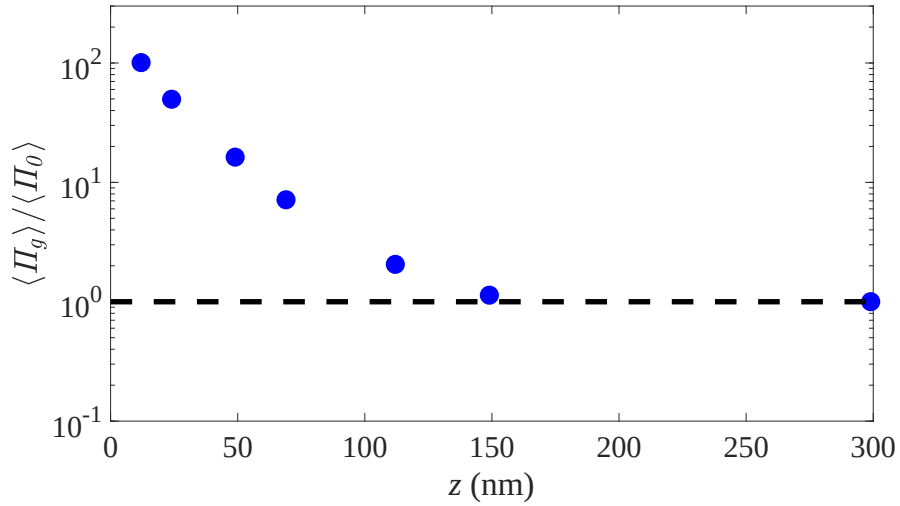

Figure 7.14: Enhancement of the ground state population depletion as function of the distance from the from the metamaterial-vapor interface. $\langle \Pi_g \rangle$ is the spectral averaged ground state population. $\langle \Pi_0 \rangle$ is the spectral averaged ground state population in vacuum.

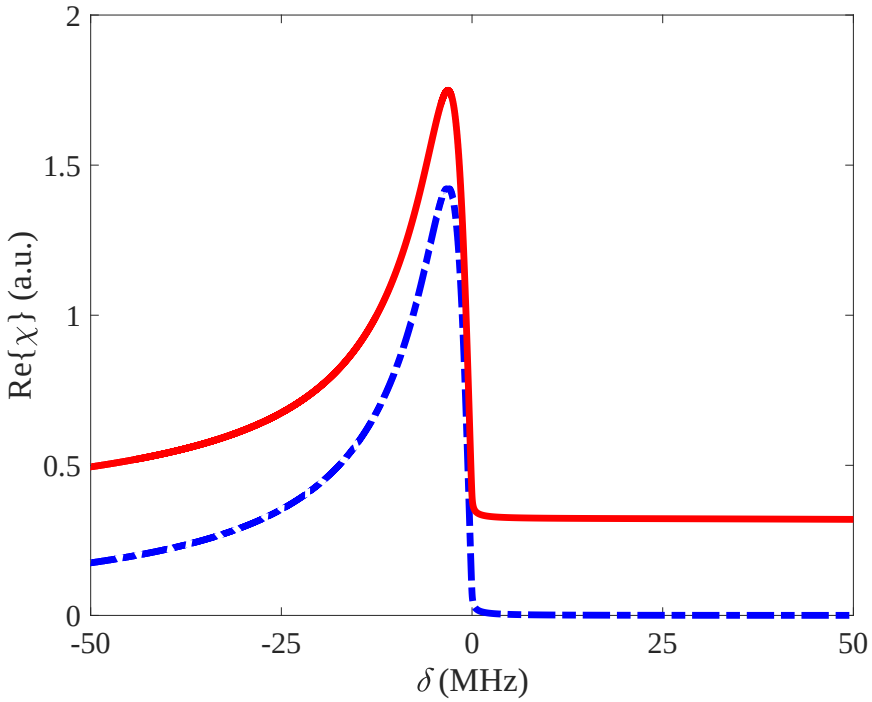

Figure 7.15: Real part of the effective susceptibility. The red (resp. dashed-dotted blue) curve includes (resp. excludes) surface plasmons.

7.7 Contribution of surface plasmons waves to the selective reflection signal

In Section 7.5, we assume a weak field limit and take a summation of all the contributions of the electric fields to the steady state solutions for an ensemble of hot atoms transversing on the 2D plasmonic surface. In Section 7.6, evolution of the optical Bloch ODE equations (Equations (7.13) and (7.14) until steady states are done on a 1D path on the plasmonic surface. Both results are shown in Figure 7.13 for the case of $z = 0.02\,\lambda$. The comparison shows that both methods are consistent. 2D simulations of the ODE were not used because of the long computation time needed.

As shown in Figure 7.13, the spectra are characterized by a narrow central peak with a z - independent amplitude confirming that it can be attributed to the Doppler-free propagating component of the light field. The surface plasmons field gives a Doppler broadened contribution of width $1.4 \times 10^4\,\gamma = 1.7\,\mathrm{GHz}$ (FWHM value). In our experiment, the selective reflection signal is roughly the averaged contribution of the atomic layers up to a distance of $z^{-1} = 135\,\mathrm{nm}$. The surface plasmons field decays rapidly with the distance z as it is illustrated on Figure 7.14, where we show the frequency integrated ground state depletion as function of the z. Nevertheless we observe large enhancement of the coupling if the atoms are located close enough to the interface.

To get a general idea of the surface plasmons contribution to the selective reflection signal, we plug the ground state depletion from the simulation into Equation (7.1) for $z = 70\,\mathrm{nm}$, the typical distance for selective reflection signal. We observe that the general shape of the effective susceptibility remains unchanged, and the surface plasmons field mainly contributes to an extra background (see Figure 7.15). The moderate offset, expected on the selective reflection signal, makes the observation surface plasmons field very difficult to isolated from other spurious sources of offset as the stray reflection of the pump laser.

7.8 Conclusion

We studied selective reflection spectroscopy of a weakly coupled electric quadrupole transition using a pump-probe spectroscopy method. Here the signal is probed on an electric dipole transition. We demonstrate in Section 7.3 that using a dielectric-vapor interface, the selective reflection signal is proportional to the susceptibility of an atom at rest for negative frequency and it drops to zero for positive frequency. The effective linewidth of the selective reflection signal is predicted to be the linewidth of the probe transition divides by a factor 0.8 corresponding to the probe and pump wavenumber ratio. On a dielectric-metamaterial-vapor interface, we observe similar selective reflection signal with a reduction of the overall signal amplitude. Here, the metamaterial is designed to have a plasmonic resonance at the vicinity of the pump frequency. The overall signal reduction is in good agreement with a mean-field model where the metamaterial is replaced by a homogenous material. The model indicates that the enhancement of the coupling of the electric quadrupole transition, due to large spatial variation of the surface plasmons field, is not observed on the selective reflection signal. Using a complete description of the electromagnetic field in Sections 7.5 and 7.6, we find that the surface plasmons waves contribute to a Doppler broadened signal which slightly offsets the selective reflection signal which is shown in Section 7.7. One way to remove the Doppler broadening would be to transversally cool the atomic vapor down to $\sim 5\,\mu\mathrm{ms}^{-1}$, corresponding to a Doppler broadening equals natural linewidth of the Cs $6\mathrm{S}^2_{1/2} - 6\mathrm{D}^2_{5/2}$ electric quadrupole transition of 124 kHz. In this case, a large increase in the quadrupole signal should be observed.

Chapter 8

Summary and Outlook

This final chapter highlights the main results presented in the previous chapters and a discussion of future work for the atom-metamaterial experiments.

In Chapter 4, we report on the modification of van der Waals ΔC_3 coefficient on Cesium atomic vapor between the states $6^2\mathrm{P}_{3/2}$ and $6^2\mathrm{S}_{1/2}$ for atoms coupled with the plasmonic resonance of metamaterial. The presence of imaginary ΔC_3 is due to additional non-radiative decay channels into the surface plasmon. Accompanied with the non-radiative decay is the observation of near-vanishing attractive van der Waals potential of the aforementioned energy levels. Our work is an experimental demonstration of tunability in the atom-surface interaction unrestrained by the availability of natural material, which would be useful in future atomic physics experiments near surfaces.

In Chapter 5, by performing selective reflection spectroscopy on a large transverse area multimode optical fiber with metamaterial on fiber tip, we observe a characteristic modification on the spectral lineshape due to the coupling of atomic transition with the surface. By fitting the spectrum with selective reflection theory, we extract the change in van der Waals ΔC_3 coefficient due to the metamaterial surface and demonstrate that active engineering of atom - surface interaction on optical fiber platform is possible.

In Chapter 6, we report on the first Doppler-free non-linear spectroscopy on an electric quadrupole transition. We resolve the hyperfine structures on the electric quadrupole transition by optical pumping on the transition and probing on another electric dipole transition on a three level system with linear polarizations. We show that for this V-type three level system and the probe laser locked on the electric dipole $6^2\mathrm{S}_{1/2}(F = 4) \rightarrow 6^2\mathrm{P}_{3/2}(F = 5)$ transition, the spectrum can be explained by the optical de-pumping and re-

pumping on the shared ground state hyperfine manifold with a fixed transition time relaxation rate, which resulted in an 'emission-like' spectrum. For a three level system with no shared ground state, the spectrum is governed by the optical re-pumping to the ground state of the electric dipole probe and resulted in an 'absorption-like' spectrum. In above two cases, the spectrum are polarization-independent and the relative line intensities can be modeled only depending on the hyperfine transitional strength factors of the electric dipole and electric quadrupole lines. For a probe laser exciting on the electric dipole $6^2S_{1/2}(F = 4) \rightarrow 6^2P_{3/2}(F = 4)$ transition, the spectrum depends on the relative polarization between the pump and the probe and we suggest that optical pumping between the magnetic sublevels need to be considered.

In Chapter 6, we observe an enhancement up to 2 order of magnitude on the electric quadrupole $Cs6^2S_{1/2} - 5^2D_{5/2}$ 685 nm transition due to excitation from localized surface plasmon in our theoretical calculations. Experimentally, we observe the coupling of the electric quadrupole transition with the metamaterial by modulating the 685 nm excitation laser on our metamaterial and detecting the modulated reflection on ground state population on an overlapping 852 nm beam. The Doppler-free signal detected is explained as a mixing of the absorptive and dispersive parts of the atomic suceptibility due to coupling of the electric quadrupole transition with metamaterials. Overall, the high thermal velocities of atom vapor mitigate the enhancement effect of metamaterials on the atomic transitions, because of the subwavelength localization of electric field on metamaterials. One straightforward method to counter the damping of enhancement would be to transversely cool the atoms, where we would expect to see an enhancement in our reflection spectrum. Another possibility is to investigate the surface enhancement effect in the Dicke regime, where the mean free path of the atoms is less than the wavelength of the atomic resonance. In this regime, the Doppler-broadened spectrum can be dramatically narrowed from frequent velocity-changing collisions [121, 122]. The strong enhancement effects that are dispersed over strong Doppler broadened signal could therefore possibly be observed on the strongly Dicke narrowed line.

At the closing of this chapter, we highlight a possible direction of our future work. One promising direction is the manipulation and imaging of single atom using a sub-wavelength super-oscillatory spot created by metamaterial [123]. Super-oscillation is termed as such because a band-limited function could locally oscillate faster than its highest Fourier component [124]. The concept of localizing cold atoms in sub-wavelength spots is first considered by

Balykin and coauthors [125] and subsequently investigated by few other groups [126, 127, 128] in evanescent wave . However, experimental realization of atom trap in the near-field evanescent wave requires overcoming techinical challenges such as heating up of cold atoms by thermal noise of the surface and adiabatic transfer of cold atoms to the nearfield structures. By trapping atom in the far-field, we have the benefits of overcoming these technical challenges. Quantum technologies applications such as single photon source and strong atom-light coupling has been reported [129, 130] but so far only with conventional imaging system which are diffraction limited. By trapping of atoms in sub-wavelength spots, we achieve better transverse spatial localization and better control of the atom position. This would result in better coupling efficiency of the atom with light for quantum technologies application. Another promising application is the imaging of a single atom with the sub-wavelength spot. This has application in single site resolution adrressing of atoms trapped in a two-dimensional lattices where interesting results such as quantum phase transitions, strongly correlated systems, and single spin addressing have been reported [131, 132, 133]. In the studies above, site addressing of atoms are performed with a microscope objective with a large numberical aperture (N.A. $= 0.7 - 0.8$) which has stringent requirements on the optical alignment and tolerances on the aberration-correction procedures. Short working distance of high numerical aperture objective is also a major experimental constraint in the system. Using sub-wavelength spot generated in the far-field from metamaterial, similar resolution with a lower numerical aperture and higher working distance is expected. This would greatly simplify the imaging system. Currently, we have built a magneto-optical trap that trap about 10^5 atoms in a volume of $0.01\,\mathrm{mm}^3$ at a temperature of $\simeq 50\,\mu\mathrm{K}$. The next step would be to transfer one atom from our cold atomic cloud into the sub-wavelength trap and characterizing trapping performance. Experiment such as resonant imaging on a single atom with a super-oscillatory beam is also planned.

Appendix A

Appendices

A.1 Data sets for Casimir Polder forces control on Cesium electric dipole transitions

The full span of refractive indices n' and factor $r_0^*\rho$ extracted from FDFD simulation and ΔC_3 coefficients from the spectra fit across the ten metamaterials are given in Table A.1. Factor $r_0^*\rho$ is computed from n' by using Equation (4.6) and ΔC_3 coefficients are fitted using Equations (4.2) to (4.6). Refractive index of dielectric window used in the fit is $n_d = 1.45$, corresponding to the refractive index of fused quartz window and the metamaterial thickness is taken to be 50 nm. $r_0^*\rho$ encapsulates the Fano resonance effect on the metamaterial as is explained in Chapters 2 and 4. The full span of the selective reflection spectrum of atoms across the ten metamaterials is shown in Figure A.1. Signals for plasmon resonance λ_p, far-detuned from the atomic transition, are considerably smaller than the spectra near coupled resonances because of the low transmission of the metamaterial at $\lambda = 852$ nm (see for example case $\lambda_p = 973$ nm in Figure A.1. From the fits to the data, we extract the complex value of the ΔC_3 coefficient shown in Figure 4.4 in Chapter 4.

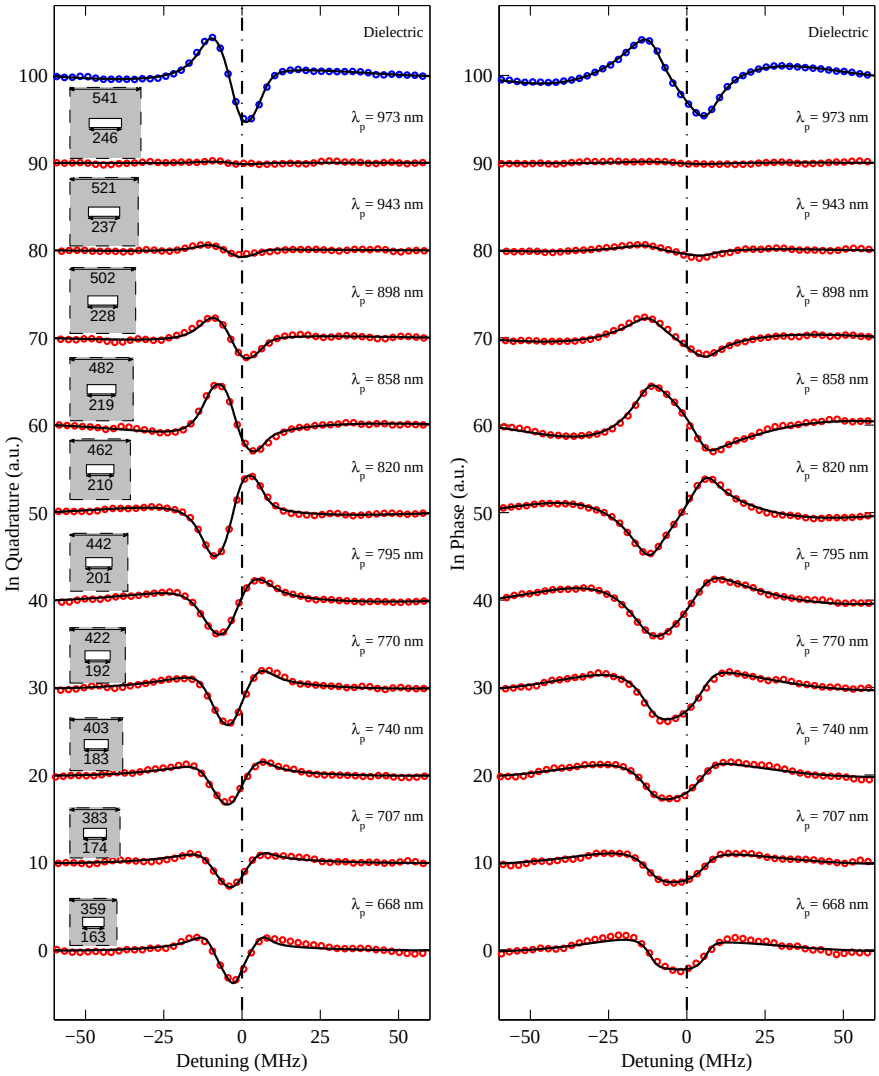

Figure A.1: Selective reflection spectra (both in-phase and in-quadrature) of the plain windows (blue dots at top curves) and of the ten metamaterials (red dots) with plasmon resonances in Table A.1. Black lines correspond to the fits to the data as explained in Section 4.3.3.

Table A.1: Table of parameters n', $r_0^*\rho$ and ΔC_3

#	Resonance λ (nm)	n'	$r_0^*\rho$	ΔC_3 (kHz µm^3)
1	973	0.4443 + 6.1613i	-0.0215 + 0.0130i	4.6597
2	943	1.4140 + 8.0858i	-0.0715 + 0.0344i	7.5551
3	898	5.8364 + 8.1683i	-0.2792 + 0.2134i	5.3601
4	858	7.0015 + 4.8457i	0.2853 + 1.2968i	1.2419 + 10.1840i
5	820	6.2937 + 2.1464i	0.3530 - 1.1251i	6.3721 + 5.3302i
6	795	4.1938 + 1.0027i	-0.1877 - 0.7492i	11.3780
7	770	2.7200 + 0.9165i	-0.2631 - 0.5064i	6.3074
8	740	1.6244 + 1.0867i	-0.2513 - 0.3549i	8.2030
9	707	0.5590 + 1.5098i	-0.2216 - 0.2599i	5.8829 + 0.5181i
10	668	0.1378 + 2.3466i	-0.1922 - 0.1995i	4.8429

Bibliography

[1] Eng Aik Chan, Syed Abdullah Aljunid, Giorgio Adamo, Athanasios Laliotis, Martial Ducloy, and David Wilkowski. Tailoring optical metamaterials to tune the atom-surface casimir-polder interaction. Science Advances, 4(2), 2018.

[2] Eng Aik Chan, Syed Abdullah Aljunid, Nikolay I Zheludev, David Wilkowski, and Martial Ducloy. Doppler-free approach to optical pumping dynamics in the $6s_{1/2}$- $5d_{5/2}$ electric quadrupole transition of cesium vapor. Optics Letters, 41(9):2005–2008, 2016.

[3] P. A. D. Gonçalves, Thomas Christensen, Nicholas Rivera, Antti-Pekka Jauho, N. Asger Mortensen, and Marin Soljačić. Plasmon-emitter interactions at the nanoscale. 2019.

[4] Heiko Groß, Joachim M. Hamm, Tommaso Tufarelli, Ortwin Hess, and Bert Hecht. Near-field strong coupling of single quantum dots. Science Advances, 4(3), 2018.

[5] Yoel Sebbag, Pankaj Arora, Yefim Barash, and Uriel Levy. Cooperative coupling of hot alkali vapors to surface plasmon: Towards room temperature quantum plasmonics with atomic media. In Conference on Lasers and Electro-Optics, page FTu4E.5. Optical Society of America, 2018.

[6] Eliran Talker, Pankaj Arora, Yefim Barash, Liron Stern, and Uriel Levy. Plasmonic enhanced eit and velocity selective optical pumping measurements with atomic vapor. ACS Photonics, 5(7):2609–2616, 2018.

[7] Liron Stern, Meir Grajower, and Uriel Levy. Fano resonances and all-optical switching in a resonantly coupled plasmonic-atomic system. Nature Communications, 5:4865 EP –, Sep 2014. Article.

[8] Liron Stern, Meir Grajower, Noa Mazurski, and Uriel Levy. Magnetically controlled atomic–plasmonic fano resonances. Nano Letters, 18(1):202–207, 2018. PMID: 29240438.

[9] Matthias Mildner, Andreas Horrer, Monika Fleischer, Claus Zimmermann, and Sebastian Slama. Plasmonic trapping potentials for cold atoms. Journal of Physics B: Atomic, Molecular and Optical Physics, 51(13):135005, 2018.

[10] Tomasz Kawalec, Aleksandra Sierant, Roman Panaś, Jacek Fiutowski, Dobrosława Bartoszek-Bober, Leszek Józefowski, and Horst-Günter Rubahn. Surface plasmon polaritons probed with cold atoms. Plasmonics, 13(2):639–644, Apr 2018.

[11] Christian Stehle, Helmar Bender, Claus Zimmermann, Dieter Kern, Monika Fleischer, and Sebastian Slama. Plasmonically tailored micropotentials for ultracold atoms. Nature Photonics, 5:494 EP –, Jul 2011. Article.

[12] Christian Stehle, Claus Zimmermann, and Sebastian Slama. Cooperative coupling of ultracold atoms and surface plasmons. Nature Physics, 10:937 EP –, Oct 2014. Article.

[13] Simeon I. Bogdanov, Mikhail Y. Shalaginov, Alexei S. Lagutchev, Chin-Cheng Chiang, Deesha Shah, Alexandr S. Baburin, Ilya A. Ryzhikov, Ilya A. Rodionov, Alexander V. Kildishev, Alexandra Boltasseva, and Vladimir M. Shalaev. Ultrabright room-temperature sub-nanosecond emission from single nitrogen-vacancy centers coupled to nanopatch antennas. Nano Letters, 18(8):4837–4844, 2018. PMID: 29969274.

[14] Horacio Failache, Solomon Saltiel, Michèle Fichet, Daniel Bloch, and Martial Ducloy. Resonant van der Waals Repulsion between Excited Cs Atoms and Sapphire Surface. Physical Review Letters, 83(26):5467–5470, December 1999.

[15] H. Failache, S. Saltiel, M. Fichet, D. Bloch, and M. Ducloy. Resonant coupling in the van der Waals interaction between an excited alkali

atom and a dielectric surface: an experimental study via stepwise selective reflection spectroscopy. The European Physical Journal D, 23(2):237–255, May 2003.

[16] F. S. S. Rosa, D. A. R. Dalvit, and P. W. Milonni. Casimir-lifshitz theory and metamaterials. Physical Review Letters, 100:183602, May 2008.

[17] V. Yannopapas and N. V. Vitanov. Casimir-polder interaction between an atom and a periodic nanostructure. Physical Review A, 81:042506, Apr 2010.

[18] Mohammadreza Khorasaninejad, Francesco Aieta, Pritpal Kanhaiya, Mikhail A. Kats, Patrice Genevet, David Rousso, and Federico Capasso. Achromatic metasurface lens at telecommunication wavelengths. Nano Letters, 15(8):5358–5362, 2015. PMID: 26168329.

[19] Longqing Cong, Wei Cao, Xueqian Zhang, Zhen Tian, Jianqiang Gu, Ranjan Singh, Jiaguang Han, and Weili Zhang. A perfect metamaterial polarization rotator. Applied Physics Letters, 103(17):171107, 2013.

[20] Yi-Ju Chiang and Ta-Jen Yen. A composite-metamaterial-based terahertz-wave polarization rotator with an ultrathin thickness, an excellent conversion ratio, and enhanced transmission. Applied Physics Letters, 102(1):011129, 2013.

[21] T. W. Ebbesen, H. J. Lezec, H. F. Ghaemi, T. Thio, and P. A. Wolff. Extraordinary optical transmission through sub-wavelength hole arrays. Nature, 391(6668):667–669, 1998.

[22] DE Chang, K Sinha, JM Taylor, and HJ Kimble. Trapping atoms using nanoscale quantum vacuum forces. Nature Communications, 5, 2014.

[23] Josephine Gutekunst, Daniel Weller, Harald Kübler, Jan-Philipp Negel, Marwan Abdou Ahmed, Thomas Graf, and Robert Löw. Fiber-integrated spectroscopy device for hot alkali vapor. Applied Optics, 56(21):5898–5902, Jul 2017.

[24] Saikat Ghosh, Amar R. Bhagwat, C. Kyle Renshaw, Shireen Goh, Alexander L. Gaeta, and Brian J. Kirby. Low-light-level optical interactions with rubidium vapor in a photonic band-gap fiber. Physical Review Letters, 97:023603, Jul 2006.

[25] Liron Stern, Boris Desiatov, Noa Mazurski, and Uriel Levy. Strong coupling and high-contrast all-optical modulation in atomic cladding waveguides. Nature Communications, 8:14461 EP –, Feb 2017. Article.

[26] E. Vetsch, D. Reitz, G. Sagué, R. Schmidt, S. T. Dawkins, and A. Rauschenbeutel. Optical interface created by laser-cooled atoms trapped in the evanescent field surrounding an optical nanofiber. Physical Review Letters, 104:203603, May 2010.

[27] A. M. Kern and O. J. F. Martin. Strong enhancement of forbidden atomic transitions using plasmonic nanostructures. Physical Review A, 85:022501, Feb 2012.

[28] Vassilios Yannopapas and Emmanuel Paspalakis. Giant enhancement of dipole-forbidden transitions via lattices of plasmonic nanoparticles. Journal of Modern Optics, 62(17):1435–1441, October 2015.

[29] Kazuhiro Deguchi, Michihiro Okuda, Atsushi Iwamae, Hiroaki Nakamura, Keiji Sawada, and Masahiro Hasuo. Simulation of Electric Quadrupole and Magnetic Dipole Transition Efficiencies in Optical Near Fields Generated by a Subwavelength Slit Array. Journal of the Physical Society of Japan, 78(2):024301, 2009.

[30] Kosuke Shibata, Satoshi Tojo, and Daniel Bloch. Excitation enhancement in electric multipole transitions near a nanoedge. Optics Express, 25(8):9476–9489, Apr 2017.

[31] J.P. Woerdman and M.F.H. Schuurmans. Spectral narrowing of selective reflection from sodium vapour. Optics Communications, 14(2):248–251, June 1975.

[32] Schuurmans, M. F. H. Spectral narrowing of selective reflection. Journal de Physique France, 37(5):469–485, 1976.

[33] M.F. H. Schuurmans. The fluorescence of atoms near a glass surface. Contemporary Physics, 21(5):463–482, 1980.

[34] TA Vartanyan. Resonant reflection of intense optical radiation from a low-density gaseous medium. Journal of Experimental and Theoretical Physics Soviet, 61(4):674–677, 1985.

[35] Suneel Singh and G.S. Agarwal. Effect of collisions with surface on nonlinear optical properties and nonlinear selective reflection. Optics Communications, 59(2):107 – 112, 1986.

[36] R.W. Wood. Xx. the selective reflexion of monochromatic light by mercury vapour. The London, Edinburgh, and Dublin Philosophical Magazine and Journal of Science, 18(103):187–193, 1909.

[37] M. Born and E. Wolf. Principles of Optics: Electromagnetic Theory of Propagation, Interference and Diffraction of Light. Elsevier Science, 2013.

[38] Cojan, Jean-Louis. Contribution à l'étude de la réflexion sélective sur les vapeurs de mercure de la radiation de résonance du mercure. Annales de Physique, 12(9):385–440, 1954.

[39] Burgmans, A.L.J. and Woerdman, J.P. Selective reflection from sodium vapour at low densities. Journal de Physique France, 37(6):677–681, 1976.

[40] Am Akulshin, Vl Velichanskii, As Zibrov, Vv Nikitin, Vv Sautenkov, Ek Yurkin, and Nv Senkov. Collisional Broadening of Intra-Doppler Resonances of Selective Reflection on the D2 Line of Cesium. JETP Letters, 36(7):303–307, 1982. WOS:A1982QP81200007.

[41] M. Oria, M. Chevrollier, D. Bloch, M. Fichet, and M. Ducloy. Spectral Observation of Surface-Induced Van der Waals Attraction on Atomic Vapour. Europhysics Letters, 14(6):527, March 1991.

[42] M. Ducloy and M. Fichet. General theory of frequency modulated selective reflection. influence of atom surface interactions. Journal de Physique II France, 1(12):1429–1446, 1991.

[43] G. Nienhuis, F. Schuller, and M. Ducloy. Nonlinear selective reflection from an atomic vapor at arbitrary incidence angle. Physical Review A, 38:5197–5205, Nov 1988.

[44] V. Vuletić, V.A. Sautenkov, C. Zimmermann, and T.W. Hänsch. Optical pumping saturation effect in selective reflection. Optics Communications, 108(1):77 – 83, 1994.

[45] F. Schuller, O. Gorceix, and M. Ducloy. Nonlinear selective reflection in cascade three-level atomic systems. Physical Review A, 47:519–528, Jan 1993.

[46] G. Nienhuis and F. Schuller. Selective reflection from a vapor of three-level atoms. Physical Review A, 50:1586–1592, Aug 1994.

[47] S Le Boiteux, P Simoneau, D Bloch, and M Ducloy. Doppler-free spectroscopy at a glass-vapour interface by saturated selective reflection at near normal incidence. Journal of Physics B: Atomic and Molecular Physics, 20(5):L149, 1987.

[48] Yan-Ting Zhao, Jie Ma, Li-Rong Wang, Jian-Ming Zhao, Lian-Tuan Xiao, and Suo-Tang Jia. Spectral hole-burning in pump–probe studies of nonlinear selective reflection spectroscopy. Journal of Physics B: Atomic, Molecular and Optical Physics, 38(16):3037, 2005.

[49] J. Guo, J. Cooper, A. Gallagher, and M. Lewenstein. Theory of selective reflection spectroscopy. Optics Communications, 110(1):197 – 208, 1994.

[50] B. Gross, N. Papageorgiou, V. Sautenkov, and A. Weis. Velocity selective optical pumping and dark resonances in selective reflection spectroscopy. Physical Review A, 55:2973–2981, Apr 1997.

[51] Jeffery J. Maki, Michelle S. Malcuit, J. E. Sipe, and Robert W. Boyd. Linear and nonlinear optical measurements of the lorentz local field. Physical Review Letters, 67:972–975, Aug 1991.

[52] Badalyan, A., Chaltykyan, V., Grigoryan, G., Papoyan, A., Shmavonyan, S., and Movsessian, M. Selective reflection by atomic vapor: experiments and self-consistent theory. The European Physical Journal D, 37(2):157–162, 2006.

[53] G. Stanzel. Level- and line-crossing experiments in selective reflection from mercury vapour. Zeitschrift für Physik, 270(4):361–369, Dec 1974.

[54] W. Siegmund and A. Scharmann. Level- and line-crossing in forward scattering and selective reflection in a transverse magnetic field. Zeitschrift für Physik A Atoms and Nuclei, 276(1):19–24, Mar 1976.

[55] A. Weis, V. A. Sautenkov, and T. W. Hänsch. Observation of ground-state zeeman coherences in the selective reflection from cesium vapor. Physical Review A, 45:7991–7996, Jun 1992.

[56] N. Papageorgiou, A. Weis, V. A. Sautenkov, D. Bloch, and M. Ducloy. High-resolution selective reflection spectroscopy in intermediate magnetic fields. Applied Physics B, 59(2):123–126, Aug 1994.

[57] M. Chevrollier, M. Oriá, J. G. de Souza, D. Bloch, M. Fichet, and M. Ducloy. Selective reflection spectroscopy of a resonant vapor at the interface with a metallic layer. Physical Review E, 63(4):046610, March 2001.

[58] M. Fichet, F. Schuller, D. Bloch, and M. Ducloy. van der Waals interactions between excited-state atoms and dispersive dielectric surfaces. Physical Review A, 51(2):1553–1564, February 1995.

[59] Horacio Failache, Solomon Saltiel, Alexis Fischer, Daniel Bloch, and Martial Ducloy. Resonant Quenching of Gas-Phase Cs Atoms Induced by Surface Polaritons. Physical Review Letters, 88(24):243603, May 2002.

[60] M. Fichet, G. Dutier, A. Yarovitsky, P. Todorov, I. Hamdi, I. Maurin, S. Saltiel, D. Sarkisyan, M.-P. Gorza, D. Bloch, and M. Ducloy. Exploring the van der waals atom-surface attraction in the nanometric range. Europhysics Letters, 77(5):54001, 2007.

[61] Armen Sargsyan, Aram Papoyan, Ifan G. Hughes, Charles S. Adams, and David Sarkisyan. Selective reflection from an rb layer with a thickness below $\lambda/12$ and applications. Optics Letters, 42(8):1476–1479, Apr 2017.

[62] M. Born, E. Wolf, and A.B. Bhatia. Principles of Optics: Electromagnetic Theory of Propagation, Interference and Diffraction of Light. Cambridge University Press, 2000.

[63] E. Balagurusamy. Numerical Methods.

[64] J. E. Lennard-Jones. Processes of adsorption and diffusion on solid surfaces. Transactions of the Faraday Society, 28(0):333–359, January 1932.

[65] H. B. G. Casimir and D. Polder. The influence of retardation on the london-van der waals forces. Physical Review, 73:360–372, Feb 1948.

[66] West P.R., Ishii S., Naik G.V., Emani N.K., Shalaev V.M., and Boltasseva A. Searching for better plasmonic materials. Laser & Photonics Reviews, 4(6):795–808.

[67] A. SOMMER. Alloys of gold with alkali metals. Nature, 152:215 EP –, Aug 1943.

[68] C. J. Foot. Atomic Physics, chapter 8.

[69] Thomas Kugelstadt. Active filter design techniques. In Op Amps for Everyone (Third Edition), chapter 16.3.2.2, pages 16–18.

[70] Paul Siddons, Charles S Adams, Chang Ge, and Ifan G Hughes. Absolute absorption on rubidium d lines: comparison between theory and experiment. Journal of Physics B: Atomic, Molecular and Optical Physics, 41(15):155004, 2008.

[71] Daniel A Steck. Cesium d line data. Chapter 2:3.

[72] Lee Weller, Robert J Bettles, Paul Siddons, Charles S Adams, and Ifan G Hughes. Absolute absorption on the rubidium d 1 line including resonant dipole–dipole interactions. Journal of Physics B: Atomic, Molecular and Optical Physics, 44(19):195006, 2011.

[73] A Goban, C-L Hung, S-P Yu, JD Hood, JA Muniz, JH Lee, MJ Martin, AC McClung, KS Choi, Darrick E Chang, et al. Atom–light interactions in photonic crystals. Nature Communications, 5:3808, 2014.

[74] S-P Yu, JD Hood, JA Muniz, MJ Martin, Richard Norte, C-L Hung, Seán M Meenehan, Justin D Cohen, Oskar Painter, and HJ Kimble. Nanowire photonic crystal waveguides for single-atom trapping and strong light-matter interactions. Applied Physics Letters, 104(11):111103, 2014.

[75] Athanasios Laliotis, Thierry Passerat de Silans, Isabelle Maurin, Martial Ducloy, and Daniel Bloch. Casimir–Polder interactions in the presence of thermally excited surface modes. Nature Communications, 5:4364, July 2014.

[76] Cyrille Billaudeau, Stéphane Collin, Fabrice Pardo, Nathalie Bardou, and Jean-Luc Pelouard. Tailoring radiative and non-radiative losses of thin nanostructured plasmonic waveguides. Opt. Express, 17(5):3490–3499, Mar 2009.

[77] Wei-Shun Chang, Britain A. Willingham, Liane S. Slaughter, Bishnu P. Khanal, Leonid Vigderman, Eugene R. Zubarev, and Stephan Link. Low absorption losses of strongly coupled surface plasmons in nanoparticle assemblies. Proceedings of the National Academy of Sciences, 108(50):19879–19884, 2011.

[78] J. Baker-Jarvis, E.J. Vanzura, and W.A. Kissick. Improved technique for determining complex permittivity with the transmission/reflection method. IEEE Transactions on Microwave Theory and Techniques, 38(8):1096–1103, August 1990.

[79] Xudong Chen, Tomasz M. Grzegorczyk, Bae-Ian Wu, Joe Pacheco, and Jin Au Kong. Robust method to retrieve the constitutive effective parameters of metamaterials. Physical Review E, 70(1):016608, July 2004.

[80] Martine Chevrollier, Michèle Fichet, Marcos Oria, Gabriel Rahmat, Daniel Bloch, and Martial Ducloy. High resolution selective reflection spectroscopy as a probe of long-range surface interaction : measurement of the surface van der Waals attraction exerted on excited Cs atoms. Journal de Physique II, 2(4):631–657, April 1992.

[81] Gleb M. Akselrod, Christos Argyropoulos, Thang B. Hoang, Cristian Ciracì, Chao Fang, Jiani Huang, David R. Smith, and Maiken H. Mikkelsen. Probing the mechanisms of large purcell enhancement in plasmonic nanoantennas. Nature Photonics, 8:835 EP –, Oct 2014.

[82] M. A. Ordal, L. L. Long, R. J. Bell, S. E. Bell, R. R. Bell, R. W. Alexander, and C. A. Ward. Optical properties of the metals al, co, cu, au, fe, pb, ni, pd, pt, ag, ti, and w in the infrared and far infrared. Applied Optics, 22(7):1099–1119, Apr 1983.

[83] J. M. Wylie and J. E. Sipe. Quantum electrodynamics near an interface. Physical Review A, 30:1185–1193, Sep 1984.

[84] J. M. Wylie and J. E. Sipe. Quantum electrodynamics near an interface. ii. Physical Review A, 32:2030–2043, Oct 1985.

[85] M.-P. Gorza, S. Saltiel, H. Failache, and M. Ducloy. Quantum theory of van der Waals interactions between excited atoms and birefringent dielectric surfaces. The European Physical Journal D, 15(1):113–126, July 2001.

[86] Xuan Yang, Nazar Ileri, Cindy C. Larson, Thomas C. Carlson, Jerald A. Britten, Allan S. P. Chang, Claire Gu, and Tiziana C. Bond. Nanopillar array on a fiber facet for highly sensitive surface-enhanced raman scattering. Optics Express, 20(22):24819–24826, Oct 2012.

[87] Zhen Yin, Youfu Geng, Qingli Xie, Xueming Hong, Xiaoling Tan, Yuzhi Chen, Lele Wang, Wenjia Wang, and Xuejin Li. Photoreduced silver nanoparticles grown on femtosecond laser ablated, d-shaped fiber probe for surface-enhanced raman scattering. Applied Optics, 55(20):5408–5412, Jul 2016.

[88] Armando Ricciardi, Marco Consales, Giuseppe Quero, Alessio Crescitelli, Emanuela Esposito, and Andrea Cusano. Versatile optical fiber nanoprobes: From plasmonic biosensors to polarization-sensitive devices. ACS Photonics, 1(1):69–78, 2014.

[89] Joseph W Goodman. Speckle phenomena in optics : theory and applications. Roberts and Company Publishers, 2007.

[90] Syed Abdullah Aljunid, Eng Aik Chan, Giorgio Adamo, Martial Ducloy, David Wilkowski, and Nikolay I. Zheludev. Atomic response in the near-field of nanostructured plasmonic metamaterial. Nano Letters, 16(5):3137–3141, 2016. PMID: 27018806.

[91] R C Kuhn, O Sigwarth, C Miniatura, D Delande, and C A Müller. Coherent matter wave transport in speckle potentials. New Journal of Physics, 9(6):161, 2007.

[92] Giulia Semeghini, Manuele Landini, Patricia Castilho, Sanjukta Roy, Giacomo Spagnolli, Andreas Trenkwalder, Marco Fattori, Massimo Inguscio, and Giovanni Modugno. Measurement of the mobility edge for 3d anderson localization. Nature Physics, 11(7):554–559, 2015.

[93] Valentin V. Volchkov, Michael Pasek, Vincent Denechaud, Musawwadah Mukhtar, Alain Aspect, Dominique Delande, and Vincent Josse. Measurement of spectral functions of ultracold atoms in disordered potentials. Physical Review Letters, 120:060404, Feb 2018.

[94] Pranjal Bordia, Henrik P. Lüschen, Sean S. Hodgman, Michael Schreiber, Immanuel Bloch, and Ulrich Schneider. Coupling identical one-dimensional many-body localized systems. Physical Review Letters, 116:140401, Apr 2016.

[95] E. Suarez, D. Auwärter, T. J. Arruda, R. Bachelard, P. W. Courteille, C. Zimmermann, and S. Slama. Photon-antibunching in the fluorescence of statistical ensembles of emitters at an optical nanofiber-tip. ArXiv e-prints, September 2018.

[96] Vladilen S. Letokhov and V. P. Chebotayev. Nonlinear laser spectroscopy. Springer-Verlag, 1977.

[97] W. Demtröder. Laser spectroscopy : basic concepts and instrumentation. Advanced texts in physics. Berlin ; New York : Springer, c2003., 2003.

[98] K. Tsigutkin, D. Dounas-Frazer, A. Family, J. E. Stalnaker, V. V. Yashchuk, and D. Budker. Observation of a Large Atomic Parity Violation Effect in Ytterbium. Physical Review Letters, 103(7):071601, August 2009.

[99] Chr. Tamm, D. Engelke, and V. Bühner. Spectroscopy of the electric-quadrupole transition ${}^2S_{1/2}(F = 0)$– ${}^2D_{3/2}(F = 2)$ in trapped ${}^{171}\mathrm{Yb}^+$. Physical Review A, 61(5):053405, April 2000.

[100] W. H. Oskay, S. A. Diddams, E. A. Donley, T. M. Fortier, T. P. Heavner, L. Hollberg, W. M. Itano, S. R. Jefferts, M. J. Delaney, K. Kim, F. Levi, T. E. Parker, and J. C. Bergquist. Single-Atom Optical Clock with High Accuracy. Physical Review Letters, 97(2):020801, July 2006.

[101] T. Rosenband, D. B. Hume, P. O. Schmidt, C. W. Chou, A. Brusch, L. Lorini, W. H. Oskay, R. E. Drullinger, T. M. Fortier, J. E. Stalnaker, S. A. Diddams, W. C. Swann, N. R. Newbury, W. M. Itano, D. J. Wineland, and J. C. Bergquist. Frequency Ratio of Al+ and Hg+

Single-Ion Optical Clocks; Metrology at the 17th Decimal Place. Science, 319(5871):1808–1812, March 2008.

[102] Satoshi Tojo, Masahiro Hasuo, and Takashi Fujimoto. Absorption Enhancement of an Electric Quadrupole Transition of Cesium Atoms in an Evanescent Field. Physical Review Letters, 92(5):053001, February 2004.

[103] Satoshi Tojo, Takashi Fujimoto, and Masahiro Hasuo. Precision measurement of the oscillator strength of the cesium $6\,^2s_{1/2} \rightarrow 5\,^2d_{5/2}$ electric quadrupole transition in propagating and evanescent wave fields. Physical Review A, 71(1):012507, January 2005.

[104] K.-H. Weber and Craig J. Sansonetti. Accurate energies of nS , nP , nD , nF , and nG levels of neutral cesium. Physical Review A, 35(11):4650–4660, June 1987.

[105] F. Ponciano-Ojeda, S. Hernández-Gómez, O. López-Hernández, C. Mojica-Casique, R. Colín-Rodríguez, F. Ramírez-Martínez, J. Flores-Mijangos, D. Sahagún, R. Jáuregui, and J. Jiménez-Mier. Observation of the $5p_{3/2} \rightarrow 6p_{3/2}$ electric-dipole-forbidden transition in atomic rubidium using optical-optical double-resonance spectroscopy. Physical Review A, 92:042511, Oct 2015.

[106] Armen Sargsyan, Ara Tonoyan, Grant Hakhumyan, Aram Papoyan, Emilio Mariotti, and David Sarkisyan. Giant modification of atomic transition probabilities induced by a magnetic field: forbidden transitions become predominant. Laser Physics Letters, 11(5):055701, 2014.

[107] F. Nez, F. Biraben, R. Felder, and Y. Millerioux. Optical frequency determination of the hyperfine components of the 5s12-5d32 two-photon transitions in rubidium. Optics Communications, 102(5):432–438, October 1993.

[108] P. V. Kiran Kumar and M. V. Suryanarayana. Precision two-photon spectroscopy of alkali elements. Pramana, 83(2):189–219, July 2014.

[109] M. S. Feld and A. Javan. Laser-Induced Line-Narrowing Effects in Coupled Doppler-Broadened Transitions. Physical Review, 177(2):540–562, January 1969.

[110] Martial Ducloy, José R. R. Leite, and Michael S. Feld. Laser saturation spectroscopy in the time-delayed mode. Theory of optical free induction decay in coupled Doppler-broadened systems. Physical Review A, 17(2):623–644, February 1978.

[111] P. Thoumany, T. Hänsch, G. Stania, L. Urbonas, and Th. Becker. Optical spectroscopy of rubidium Rydberg atoms with a 297 nm frequency-doubled dye laser. Optics Letters, 34(11):1621, June 2009.

[112] D. DiBerardino, C. E. Tanner, and A. Sieradzan. Lifetime measurements of cesium $5d^2d_{5/2,3/2}$ and $11s^2s_{1/2}$ states using pulsed-laser excitation. Physical Review A, 57(6):4204–4211, June 1998.

[113] Mitchel Weissbluth. Atoms and molecules. Academic Press, New York, 1978.

[114] C Mojica-Casique, F Ponciano-Ojeda, S Hernández-Gómez, O López-Hernández, J Flores-Mijangos, F Ramírez-Martínez, D Sahagún, R Jáuregui, and J Jiménez-Mier. Control of electronic magnetic state population via light polarization in the 5 p 3/2 - 6 p 3/2 electric quadrupole transition in atomic rubidium. Journal of Physics B: Atomic, Molecular and Optical Physics, 50(2):025003, 2017.

[115] J Sagle, R K Namiotka, and J Huennekens. Measurement and modelling of intensity dependent absorption and transit relaxation on the cesium line. Journal of Physics B: Atomic, Molecular and Optical Physics, 29(12):2629, 1996.

[116] Vasily Klimov, Daniel Bloch, Martial Ducloy, and Jose R. Rios Leite. Detecting photons in the dark region of Laguerre-Gauss beams. Optics Express, 17(12):9718, June 2009.

[117] V. V. Klimov, D. Bloch, M. Ducloy, and J. R. Rios Leite. Mapping of focused Laguerre-Gauss beams: The interplay between spin and orbital angular momentum and its dependence on detector characteristics. Physical Review A, 85(5):053834, May 2012.

[118] M. Auzinsh, D. Budker, and S. Rochester. Optically Polarized Atoms: Understanding Light-atom Interactions. OUP Oxford, 2010.

[119] Nicholas Rivera, Ido Kaminer, Bo Zhen, John D Joannopoulos, and Marin Soljačić. Shrinking light to allow forbidden transitions on the atomic scale. Science, 353(6296):263–269, 2016.

[120] Syed Abdullah Aljunid, Eng Aik Chan, Giorgio Adamo, Martial Ducloy, David Wilkowski, and Nikolay I. Zheludev. Atomic Response in the Near-Field of Nanostructured Plasmonic Metamaterial. Nano Letters, 16(5):3137–3141, May 2016.

[121] R. H. Dicke. The effect of collisions upon the doppler width of spectral lines. Physical Review, 89:472–473, Jan 1953.

[122] R. P. Frueholz and J. C. Camparo. Implications of the trapping-desorption and direct inelastic-scattering channels on dicke-narrowed line shapes. Physical Review A, 35:3768–3774, May 1987.

[123] Tapashree Roy, Edward T. F. Rogers, and Nikolay I. Zheludev. Sub-wavelength focusing meta-lens. Optics Express, 21(6):7577–7582, Mar 2013.

[124] M V Berry and S Popescu. Evolution of quantum superoscillations and optical superresolution without evanescent waves. Journal of Physics A: Mathematical and General, 39(22):6965, 2006.

[125] V. I. Balykin, V. V. Klimov, and V. S. Letokhov. Atom nanooptics based on photon dots and photon holes. Journal of Experimental and Theoretical Physics Letters, 78(1):8–12, Jul 2003.

[126] Thejesh N. Bandi, Vladimir G. Minogin, and Síle Nic Chormaic. Atom microtraps based on near-field fresnel diffraction. Physical Review A, 78:013410, Jul 2008.

[127] M. Gullans, T. G. Tiecke, D. E. Chang, J. Feist, J. D. Thompson, J. I. Cirac, P. Zoller, and M. D. Lukin. Nanoplasmonic Lattices for Ultracold Atoms. Physical Review Letters, 109(23):235309, December 2012.

[128] A. González-Tudela, C.-L. Hung, D. E. Chang, J. I. Cirac, and H. J. Kimble. Subwavelength vacuum lattices and atom-atom interactions in two-dimensional photonic crystals. Nature Photonics, 9:320 EP –, Apr 2015. Article.

[129] B. Darquié, M. P. A. Jones, J. Dingjan, J. Beugnon, S. Bergamini, Y. Sortais, G. Messin, A. Browaeys, and P. Grangier. Controlled single-photon emission from a single trapped two-level atom. Science, 309(5733):454–456, 2005.

[130] Meng Khoon Tey, Zilong Chen, Syed Abdullah Aljunid, Brenda Chng, Florian Huber, Gleb Maslennikov, and Christian Kurtsiefer. Strong interaction between light and a single trapped atom without the need for?a?cavity. Nature Physics, 4:924 EP –, Oct 2008.

[131] Waseem S. Bakr, Jonathon I. Gillen, Amy Peng, Simon Fölling, and Markus Greiner. A quantum gas microscope for detecting single atoms in a hubbard-regime optical lattice. Nature, 462:74 EP –, Nov 2009.

[132] Christof Weitenberg, Manuel Endres, Jacob F. Sherson, Marc Cheneau, Peter Schauß, Takeshi Fukuhara, Immanuel Bloch, and Stefan Kuhr. Single-spin addressing in an atomic mott insulator. Nature, 471:319 EP –, Mar 2011. Article.

[133] Marc Cheneau, Peter Barmettler, Dario Poletti, Manuel Endres, Peter Schauß, Takeshi Fukuhara, Christian Gross, Immanuel Bloch, Corinna Kollath, and Stefan Kuhr. Light-cone-like spreading of correlations in a quantum many-body system. Nature, 481:484 EP –, Jan 2012.